

# TECHNICAL REPORT 00-08

Grimsel Test Site  
Investigation Phase IV (1994-1996)

**The Nagra-JNC in situ study of safety  
relevant radionuclide retardation  
in fractured crystalline rock**

**IV: The in situ study of matrix porosity in  
the vicinity of a water conducting fracture**

May 2003

A. Möri, M. Mazurek, M. Adler, M. Schild,  
S. Siegesmund, A. Vollbrecht, K. Ota, T. Ando,  
W.R. Alexander, P.A. Smith, P. Haag, Ch. Bühler



# TECHNICAL REPORT 00-08

Grimsel Test Site  
Investigation Phase IV (1994-1996)

**The Nagra-JNC in situ study of safety  
relevant radionuclide retardation  
in fractured crystalline rock**

**IV: The in situ study of matrix porosity in  
the vicinity of a water conducting fracture**

May 2003

A. Möri <sup>1)</sup>, M. Mazurek <sup>2)</sup>, M. Adler <sup>2)</sup>, M. Schild <sup>3)</sup>,  
S. Siegesmund <sup>3)</sup>, A. Vollbrecht <sup>3)</sup>, K. Ota <sup>4)</sup>, T. Ando <sup>4)</sup>,  
W.R. Alexander <sup>5)</sup>, P.A. Smith <sup>6)</sup>, P. Haag <sup>7)</sup>, Ch. Bühler <sup>8)</sup>

<sup>1)</sup> Geotechnisches Institut AG, Bern, Switzerland

<sup>2)</sup> GGWW (Rock-Water Interaction Group),  
University of Berne, Switzerland

<sup>3)</sup> Institut für Geologie und Dynamik der Lithosphäre,  
University of Göttingen, Germany

<sup>4)</sup> JNC (Japan Nuclear Cycle Development Institute),  
Tono Geoscience Centre, Gifu, Japan

<sup>5)</sup> Nagra, Wettingen, Switzerland

<sup>6)</sup> SAM (Safety Assessment Management), Edinburgh, Scotland

<sup>7)</sup> SIKA AG, Zürich, Switzerland

<sup>8)</sup> Solexperts AG, Schwerzenbach, Switzerland

This report was prepared on behalf of Nagra. The viewpoints presented and conclusions reached are those of the author(s) and do not necessarily represent those of Nagra.

**ISSN 1015-2636**

"Copyright © 2003 by Nagra, Wettingen (Switzerland) / All rights reserved.

All parts of this work are protected by copyright. Any utilisation outwith the remit of the copyright law is unlawful and liable to prosecution. This applies in particular to translations, storage and processing in electronic systems and programs, microfilms, reproductions, etc."



## FOREWORD

Concepts for the disposal of radioactive waste in geological formations depend crucially on a thorough knowledge of relevant processes in the host rock and on an understanding of the whole repository system, comprising both engineered and geological barriers. The Grimsel Test Site (GTS) is an underground rock laboratory which is used to investigate many of these processes in hard, fractured rocks. It has been operated since 1984 by the Swiss National Cooperative for the Disposal of Radioactive Waste (NAGRA).

The laboratory is located in the crystalline rock of the Central Aare Massif, 450 m below the eastern flank of the Juchlistock at an altitude of 1730 m asl. It is reached via a 1200 m long horizontal access tunnel, operated by the hydro-electric power company KWO. The layout of the tunnels that comprise the GTS allowed the establishment of a radiation controlled zone (IAEA type C in 1990, being upgraded to Type B in 1996) in which experiments with radioactive tracers are carried out. With increasing experience in the implementation of *in situ* experiments, improved process understanding and more advanced repository concepts, the experimental programmes at the GTS have gradually become more complex and more directly related to open questions defined by performance assessors or by regulatory bodies. Demonstration of disposal concepts by performing large- or full-scale, long-term experiments has also become a key aspect of investigations in the rock laboratory. The GTS Phase IV, 1994 – 1996, was initiated in close co-operation with a number of international partner organisations. The performed programmes focused on the characterisation and conceptualisation of the tunnel nearfield, geophysical investigations and experiments related on *in situ* radionuclide retardation.

Within the current investigation phase (Phase V; 1997 – 2002) seven experimental programmes and projects are included (see [www.grimsel.com](http://www.grimsel.com) for details).

Within GTS Phase IV, the Nagra-JNC Radionuclide Migration Programme (RMP) examined the behaviour of a large suite of radionuclides in the geosphere. The Connected Porosity project (CP), which began in 1996 and continued until 2000, is an integral part of RMP. This report summarises the results of the work. The main aim of CP was to examine the magnitude and extent of connectivity of the rock matrix porosity *in situ*. To this end, an acrylic resin was specially developed for rock matrix impregnation and methods to recover the impregnated rock matrix with the minimum of disturbance were tested in the GTS and in JNC's Kamaishi In Situ Test Site (KTS) in Japan. Three independent techniques (including the application of a novel porosimetry method) were then applied to the samples to assess the extent of *in situ* pore connectivity and the implications of the results to calculated radionuclide retardation in the geosphere were assessed.

This report is one of four Nagra Technical Reports (NTBs) on the RMP, that includes the Radionuclide Retardation Project (RRP) methodology (ALEXANDER et al. 2001b), the RRP final report (MÖRI et al. 2001), and the Migration Experiment final report (SMITH et al. 2001), all of which will be synthesised in ALEXANDER et al. (2002).

## VORWORT

Bei Lagerkonzepten für die Entsorgung radioaktiver Abfälle in geologischen Formationen sind eine vertiefte Kenntnis der relevanten Prozesse im Wirtgestein sowie ein Verständnis des gesamten Lagersystems mit den technischen und geologischen Barrieren von entscheidender Bedeutung. Das Felslabor Grimsel (FLG) ist ein standortunabhängiges Felslabor, in welchem zahlreiche dieser Prozesse in geklüftetem Festgestein untersucht werden. Es wird seit 1984 von der Nagra (Nationale Genossenschaft für die Lagerung radioaktiver Abfälle) betrieben.

Das FLG befindet sich im Kristallingestein des Zentralen Aarmassives 450 m unterhalb der Ostflanke des Juchlistocks auf einer Höhe von 1730 m ü.M. und kann durch einen 1200 m langen horizontalen Zugangstollen der Kraftwerke Oberhasli AG (KWO) erreicht werden. 1990 wurde in einem Stollenabschnitt des FLG eine kontrollierte Zone (IAEA Typ B 1990, höher gestuft auf Typ C 1996) für Versuche mit radioaktiven Tracern eingerichtet. Mit zunehmender Erfahrung bei der Durchführung von In-situ-Feldversuchen und verbessertem Systemverständnis der weiter entwickelten Lagerkonzepte, verlagerten sich die experimentellen Programmschwerpunkte hin zu komplexen, direkt auf die Anforderungen der Sicherheitsanalyse und Behörden ausgerichteten Versuche. Langzeit-Demonstrationsversuche in grösserem oder Originalmassstab gewannen bei den durchgeführten Untersuchungen im Felslabor zunehmend an Bedeutung. Die FLG Untersuchungsphase IV (1994 – 1996) wurde in enger Zusammenarbeit mit einer Anzahl internationaler Partnerorganisationen geplant. Die durchgeführten Versuchsprogramme konzentrierten sich auf die Charakterisierung und Konzeptualisierung des Tunnelnahfeldbereichs mit geophysikalischen Methoden und Versuchen zur Radionuklidrückhaltung.

Die jetzige Untersuchungsphase (Phase V, 1997 – 2002) umfasst sieben Versuchsprogramme und -projekte (siehe auch [www.grimsel.com](http://www.grimsel.com) für Einzelheiten).

Innerhalb der FLG Phase IV wurde mit dem Nagra-JNC Radionuklid-Migrationsprogramm (Radionuclide Migration Programme, RMP) das Verhalten einer Reihe von Radionukliden in der Geosphäre untersucht. Das Projekt 'Verbundene Porosität' (Connected Porosity project, CP), ist ein eigenständiges Teilprojekt von RMP, das 1996 begonnen und bis 2000 fortgeführt wurde. Der vorliegende Bericht fasst die Ergebnisse dieser Arbeiten zusammen. Die Hauptzielsetzung von CP war die In-situ-Untersuchung der Grösse und des Verbindungsgrads der Porosität der Gesteinsmatrix. Für die Imprägnierung der Gesteinsmatrix wurde speziell ein Acrylharz entwickelt und es wurden Methoden für die Gewinnung von möglichst wenig gestörten Gesteinsmatrixproben im FLG und am Kamaishi In situ-Teststandort (KTS) von JNC in Japan getestet. Bei den auf diese Weise gewonnenen Proben wurden drei unabhängige Techniken (inklusive der Anwendung eines neuartigen Porosimetrieverfahrens) angewendet, um das Ausmass der In-situ-Probenverbindung und die Auswirkungen dieser Resultate auf die berechnete Radionuklidretardierung in der Geosphäre abzuschätzen/zu bewerten.

Der vorliegenden Bericht ist Teil einer Reihe von vier Nagra Technischen Berichten (NTBs) zum Thema RMP, zusammen mit der Methodik des Radionuklidretardierungsprojekts (Radionuclide Retardation Project, RRP; ALEXANDER et al. 2001b), dem RRP Schlussbericht (MÖRI et al. 2001) und dem Schlussbericht zum Migrationsversuch (SMITH et al. 2001), deren Synthese in ALEXANDER et al. (2002) dargelegt ist.

## PRÉFACE

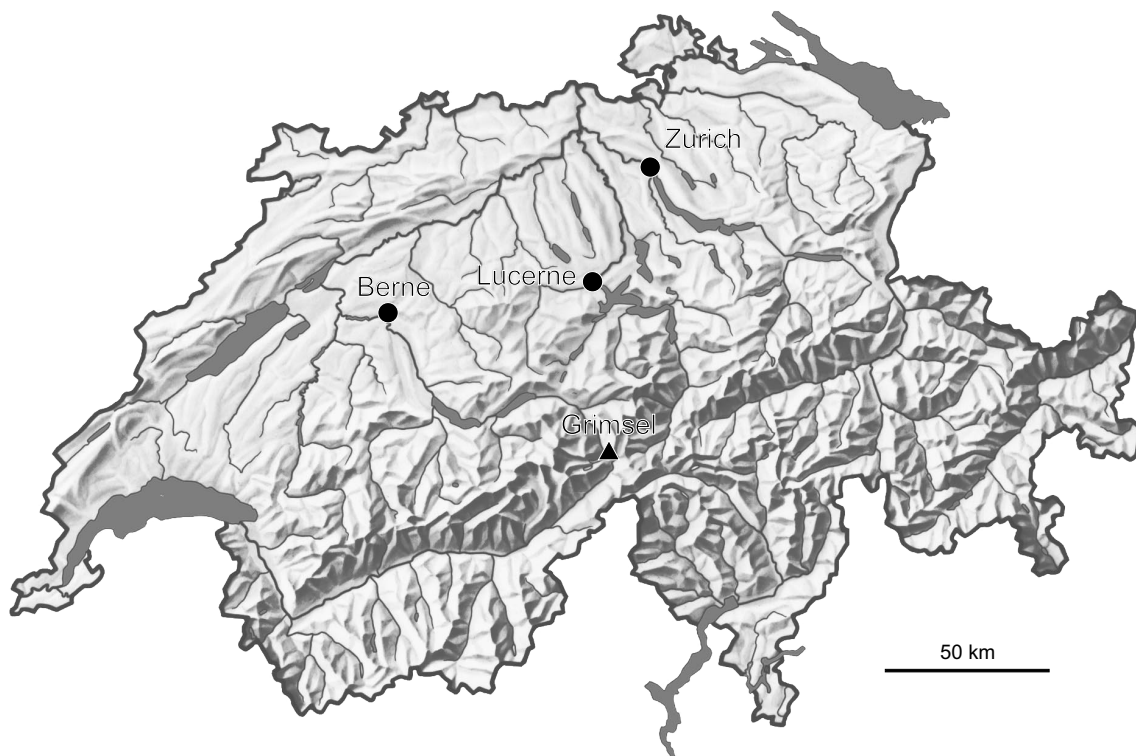
Les concepts élaborés pour le dépôt de déchets radioactifs dans des formations géologiques dépendent fondamentalement d'une connaissance approfondie des processus significatifs qui ont lieu dans la roche d'accueil et sur la compréhension du système de dépôt dans son ensemble, comprenant à la fois les barrières techniques et les barrières géologiques. Le laboratoire souterrain du Grimsel (Grimsel Test Site GTS) est un laboratoire souterrain de première génération destiné à étudier nombre de processus dans les roches consolidées fracturées. Il est en fonction depuis 1984, dirigé par la NAGRA, la Société coopérative nationale suisse pour l'entreposage de déchets radioactifs.

Le laboratoire est situé dans les roches cristallines du massif central de l'Aar, à une altitude de 1'730 m s.m., 450 m sous le flanc est du Juchlistock. On l'atteint par une galerie d'accès horizontale longue de 1200 m, exploitée par l'entreprise d'électricité hydraulique KWO. La disposition des galeries qui constituent le GTS a permis l'installation en 1990 d'une zone de radiation contrôlée (AIEA type B) dans laquelle sont conduites les expériences avec des traceurs radioactifs. Avec une expérience croissante dans la mise en œuvre d'essais *in situ*, la compréhension accrue des processus et des concepts de dépôts plus avancés, les programmes expérimentaux conduits au GTS ont gagné en complexité et se sont calqués plus directement sur les questions à élucider posées par les spécialistes en évaluation de performance et par les autorités compétentes. L'essai à grande échelle ou en vraie grandeur de concepts de dépôt, ainsi que des essais à long terme, sont également devenus un aspect clé des investigations au laboratoire souterrain. La phase IV du GTS, conduite de 1994 à 1996, a été mise en œuvre en coopération étroite avec des organisations partenaires internationales. Les programmes ont été focalisés sur la caractérisation et la conceptualisation du champ proche du tunnel, sur des recherches géophysiques et sur des expériences liées à l'étude du retardement *in situ* des radioéléments.

La phase actuelle des investigations (phase V, 1997 – 2002) comprend sept programmes et projets expérimentaux (voir [www.grimsel.com](http://www.grimsel.com) pour le détail).

Au cours de la phase IV du GTS, le programme d'étude de la migration des radioéléments (Radionuclide Migration Programme RMP), conduit conjointement par la Nagra et le JNC, a étudié le comportement de toute une série de radioéléments dans la géosphère. Le projet d'étude de la porosité interconnectée (Connected Porosity project CP), commencé en 1996 et poursuivi jusqu'en 2000, fait partie intégrante du RMP. Le présent rapport résume les résultats de ces travaux. Le CP avait comme objectif principal d'examiner *in situ* l'ampleur et l'extension de l'interconnection des pores dans la matrice rocheuse. Une résine acrylique a spécialement été développée dans ce but pour l'imprégnation de la matrice rocheuse, et on a testé au GTS et au site de test *in situ* de Kamaishi (KTS) du JNC au Japon des méthodes pour la récupération de la roche imprégnée avec le moins de dommage possible. Trois techniques indépendantes ont ensuite été appliquées aux échantillons pour évaluer l'extension *in situ* de l'interconnection des pores, et les conséquences des résultats sur le calcul du retardement des radioéléments dans la géosphère ont été évaluées.

Le présent rapport est un des quatre rapports techniques de la Nagra (Nagra Technical Reports NTB) sur le RMP. Cet ensemble comprend aussi un rapport (ALEXANDER et al. 2001b) sur la méthodologie du projet de retardement des radioéléments (RRP, Radionuclide Retardation Project), le rapport final du RRP (MÖRI et al. 2001), et le rapport final sur l'expérience de migration (Migration Experiment, SMITH et al. 2001). Tous ces rapports seront présentés sous forme synthétique dans ALEXANDER et al. (2002).



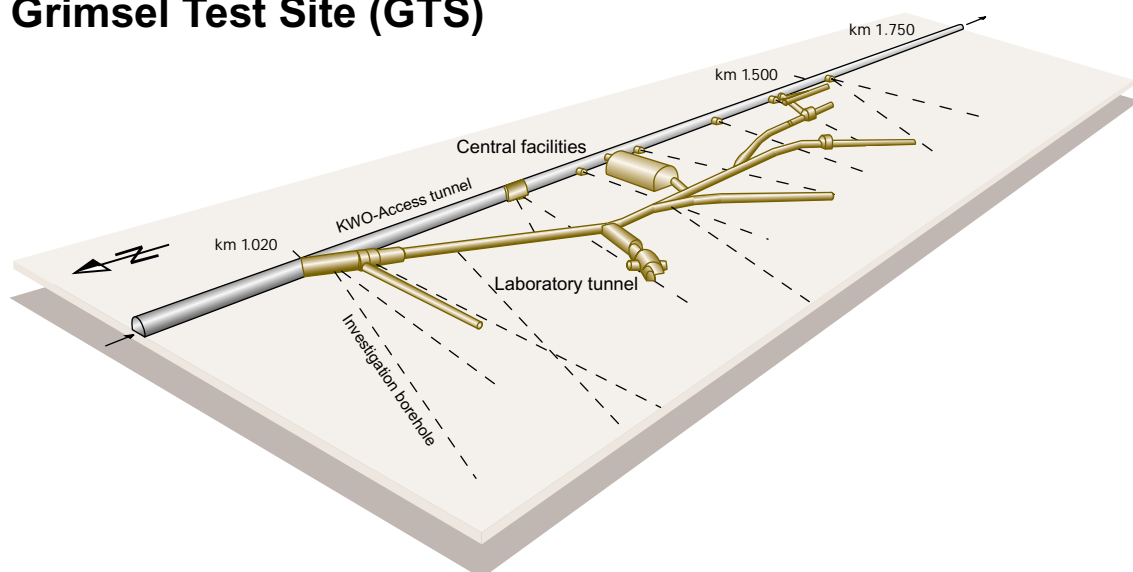
Location of Nagra's underground test facility at the Grimsel Pass in the Central Alps (Bernese Alps) of Switzerland

## Grimsel area (view to the west)



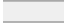
1 Grimsel Test Site    2 Lake Raeterichsboden    3 Lake Grimsel    4 Juchlistock


## Grimsel Test Site (GTS)







# Grimsel Test Site GTS

 KWO-Access tunnel

 Laboratory tunnel

 Central Aaregranite (CAGR)  
High biotite content CAGR

 Grimsel-Granodiorite

 Shear zone

 Lamprophyre

 SB Investigation borehole

**ZB** Central facilities

**BK** Fracture system flow

**GS** Rock stresses

**MI** Migration

**VE** Ventilation test

**WT** Heater test

## GTS Phase IV 1994-1996

**BOS** Borehole Sealing

**TOM** Further Development of  
Seismic Tomography

**EDZ** Excavation Disturbed Zone

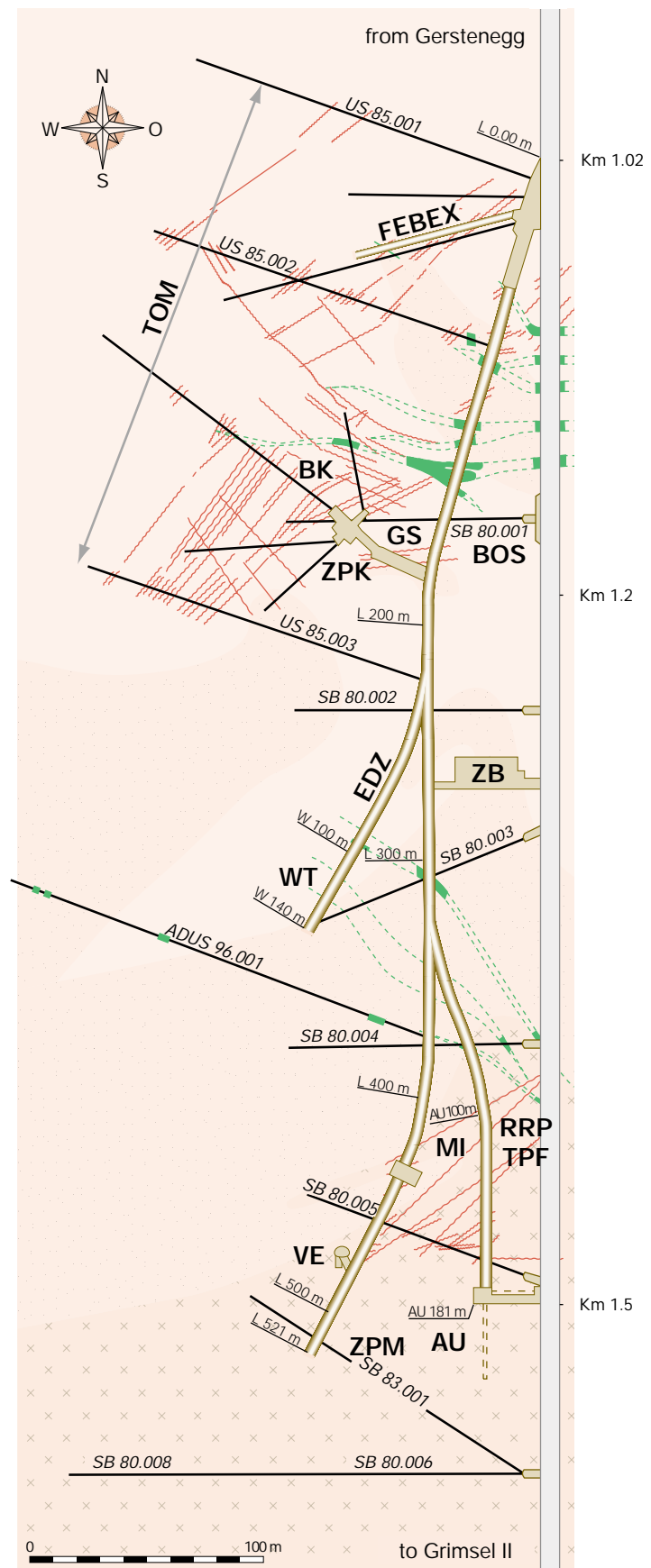
**TPF** Two-Phase Flow

**RRP** Radionuclide Retardation  
Project

**ZPK** Two-Phase Flow in Fracture Net-  
works of the Tunnel Near-field

**ZPM** Two-Phase Flow in the Unsatu-  
rated Matrix of Crystalline Rocks

**FEBEX** 1:1 EBS – Demonstration (HLW)



## SUMMARY

Matrix porosity is a key parameter for the evaluation of various scenarios in the estimation of radionuclide retardation in the geosphere. The amount, shape and size of the pores certainly influence radionuclide retardation, but the degree of connectivity (and therefore the accessibility for contaminants to these pores) must also be taken into consideration.

To date, most assessments of the role of matrix porosity have generally neglected (or have assessed the effects only qualitatively) to quantify the influence of sample disturbance on the geometry and the connectivity of pores, and its impact on the evaluation of total porosity, geophysical and hydraulic parameters. This being the case, this study was initiated to characterise the connectivity of *in situ* matrix porosity, to quantify the influence of sample preparation on total porosity and to assess the influence of the results on transport models used for performance assessment purposes.

A new technique for *in situ* impregnation of the diffusion-accessible rock matrix has been jointly developed by Nagra and JNC<sup>1</sup> and successfully applied to the granodiorite matrix behind a water conducting feature at Nagra's Grimsel Test Site (GTS) in Switzerland and JNC's Kamaishi *In Situ* Test Site (KTS) in Japan. After excavating the conserved rock matrix by over-coring, a large programme of petrographical, petrophysical and chemical analysis was applied to sub-samples taken from the core material outwith any disturbed zone in the rock (e.g. the influence of the injection borehole to the surrounding rock matrix, the tunnel excavation disturbed zone etc.).

The study revealed that the structural and mineralogical heterogeneity in the undeformed matrix of the Grimsel granodiorite is significant and strongly influences type and amount of the dominating porosity. Four different pore types could be distinguished: grain boundary pores, sheet silicate pores, solution pores and microfractures. All these pore types represent a connected network which was accessible for resin within the experimental time scales. Seismic velocity measurements ( $V_p$ ) on *in situ* and laboratory-impregnated rock samples as a function of confining pressure, water saturation and spatial direction revealed constraints on the distinction between *in situ* matrix pores and artificially induced pores. The comparison of conventional porosity determination techniques with a newly developed method to chemically analyse the amount of resin filled pores showed that conventional laboratory determinations on rock samples overestimate the matrix porosity by a factor of 2 to 2.5.

To define the implications of these new data on the efficiency of geosphere retardation of radionuclides released from a repository near-field, scoping calculations based on two existing repository performance assessments were carried out. These revealed that the calculations of radionuclide retardation are relatively insensitive to the magnitude of both the porosity and the pore diffusion coefficient (in the ranges observed in typical repository host rocks). However, the depth of connectivity of the porosity does play an important role, potentially leading to a significant increase in the time of radionuclide breakthrough to the biosphere and to a significant decrease in peak activity of the radionuclides concerned.

The results of this study indicate that, for the two rock types studied here, connected porosity can be shown to exist at significant depths (at least up to several metres) into the matrix behind water conducting features in the rock. Although this work must be repeated in other rock types

---

<sup>1</sup> The Japan Nuclear Cycle Development Institute (previously PNC, Power Reactor and Nuclear Fuel Development Corporation).

(and eventually in repository host rocks) to obtain statistically meaningful results, the clear implications are that current assumptions about the retardation properties of the host rock matrix are over-conservative and probably need to be re-evaluated in future repository performance assessments. In addition, the results highlight the dangers of simply transferring laboratory-derived data on geosphere properties to *in situ* conditions.



## ZUSAMMENFASSUNG

Die Matrixporosität ist ein Schlüsselparameter für die Bewertung verschiedener Szenarien bei der Abschätzung der Radionuklidrückhaltung in der Geosphäre. Die Anzahl, Form und Grösse der Poren beeinflusst direkt die Radionuklidrückhaltung, der Verbindungsgrad dieser Poren (und folglich die Zugänglichkeit für Schadstoffe zu solchen Poren) muss jedoch ebenfalls in Betracht gezogen werden.

Bisher wurde bei der Bewertung der Rolle der Matrixporosität in der Sicherheitsanalyse meistens die Quantifizierung des Einflusses gestörter Proben auf die Geometrie und den Verbindungsgrad der Poren und deren Auswirkung auf die Abschätzung der Gesamtporosität sowie der geophysikalischen und hydraulischen Parameter generell vernachlässigt (oder die Effekte ausschliesslich qualitativ bewertet). Daher wurde die folgende Studie initiiert, mit der Zielsetzung, die Verbundenheit der *In-Situ*-Matrixporosität zu charakterisieren, den Einfluss der Probenaufarbeitung auf die Gesamtporosität zu quantifizieren und den Einfluss der Resultate auf Transportmodelle, die bei der Sicherheitsanalyse verwendet werden, zu bewerten.

Für die *In-situ*-Imprägnierung der für die Diffusion zugänglichen Gesteinsmatrix wurde eine neue Technik gemeinsam von der Nagra und JNC<sup>2</sup> entwickelt und erfolgreich im Bereich der Granodioritmatrix hinter einer wasserführenden Kluft im Felslabor Grimsel (FLG) der Nagra in der Schweiz und am Kamaishi *In-Situ*-Teststandort (KTS) von JNC in Japan angewendet. Nachdem die konservierte Gesteinsmatrix überbohrt worden war, wurde ein umfangreiches petrographisches, petropysikalisches und chemisches Untersuchungsprogramm an Proben aus allen gestörten Gesteinsbereichen durchgeführt (z. B. die vom Injektionsbohrloch beeinflusste umgebende Gesteinsmatrix, die vom Tunnelausbruch gestörte Zone etc.).

Die Ergebnisse dieser Studie ergaben, dass die strukturelle und mineralogische Heterogenität in der undeformierten Matrix des Grimsel-Granodiorits wichtig ist und den Typ und die Grösse der vorherrschenden Porosität beeinflusst. Es konnten vier verschiedene Porentypen unterschieden werden: Korngrenzenporen, Schichtsilikatporen, Lösungsporen und Mikrokluften. Sämtliche dieser Porentypen stellen ein verbundenes Netzwerk dar, das innerhalb des experimentellen Zeitrahmens für Harz zugänglich ist. Messungen der seismischen Geschwindigkeit ( $V_p$ ) als Funktion des Porenwasserdrucks, der Wassersättigung und Raumrichtung an *in situ* und im Labor imprägnierten Gesteinsproben ergaben Einschränkungen bei der Unterscheidung zwischen *In-situ*-Matrixporen und künstlich verursachten Poren. Der Vergleich der konventionellen Techniken zur Bestimmung der Porosität mit einer neu entwickelten Methode einer chemischen Analyse von Harz-erfüllten Poren zeigte, dass konventionelle Laborbestimmungen an Gesteinsproben die Matrixporosität um einen Faktor 2 bis 2.5 überschätzen.

Um die Auswirkungen dieser neu gewonnenen Daten auf das Rückhaltevermögen von aus einem Lagernahfeld freigesetzten Radionukliden in der Geosphäre zu definieren, wurden Überschlagsrechnungen basierend auf zwei bestehenden Sicherheitsanalysen für ein Tiefenlager durchgeführt. Diese ergaben, dass die Berechnung der Radionuklidrückhaltung relativ unempfindlich ist gegenüber der Grössenordnung von sowohl der Porosität als auch des Porendiffusionskoeffizienten (in den für typische Wirtgesteine beobachteten Wertebereichen). Jedoch spielt der Grad der verbundenen Porosität eine wichtige Rolle und führt möglicherweise zu einer deutlichen Zunahme der Radionukliddurchbruchzeit in die Biosphäre und zu einem deutlichen Rückgang der Peakaktivität der betroffenen Radionuklide.

---

<sup>2</sup> The Japan Nuclear Cycle Development Institute (früher PNC, Power Reactor and Nuclear Fuel Development Corporation).

Die Ergebnisse der vorliegenden Studie an den beiden untersuchten Gesteinstypen zeigen, dass eine verbundene Porosität in der Matrix hinter wasserführenden Klüften im Gestein in bestimmten Tiefenbereichen existiert (zumindest bis in einigen Metern Tiefe). Obwohl diese Arbeiten in anderen Gesteinstypen (und schliesslich auch in Wirtgesteinen) wiederholt werden müssen, um statistisch aussagekräftige Ergebnisse zu erhalten, kann aus den bisherigen Ergebnissen geschlossen werden, dass die gängigen Annahmen zu den Eigenschaften der Radionuklidrückhaltung der Wirtgesteinsmatrix zu konservativ sind und daher in künftigen Sicherheitsanalysen neu evaluiert werden müssen. Zusätzlich weisen die Ergebnisse auf die Gefahren einer simplen Übertragung von Labordaten bezüglich der Eigenschaften der Geosphäre auf *In-situ*-Bedingungen hin.

## RÉSUMÉ

La porosité de matrice est un paramètre clé lors de l'évaluation de différents scénarios pour l'estimation du retardement de radionucléides dans la géosphère. La quantité, la forme et la grandeur des pores influencent certainement le retardement des radioéléments, mais le degré d'interconnection entre les pores (et par là l'accessibilité des contaminants aux pores) doit aussi être pris en considération.

Jusqu'ici, la plupart des études sur le rôle de la porosité de matrice se sont passées de quantifier l'influence (ou l'ont évaluée seulement qualitativement) du dérangement de l'échantillon sur la géométrie et l'interconnection des pores, ainsi que son impact sur l'estimation de la porosité totale et des paramètres géophysiques et hydrauliques. C'est pourquoi cette étude a été mise en place, avec pour objectifs la caractérisation *in situ* du degré d'interconnection de la porosité de matrice, la quantification de l'influence de la préparation de l'échantillon sur la porosité totale, enfin l'estimation de l'impact des résultats sur les modèles de transport utilisés pour les évaluations de performance.

Une nouvelle technique d'imprégnation *in situ* de la matrice rocheuse accessible à la diffusion a été développée en commun par la Nagra et le JNC<sup>3</sup>, et mise en œuvre avec succès deux types de granodiorite, l'une située derrière une structure aquifère au laboratoire souterrain du Grimsel (GTS) en Suisse, l'autre au site de test *in situ* de Kamaishi (KTS) du JNC au Japon. Après avoir extrait la matrice rocheuse intacte par surcarottage, un vaste programme d'analyses pétrographiques, pétrophysiques et chimiques a été conduit sur des échantillons du matériel carotté hors de toute zone endommagée de la matrice rocheuse (p. ex. par le forage d'injection ou par l'excavation du tunnel).

L'étude a montré que l'hétérogénéité minéralogique et structurale de la matrice non déformée de la granodiorite du Grimsel est significative et qu'elle influence fortement le type et le développement de la porosité dominante. On a pu distinguer quatre types différents de pores: des pores aux limites de grains, des pores de feuillets silicatés, des pores de dissolution et des pores de microfractures. Tous ces types de pores présentent un réseau interconnecté accessible à la résine en des laps de temps comme ceux des expérimentations. Des mesures de vitesse sismique ( $V_p$ ) effectuées sur la roche imprégnée *in situ* et sur des échantillons au laboratoire, en fonction de la pression de confinement, de la saturation en eau et de l'orientation spatiale ont révélé une distinction nécessaire entre les pores de la matrice *in situ* et les pores induits artificiellement. La comparaison entre les techniques conventionnelles de détermination de la porosité et la nouvelle méthode consistant à analyser chimiquement la quantité de résine remplissant les pores a montré que les méthodes conventionnelles surestiment la porosité de matrice d'un facteur 2 à 2.5.

Afin d'évaluer les implications de ces nouvelles données sur l'efficacité du retardement dans la géosphère des radioéléments relâchés au voisinage d'un dépôt, on a effectué des calculs de portée sur les évaluations de performance existantes pour deux dépôts. Ils ont montré que le calcul du retardement des radioéléments est relativement peu influencé par l'ampleur et de la porosité et du coefficient de diffusion dans les pores (pour les fourchettes de valeur observées dans les roches d'accueil typiques pour des dépôts). Toutefois, la distance de pénétration de la porosité interconnectée joue un rôle important, car une plus grande distance peut conduire à un retard significatif du moment d'apparition des radioéléments dans la biosphère et à une diminution significative du pic d'activité des radioéléments concernés.

---

<sup>3</sup> The Japan Nuclear Cycle Development Institute (autrefois PNC, Power Reactor and Nuclear Fuel Development Corporation).

Cette étude montre que pour les deux types de granodiorites étudiées la porosité interconnectée peut être présente dans la matrice à des distances significatives (au moins plusieurs mètres) des structures aquifères. Bien qu'il faille encore répéter de telles investigations sur d'autres types de roche pour obtenir des résultats statistiquement significatifs, on peut déjà relever que les hypothèses actuellement admises sur les propriétés de retardement dans la matrice des roches d'accueil sont trop prudentes (pessimistes) et devront probablement être ajustées pour les futures évaluations de performance de dépôts. En outre, les résultats mettent en lumière le danger qu'il y a à simplement transposer des résultats de laboratoire sur les propriétés de la géosphère aux conditions *in situ*.

## TABLE OF CONTENTS

SUMMARY .....	I
ZUSAMMENFASSUNG.....	III
RÉSUMÉ .....	V
TABLE OF CONTENTS .....	VII
LIST OF TABLES .....	X
LIST OF FIGURES.....	XI
1 INTRODUCTION .....	1
1.1 Background to the project.....	1
1.2 Radionuclide retardation in the rock matrix .....	2
1.3 The Connected Porosity project (CP) .....	3
2 DEVELOPMENT OF AN <i>IN SITU</i> IMPREGNATION TECHNIQUE FOR CRYSTALLINE ROCK MATRICES.....	5
2.1 Aims and procedures .....	5
2.2 Design calculations and hydrotesting .....	6
2.3 Evaluation of resin and injection techniques .....	8
2.3.1 General characteristics of acrylic resins .....	8
2.3.2 Methods for resin stability evaluation .....	8
2.3.3 Evaluation procedure .....	10
2.4 Heating experiments .....	13
2.5 Conclusions .....	15
3 <i>IN SITU</i> PORE SPACE IMPREGNATION EXPERIMENT.....	17
3.1 Site description and geological overview .....	17
3.2 Experimental layout.....	18
3.3 Injection of resin and heating .....	20
3.4 Overcoring and sub-sampling.....	22
3.5 Summary.....	23
4 PETROGRAPHY OF GRIMSEL GRANODIORITE AND DEFINITION OF STRUCTURAL ELEMENTS AND PORE TYPES .....	25
4.1 Petrography of Grimsel granodiorite matrix.....	25
4.2 Structural elements .....	26
4.3 Pore types .....	27
4.4 Summary.....	30

5	PORE SPACE DESCRIPTION UNDER UV LIGHT AT DIFFERENT SCALES AND FREQUENCY COUNTING METHODS.....	31
5.1	Methods .....	31
5.2	Results .....	31
5.2.1	Pore space distribution on macroscopic scale.....	31
5.2.2	Pore space distribution on microscopic scale .....	34
5.3	Conclusions .....	37
6	SCANNING ELECTRON MICROSCOPE INVESTIGATIONS OF <i>IN SITU</i> POROSITY .....	41
6.1	Methods .....	41
6.2	Results and discussion .....	42
6.2.1	Visualisation of impregnated pore spaces with SEM .....	42
6.2.2	3-D reconstruction of impregnated pore space .....	43
6.3	Conclusions .....	45
7	UNIVERSAL-STAGE MEASUREMENTS AND DETERMINATION OF POROSITY, PERMEABILITY AND SEISMIC VELOCITIES .....	49
7.1	Methods .....	49
7.1.1	Sample reference system .....	49
7.1.2	Universal-stage measurements .....	49
7.1.3	Porosity and permeability measurements .....	50
7.1.4	Seismic velocities .....	50
7.2	Results .....	51
7.2.1	Petrography .....	51
7.2.2	Pore space fabrics .....	51
7.2.3	Porosity .....	55
7.2.4	Hydraulic conductivity .....	56
7.2.5	Seismic velocities .....	57
7.3	Conclusions .....	61
8	WATER SATURATION GRAVIMETRY, MERCURY INJECTION POROSIMETRY AND CHEMICAL ANALYSIS POROSIMETRY .....	63
8.1	Methods .....	63
8.1.1	Sample preparation .....	63
8.1.2	Water saturation gravimetry .....	64
8.1.3	Mercury injection porosimetry .....	65
8.1.4	Chemical analysis porosimetry .....	66

8.2	Results and discussion .....	67
8.2.1	Comparison of porosimetrical measurements on non-impregnated samples .....	68
8.2.2	Connected porosity and pore-size distribution of laboratory samples.....	69
8.2.3	Comparison of connected porosities for <i>in situ</i> and laboratory samples .....	70
8.3	Conclusions .....	72
9	ILLUSTRATING THE EFFECTS OF THE MAGNITUDE AND EXTENT OF CONNECTED MATRIX POROSITY ON RADIONUCLIDE TRANSPORT IN A FRACTURED GEOLOGICAL MEDIUM.....	73
9.1	Introduction .....	73
9.2	Model representation of the geosphere.....	73
9.3	Parameter values.....	74
9.4	Results .....	74
9.5	Discussion.....	76
9.6	Conclusions .....	76
10	CONCLUSIONS .....	81
11	ACKNOWLEDGEMENTS.....	84
12	REFERENCES .....	85

**LIST OF TABLES**

Tab. 2.4.1: Properties of heating oil Parapharm 68.....	14
Tab. 2.5.1: Properties of NHC-9 acrylic resin .....	15
Tab. 3.2.1: Technical data for the boreholes drilled for the final <i>in situ</i> experiment; all boreholes have an orientation subparallel to 144 / 07 .....	18
Tab. 3.3.1: Total mass of resin injected after 6 weeks.....	20
Tab. 3.4.1: Dimensions of overcores BOVE 97.004 to 007 with the positions of the slab surfaces .....	22
Tab. 4.3.1: Summary of pore type characteristics.....	27
Tab. 5.3.1: Summary of quantified parameters for all pore types.....	39
Tab. 7.2.2: Pressure dependent permeability and hydraulic conductivity of impregnated (imp) and non-impregnated (ni) samples in the direction parallel to the lineation (x) and perpendicular to the foliation (z).....	57
Tab. 8.2.1: Porosimetry data for the Grimsel granodiorite matrix, obtained through quantitative investigations; analytical errors listed were assessed for each technique as described in the preceding sections.....	68
Tab. 9.3.1: Nuclide-independent geosphere parameters .....	75
Tab. 9.3.2: Nuclide-dependent geosphere parameters .....	75



## LIST OF FIGURES

Fig. 1.1.1: Methodology of <i>in situ</i> resin impregnation .....	4
Fig. 2.1.1: Flow chart illustrating the procedure from the experimental concept to the main experiment .....	7
Fig. 2.3.1: Setup for the on site resin stability experiments on different tubing materials .....	9
Fig. 2.3.2: Schematic illustration of the chronology of the feasibility experiments and their results .....	11
Fig. 2.4.1: Comparison of calculated and measured matrix temperature.....	14
Fig. 3.1.1: Overview of ventilation drift at GTS.....	17
Fig. 3.2.1: Layout of the final <i>in situ</i> experiment in the ventilation drift.....	19
Fig. 3.3.1: Injection pressure and mass of injected resin (top); heating curves of temperature sensors in observation boreholes and of the heating element (below).....	21
Fig. 3.4.1: Intersections of the boreholes with the shear zone T.....	23
Fig. 4.3.1: Thin section photomicrographs of pore types under crossed nicols (left) and under UV light (right).....	29
Fig. 4.4.1: Pore type distribution in granodiorite matrix.....	30
Fig. 5.1.1: Drillcore mapping and position of slab surfaces .....	32
Fig. 5.2.1: General orientation of elliptic resin halo on slab surfaces.....	33
Fig. 5.2.2: x' and y' axis of ellipsoids of macroscopically visible pore space filling [cm].....	34
Fig. 5.2.3: Slab surfaces photographed under UV light (position of surface is indicated in photograph): a) BOVE 97.004, b) BOVE 97.005, c) BOVE 97.006, d) BOVE 97.007 .....	35
Fig. 5.2.4: a) Cross-section of the impregnated interval of overcore BOVE 97.006 between 1.28 m and 1.88 m, numbers 1 to 4 indicate the position of thin sections used for microscopic analyses; b) Cross-section of the same interval under UV light, the bright central partly reflects the injection borehole .....	36
Fig. 5.2.5: Distribution of different pore types perpendicular to injection borehole (vertical axis) and with increasing distance from the shear zone (horizontal axis): a) Grain boundary pores, b) sheet silicate pores, c) solution pores and d) microfractures.....	38
Fig. 6.2.1: BSE image of microfractures (orange arrows) within the Grimsel granodiorite matrix; the microfractures with apertures of larger than a few $\mu\text{m}$ were fully filled with resin .....	42
Fig. 6.2.2: BSE image of grain boundary pores showing various resin-filled pore spaces (orange arrows) with apertures ranging in size from about 100 nm up to a few $\mu\text{m}$ ; resin-free pore spaces (black arrows) are also identified along grain boundaries.....	42

Fig. 6.2.3:	BSE images ( $a_1$ and $a_2$ ) and corresponding photomicrograph (b) of pore types in the Grimsel granodiorite matrix, a disagreement in the appearance of the pore spaces is obviously seen between (a) and (b); (a) All pore spaces are not accessible to the resin (orange arrow: resin-filled pore space, black arrow: resin-free pore space), b) Labelled A, B and C are corresponding to the cases A, B and C, respectively, shown in Fig. 6.2.4.....	44
Fig. 6.2.4:	Schematic representations of three possible cases of resin impregnation, which could cause differences in the appearance of the pores between SEM examination and fluorescent microscopy .....	45
Fig. 6.2.5a:	Top, left and bottom views of 3-D reconstructions of rock sample (top) and <i>in situ</i> connected porosity (bottom); these 3-D images consist of 51 2-D images that are 10 $\mu\text{m}$ apart.....	46
Fig. 6.2.5b:	3-D representations of <i>in situ</i> connected porosity from different viewpoints, showing the "microchannel and barrier" structure that reflects the constrictive and tortuous geometry of the rock matrix .....	47
Fig. 6.2.5c:	3-D representations of <i>in situ</i> connected porosity in 3 segmented portions of the rock volume; the whole 3-D image from the same viewpoint is shown in Fig. 6.2.5b (middle) .....	48
Fig. 7.1.1:	Reference system of the sample orientation; a) schematic cube with foliation (XY-cleavage-plane) and lineation (x-direction), the arrows indicate the orientation of the thin sections, b) orientation of cylindrical samples for the permeability measurements, c) projection of the foliation and lineation in the Schmidt net, lower hemisphere, as used in the following.....	50
Fig. 7.2.1:	Pole figures of pores for the samples HS, SZ and LS in: (a) to (c) (001) cleavage planes of micas; (d) to (f) grain boundary pores in quartz; (g) to (i) microfractures in feldspars; and (j) to (l) bulk microfractures fabric .....	52
Fig. 7.2.2:	Schematic illustrations of pore orientation (coloured planes) in sample cubes for HS, SZ and LS with reference axes (x, y, z) .....	54
Fig. 7.2.3:	Porosity of impregnated and non-impregnated (ni) samples .....	55
Fig. 7.2.4:	Pressure dependent permeability/hydraulic conductivity of HS impregnated and non-impregnated (ni) in X- and Z-direction .....	56
Fig. 7.2.5:	Pressure dependent seismic velocity of the non-impregnated sample SZ and the impregnated sample HS of two selected propagation directions .....	59
Fig. 7.2.6:	Experimentally determined directional dependence of compressional wave velocities [ $\text{km s}^{-1}$ ] for the impregnated samples HS, SZ and LS: (a) and (b) $V_p$ as a function of confining pressure, (c) $\Delta V_p$ between 100 and 3 MPa confining pressure, (d) and (g) $V_p$ under dry conditions, (e) and (h) $V_p$ under saturated conditions; and (f) and (i) $\Delta V_p$ (sat - dry) as a measure of the microfracture induced anisotropy; Schmidt net, lower hemisphere .....	60
Fig. 7.2.7:	Seismic velocity [ $\text{km s}^{-1}$ ] of the non-impregnated sample SZ: (a) at a confining pressure of 3 MPa, (b) at a confining pressure of 100 MPa, (c) $\Delta V_p$ between 100 and 3 MPa confining pressure, (d) $V_p$ under dry conditions, (e) $V_p$ under saturated conditions, and (f) $\Delta V_p$ (sat - dry) as a measure of the anisotropy induced by microfractures; Schmidt net, lower hemisphere.....	61

Fig. 8.1.1:	Sub-samples A – G and the reference material, used for quantitative porosimetry investigations.....	63
Fig. 8.2.1:	Size distribution of mercury injectable porosity in the Grimsel granodiorite; vertical axis corresponds to the relative abundance of pore size .....	69
Fig. 8.2.2:	Estimated size distribution of <i>in situ</i> porosity in the Grimsel granodiorite matrix; calculation based upon results from mercury injection porosimetry on sub-samples C, D and E.....	72
Fig. 9.2.1:	Schematic illustration of the geosphere model, showing an area <i>A</i> in a planar section through the host rock normal to the direction of groundwater flow and channels passing through the plane that convey the groundwater (large arrows); matrix diffusion is assumed to occur within the shaded regions adjacent to the channels.....	76
Fig. 9.4.1:	The geosphere releases of <sup>79</sup> Se for the cases J-2-1 to 6 (upper figure) and K-1-1 to 6 (lower figure), compared to the near-field release of this radionuclide .....	77
Fig. 9.4.2:	The geosphere releases of <sup>135</sup> Cs for the cases J-2-1 to 6 (upper figure) and K-1-1 to K-1-6 (lower figure), compared to the near-field release of this radionuclide .....	78
Fig. 9.4.3:	The geosphere releases of <sup>237</sup> Np (upper figure) and <sup>99</sup> Tc (lower figure) for the cases K-1-1 to K-1-6, compared to the near-field releases of these radionuclides.....	79



## 1 INTRODUCTION

*W.R. Alexander, A. Möri and M. Adler*

### 1.1 Background to the project

The joint Nagra-JNC Radionuclide Migration Programme (RMP<sup>4</sup>) has been running for over ten years in Nagra's Grimsel Test Site in the central Swiss Alps (KICKMAIER et al. 2001). The programme is specifically aimed at the further development of conceptual models of radionuclide transport in the geosphere, rigorously testing the applicability of current transport codes to quantify radionuclide migration *in situ* and assessing how successfully laboratory sorption data may be extrapolated to *in situ* conditions to predict radionuclide retardation in the geosphere (see McKINLEY et al. 1988, ALEXANDER et al. 1992, FRICK et al. 1992, SMITH et al. 2001a and b, OTA et al. 2003 for an overview). A large series of field tracer migration experiments (the MI project) has been carried out in a hydrologically well characterised water-bearing, complex fracture (or shear zone). The work began with simple, non-sorbing fluoresceine (a fluorescent dye, also known as uranine), <sup>3</sup>H, <sup>3,4</sup>He, <sup>82</sup>Br and <sup>123</sup>I and increased in complexity through weakly sorbing <sup>22,24</sup>Na, <sup>85</sup>Sr and <sup>86</sup>Rb to a final, long-term experiment with moderately sorbing <sup>134,137</sup>Cs. The radionuclides were injected into a dipole flow field where the flow path length, dipole width (or shape) and flow velocity were all varied. After a considerable learning period, generally good fits could be obtained between transport code blind predictions and subsequent field tracer breakthrough curves, suggesting that the transport codes tested provided a reasonable representation of *in situ* conditions.

The programme then went further in two main respects: first, strongly retarded, chemically more complex radionuclides (<sup>60</sup>Co, <sup>75</sup>Se, <sup>99</sup>Tc, <sup>113</sup>Sn, <sup>152</sup>Eu, <sup>234,235</sup>U, <sup>237</sup>Np and stable Mo) were injected into the same water-conducting shear zone which has been used for the previous ten years work and second, the sites of *in situ* radionuclide retardation were physically defined (in the excavation project EP) and not just assumed from the breakthrough curves as previously. The second part follows on partly from the first in that the injected strongly retarding radionuclides travel through the experimental shear zone so slowly (taking years to decades for complete breakthrough compared with hours to months for weakly sorbing tracers) that it was impossible to sit back and wait for their appearance at the extraction borehole as was previously the case. Following the injection of the radionuclides, a specially developed epoxy resin was injected into the experimental shear zone to immobilise the shear zone without either physical or chemical disturbance (see ALEXANDER et al. 2001 for details). The entire experimental zone (approximately one tonne of rock) was excavated and sub-samples taken to the laboratory to assess the extent of heterogeneity of transport of each radionuclide within the shear zone, based on both laboratory data and model assumptions about the distribution of flowpaths (see MÖRI et al. 2001 for details).

In addition, a second retardation mechanism was studied in the programme, namely matrix diffusion. Work carried out on natural decay series disequilibria showed that matrix diffusion occurs in the low-porosity rock matrix close behind the experimental shear zone (ALEXANDER et al. 1990a and b). It was decided that this merited further, detailed study but, in a break from traditional laboratory-based studies of matrix porosity (due to the desire to avoid artefacts associated with sample disturbance: see, for example comments in CHERNIS 1981, 1983, 1984 and FRICK et al. 1993), a technique for the examination of *in situ* porosity was developed and implemented and provides the basis for this report.

<sup>4</sup> The RMP includes the MI (migration), EP (excavation) and CP (connected porosity) projects. Previously, EP and CP have been labelled RRP (Radionuclide Retardation Project).

## 1.2 Radionuclide retardation in the rock matrix

The term matrix diffusion is applied to the process by which a solute, flowing in distinct fractures, penetrates the surrounding rock. Diffusion into this rock occurs in a connected system of pores or microfractures, and diffusion through the solid phase is insignificant by comparison (see the review of VALKIANEN 1992, for example). The importance of matrix diffusion in the context of a radioactive waste repository is that it greatly enlarges the area of rock surface in contact with advecting radionuclides from just the fracture surface to a portion of the bulk rock (NERETNIEKS 1980, GRISAK & PICKENS 1980, RASMUSON & NERETNIEKS 1981, HADERMANN & RÖSEL 1985).

The matrix diffusion theory proposes that dissolved radionuclides will diffuse from a water-filled fracture, through any fracture coating layer, into the rock matrix and, if they are reactive, sorb onto the inner surface of the pores or else remain dissolved within the immobile pore-water. This process can be envisaged as an extreme case of a dual porosity medium, in which advective flow occurs entirely within the fracture system, or primary porosity, whilst all solute transport in the bulk rock, the secondary porosity, takes place by diffusion (see, for example, BARENBLATT et al. 1960, GRISAK & PICKENS 1980). The porosity of the rock matrix can be very small (about 0.1 to 1 %) in many hard rocks and solute loss by diffusion into the matrix is likely to be slow. The impact of matrix diffusion will, as a consequence, not be significant along short or rapid flow paths but, for the longer and slower paths likely in a repository host rock, may result in a significant reduction in the maximum concentration of radionuclides in the groundwater entering the biosphere. This process is particularly important if the resulting transport time to the biosphere is greater than the half life of the radionuclide, since the total release can be reduced by several orders of magnitude (see for example, NERETNIEKS 1980, for discussion). In addition, pulse releases can be spread over longer time periods, thereby decreasing release concentrations by a process of temporal dilution (NAGRA 1985). For non-sorbed radionuclides, this process also represents an important retardation mechanism, since these radionuclides would otherwise be transported at the advection rate of the groundwater. For sorbing nuclides, the importance of matrix diffusion lies in the fact that it provides a mechanism for enlarging the rock surface in contact with the advecting solute, from that of the fracture surfaces and their infills, to a much larger portion of the bulk rock.

The theoretical basis for matrix diffusion is thus fairly well established. There are, however, different views regarding the volume of rock that would be available for matrix diffusion; *ie* the extent of connected porosity. In the KBS-3 performance assessment (KBS 1983) for example, it was assumed that matrix diffusion is limited only to dead-end pores whilst the Project Gewähr performance assessment (NAGRA 1985) assumed the matrix diffusion was limited to a micro-fractured damage zone (e.g. taken as 1 mm for calculations with limited matrix diffusion, based on the altered zone in aplite/pegmatite dykes).

Clearly then, the matrix diffusion concept required experimental verification and work has been carried out on limestone (GARRELS et al. 1949), sandstone (KLINKENBERG 1951, BRADBURY et al. 1986), claystone (MAZUREK et al. 1996) and crystalline rocks (SKAGIUS & NERETNIEKS 1982, 1983, 1985a and b, 1986, TORSTENFELT et al. 1982, BRADBURY & STEPHEN 1986, MONTOTO et al. 1992, HEATH & MONTOTO 1996). One significant problem, however, is that the work is conducted, out of necessity, on samples disturbed by collection and preparation. This leads, for example, to de-stressing of the rock (an inevitable consequence of removal to the laboratory) inducing non-reproducible changes to the pore geometry.

Other perturbations due to sample cutting or grinding will also change both the pore geometry and sorption properties of the rock, indicating that the laboratory results must be treated with some caution. In general, all of the changes induced in the samples (see MCKINLEY 1989a and

1989b for further details) tend to cause overestimation of the rock diffusivity, leading to an overestimation of matrix diffusion which is, in turn, non-conservative in the performance assessment sense as it leads to an apparently greater degree of radionuclide immobilisation in the far field.

Attempts have also been made to verify matrix diffusion by more complex experiments which, by confining the (larger) rock samples under high pressures (e.g. BRACE et al. 1968, BISCHOFF et al. 1987, DREW & VANDERGRAAF 1989), hoped to re-create the *in situ* conditions more precisely. There are still many problems with such experiments: the low hydraulic conductivity means that unrealistically high pressure gradients have to be applied to the infiltrating fluids in order to produce breakthrough of radionuclides within reasonable time scales plus there is no way to guarantee that the re-established confining pressures will recreate anything like the original pore geometry. In fact, in one study (SKAGIUS & NERETNIEKS 1986) which attempted to quantify the degree of disturbance, it was estimated that laboratory produced data probably overestimate *in situ* diffusion coefficients by several orders of magnitude. These overestimates should be treated as minimum values, however, as the study was conceptually simplistic, assuming that re-stressing core samples with simulated overburden pressures would represent undisturbed *in situ* conditions.

### 1.3 The Connected Porosity project (CP)

In the Connected Porosity (CP) project, resin impregnation of the rock matrix with a very low viscosity acrylic resin has been carried out, followed by the recovery of samples from the undisturbed rock matrix, to allow the form and distribution of porosity in the undisturbed rock matrix to be investigated in detail. Specifically, the depth of matrix porosity connected to the experimental shear zone has been studied as well the form of pore connectivity. This has provided new information on the pore volumes which could be available to retard radionuclides moving through repository host rocks, and a direct comparison between the new experimental data produced in CP with that from EP should produce a detailed description of porosity distribution in and around a water conducting feature.

The CP Project started in 1996 with a suite of different feasibility studies. Significant efforts were required to determine the optimum composition of the resin and the conditions of resin injection which would induce no damage to the rock structure. The preparatory work included laboratory and *in situ* experiments (see Chapter 2) which provided the basis for the final *in situ* rock matrix immobilisation experiment (Chapter 3). Fig. 1.1.1 gives an overview of the experimental layout of the *in situ* impregnation procedure. Different analytical techniques were then assessed and applied in order to characterise and conceptualise *in situ* pore space geometry and distribution in the excavated rock matrix (Chapters 4 to 8). Scoping calculations based on the new data were carried out (Chapter 9) to assess the likely implications on estimates of radionuclide retardation in repository host rocks. Finally, the results were summarised (Chapter 10) and the implications for repository performance assessments noted along with recommendations for future areas of work. It should be noted that no attempt is made to synthesise the four RMP reports here, rather this is left to ALEXANDER et al. (2002).

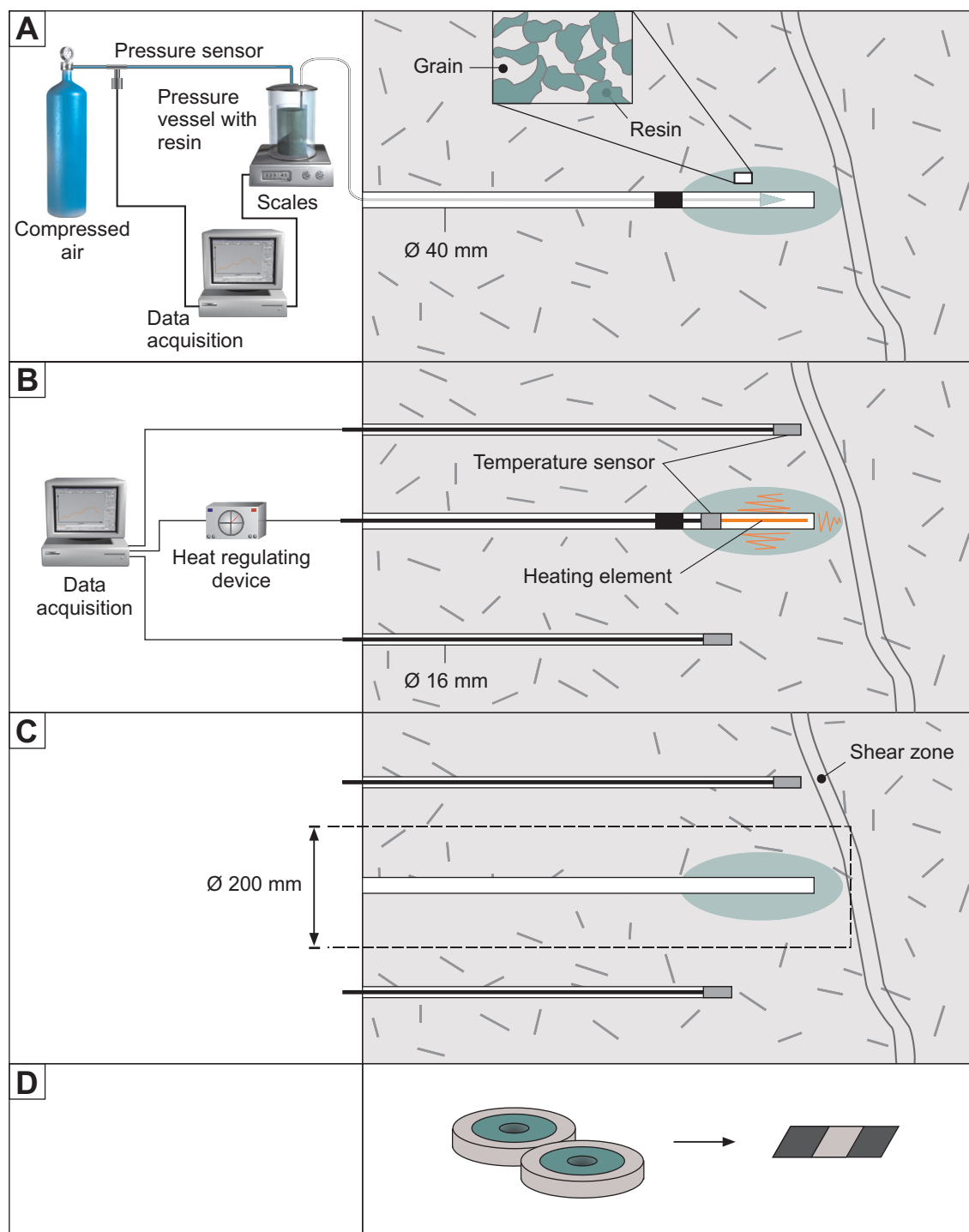


Fig. 1.1.1: Methodology of *in situ* resin impregnation

A: injection of the acrylic resin into the undisturbed<sup>5</sup> rock matrix. B: polymerisation of the resin by means of a heat shock. C: overcoring of the resin impregnated zone. D: pore space analysis in thin sections.

<sup>5</sup> No artificial influences affected the rock matrix outwith the drilling of the injection and temperature observation boreholes.



## 2 DEVELOPMENT OF AN *IN SITU* IMPREGNATION TECHNIQUE FOR CRYSTALLINE ROCK MATRICES

*A. Möri, C. Bühler, P. Haag, K. Ota and M. Mazurek*

### 2.1 Aims and procedures

Investigation of true matrix porosity requires *in situ* conservation of the pore spaces in the rock prior to excavating the impregnated rock mass for laboratory analysis. Several potential methods for *in situ* impregnation of a granitic rock matrix were envisaged at the beginning of this experiment, including freezing of the water saturated rock matrix, injection of cement grouts and injection of resin. In the end, both immobilisation by freezing and by injection of cement grouts were rejected in favour of resin injection. In the case of the freezing technique, the expansion of water on freezing was found to damage the rock with disruption of the pore spaces and extension of fractures (WATANABE et al. 1993). Cementitious grouts were rejected because they cannot penetrate the fine pore spaces in the rock matrix and they produce hyperalkaline fluids which can react with the pore waters and minerals. The selection and development of a suitable resin was found to be the most promising approach due to the possibility to easily modify the physical properties of a basis resin formula in order to obtain good penetration into fine pore space combined with ease of handling, significant structural strength and a polymerisation (hardening) which is not affected by the rock or the pore water. It should, however, be noted that the specific resin formulation used reflects the physico-chemical conditions in the two rock types studied and so application of the resin to other rock types would have to take this into account.

As part of the assessment procedure for resin impregnation, the C-14-PMMA (<sup>14</sup>C-Polymethylmethacrylate) method applied to Grimsel granite matrix samples in laboratory experiments by HELLMUTH & SIITARI-KAUPPI (1998) was also evaluated. The advantages of this method are the good impregnation properties of the resin and the post impregnation analytical methods (e.g. autoradiography combined with digital image processing) with image definition below the 0.5 µm resolution limit of optical procedures. However, regarding *in situ* applications, the use of active tracer (<sup>14</sup>C) in the PMMA resin and polymerisation initiation by radiation greatly increases complexity in the field<sup>6</sup>. Therefore it was decided to develop an acrylic resin in which polymerisation is initiated by heat as this promised to be the most practicable technique in the field.

Resin impregnation is routinely used in geological laboratories to stabilise rock samples before sub-sampling, grinding and polishing. However, the requirements of its use in the final CP experiment were more stringent and significant effort was put into determining the optimum resin composition. Given the physical properties of the rock and the need for complete impregnation and visualisation of pore space, the resin required the following characteristics:

- A low viscosity, allowing penetration into fine pore space of the matrix.
- A long processing time (potlife) in order to allow for long injection times which are required by the very low hydraulic conductivity of the matrix of around  $10^{-10}$  to  $10^{-12}$  m s<sup>-1</sup> (VOMVORIS & FRIEG 1992).
- Constancy of volume during polymerisation in order to avoid deformation of the original pore space.

<sup>6</sup> To achieve polymerisation at depth in the rock matrix will, in any case, probably require an unreasonably active <sup>60</sup>Co source. However, new experiments with a chemical initiation of PMMA polymerisation are under way at STUK (Finland) in order to increase *in situ* applicability of this method (K.-H. HELLMUTH, pers. comm. 2001).

- Miscibility with a fluorescent agent for visualisation of the pore space under UV light.
- Minimum tensile strength of 3 MPa after hardening to allow overcoring and sample preparation.
- Minimal uptake of water after polymerisation in order to preserve impregnation during overcoring and preparing this sections.

Heat flux calculations in the granodiorite and design calculations of the expected resin injection time were performed prior to the evaluation of the resin composition, appropriate injection equipment materials and injection and heating techniques.

The optimum composition of the resin was developed in a step-wise procedure: different resins were tested on Grimsel granodiorite specimens in the laboratory and *in situ* at the Grimsel Test Site (GTS). In case of failure, the formulation of the resin was modified and the new resin was again tested in the laboratory and *in situ*. The *in situ* experiments also aimed at the development of appropriate injection techniques and equipment. The results of the feasibility experiments are discussed below and formed the basis of the final *in situ* impregnation experiments in the GTS and in JNC's Kamaishi *In Situ* Test Site (KTS) in Japan which provided the sample material for analytical work. The procedure from the planning phases to the final experiment is illustrated in Fig. 2.1.1.

## 2.2 Design calculations and hydrotesting

To begin the heat flux calculations, the average thermal conductivity of the Grimsel granodiorite and of the acrylic resin was determined by the Swiss Federal Institute of Technology (ETH), Zürich (for details see MÖRI et al. 1996). The measurements revealed values between 2.30 and 3.23 W m<sup>-1</sup> K<sup>-1</sup> for the Grimsel granodiorite and a value of 0.55 W m<sup>-1</sup> K<sup>-1</sup> for the acrylic resin. The measurements on the rock samples gave no indication of a direction dependence in the thermal conductivity, despite evidence of slight cleavage and stretching lineation observed on matrix samples near the shear zone.

Two approaches for heat flux calculations were followed, both assuming a working temperature of the heating element of 80 °C and a resin polymerisation temperature of 40 °C (for details see MÖRI et al. 1996). A first approach assumed that the heating element would be in direct contact with the borehole walls. These calculations showed that, after two days of heating, the required polymerisation temperature of 40 °C could be achieved up to a distance of 10 cm into the rock matrix. A second calculation took the remaining resin in the injection borehole between the borehole wall and the heating element into account. The result is a much lower temperature at the transition into the granodiorite due to the insulating effect of the resin. These calculations gave a stable maximum temperature of only 24 °C at a distance of 20 cm from the borehole wall after about 72 hours. This heating / polymerisation temperature was found to be too close to the given mean rock temperature of about 14 °C and spontaneous early polymerisation could not be excluded due to the low difference in working and heating temperature. In order to fully evaluate the effective heat distribution in the rock and to increase rock temperature during heating, it was decided to perform heating tests during the *in situ* feasibility experiments (see Chap. 2.4 and Fig. 2.4.1).

Transmissivity of the rock matrix at the experimental site was determined by two pulse tests in the injection borehole of the first *in situ* feasibility experiment at 5 and 10 bar injection pressure. Apart from compliance effects, the injected volume in both tests was below 1 g and the calculated transmissivities for the rock matrix in Grimsel granodiorite were found to be between  $1.0 \times 10^{-11}$  and  $6.6 \times 10^{-11}$  m<sup>2</sup> m<sup>-1</sup> at the test location.

Rough design calculations based on an estimation of the amount of resin to be injected and the expected injection time were performed with the numerical well-test-simulation model GTFM<sup>7</sup> from Solexperts (for details see GRISAK et al. 1985). With a K-value of  $1 \times 10^{-12} \text{ m s}^{-1}$  and an injection pressure of 10 bars, the resulting injection mass was determined to be about 0.21 litres for a cylindrical pore volume with a radius of 10 cm around the injection interval ( $l = 70 \text{ cm}$ ). Simulated injection time would be 19 days (assuming 1 % porosity).

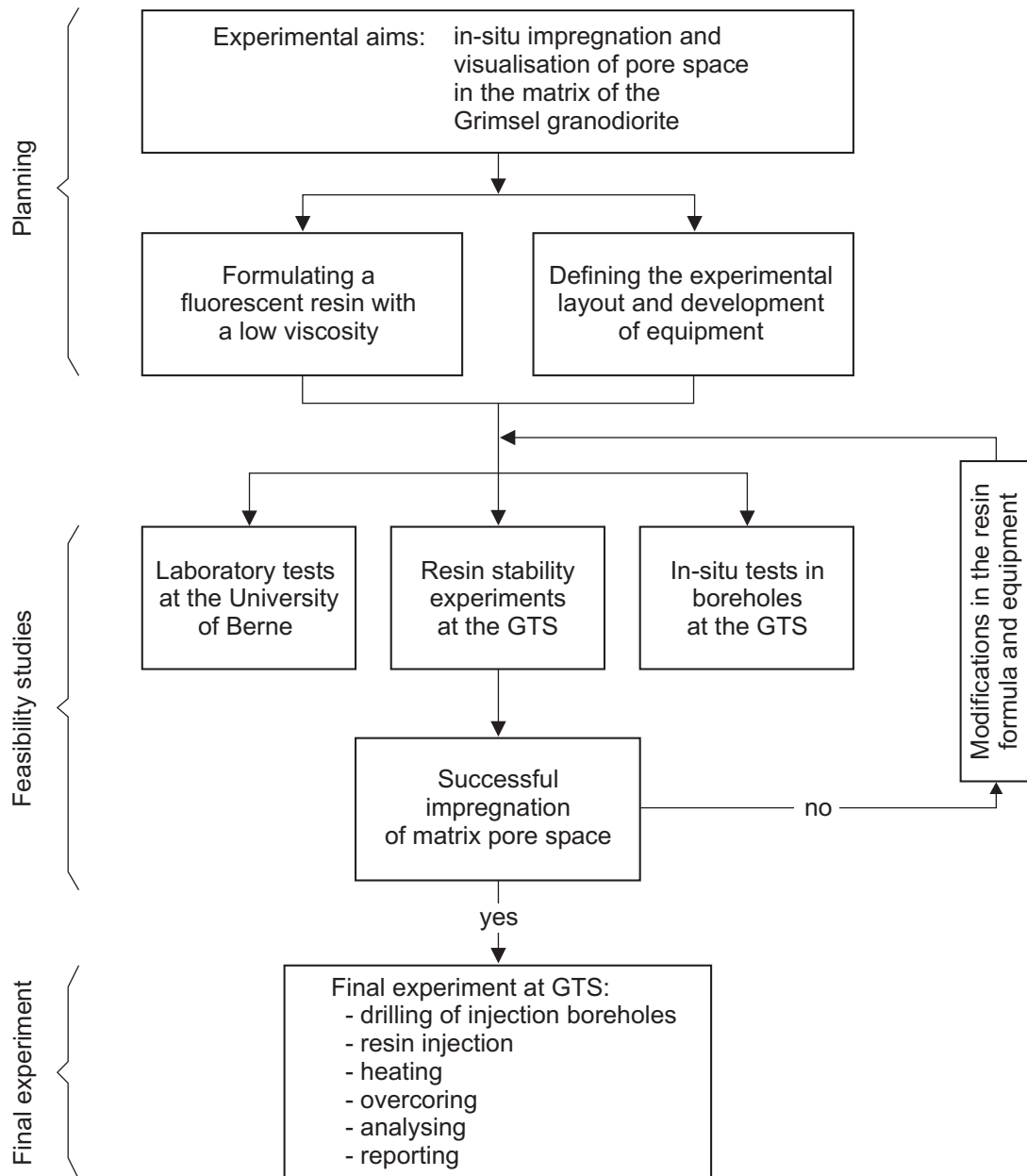


Fig. 2.1.1: Flow chart illustrating the procedure from the experimental concept to the main experiment

<sup>7</sup> Note that these calculations do not include the influence of capillary suction effects (for details see NERETNIEKS 1985).

## 2.3 Evaluation of resin and injection techniques

### 2.3.1 General characteristics of acrylic resins

Unlike epoxy resins or polyurethanes, some acrylic resins are completely miscible with water which allows formulation of a resin with a very low viscosity. The polar molecules of the acrylic resins have very good wetting properties leading to a high penetration capacity which plays a key role in the impregnation of matrix pores.

Acrylic resins have the ability to harden by a free radical initiated chain reaction of only one monomer (polymerisation). This polymerisation can run spontaneously or be triggered by adding an initiator which, in turn, can be activated by heat, irradiation (e.g. UV,  $\gamma$ -radioactivity or microwaves) or by redox reactions. The decrease in volume (shrinkage) of acrylic resins can be compensated for by the addition of free water into the system. The use of different types of initiators provides the possibility to modify the potlife of acrylic resins (time span where the resin remains at low viscosity and can be processed with the injection equipment) under the given boundary conditions such as ambient temperature, pore water chemistry or types of material which are in contact with the resin.

On the other hand, acrylic resins always need an inhibitor in order to prevent spontaneous polymerisation which could interrupt injection. Common inhibitors for resins with the necessary characteristics for the planned field experiment require the presence of oxygen in the system to fulfil their task.

An optimal balance between initiator and inhibitor must be found, on the one hand to prevent early polymerisation of the resin in the rock at the given ambient temperature as long as the injection lasts and, on the other hand, to ensure full polymerisation at the achieved rock temperature during heating. The target temperature for polymerisation was set at 40 °C which was found to be realistic with regard to the expected rock temperature to be achieved by heating and which is not too close to the ambient temperature in the GTS tunnels.

### 2.3.2 Methods for resin stability evaluation

Impregnation tests were first performed in the laboratory under conditions similar to those envisaged for the *in situ* tests. Successful impregnation under laboratory conditions was considered to be a pre-requisite for field tests (resin stability experiments in the gallery and *in situ* injections) at the GTS.

#### Laboratory experiments

The laboratory experiments were conducted on both air-dried and water-saturated Grimsel granodiorite samples. Water saturation was achieved by leaving the sample in a bucket of water for about one week. Saturation by this method clearly is not fully achieved, but this was deemed of little relevance for the scope of the tests. It was planned to evacuate air-dried samples prior to resin impregnation but the acrylic resin quickly evaporated under vacuum conditions and damaged the pressure chamber and vacuum pump system. Although other techniques for rock sample impregnation under vacuum are known (see, for example, SKAGIUS & NERETNIEKS 1982), it was decided that all subsequent tests would be performed without evacuation as this was, in any case, more appropriate to the *in situ* conditions. The pressure for the laboratory impregnations was in the range of 6 to 13 bars and impregnation time was 16 hours. The samples were then put in an oven and heated at 70 °C for 1 hour in order to achieve full poly-

merisation. Standard thin-sections were then prepared and the rock was cut such that each section contained a profile from the sample surface into the matrix.

### On site resin stability experiments

In addition to the *in situ* impregnation experiments, some resin stability experiments were performed at the GTS. The aim of these tests was to check the long term influence of ambient temperatures in the tunnel, assess potential reaction with equipment and define the effects of Grimsel granodiorite on polymerisation of the resin. A set consisting of four stainless steel tubes and one polyamide tube (Fig. 2.3.1) was filled with the resin and pressurised with compressed air to 10 bars. The tubes were reopened after a few weeks and the polymerisation behaviour of the resin checked. For the resin stability experiments performed directly in the granodiorite, the resin was poured into vertical boreholes ( $\varnothing$  40 mm) closed with a plastic lid and reopened after some weeks to check the polymerisation behaviour of the resin.

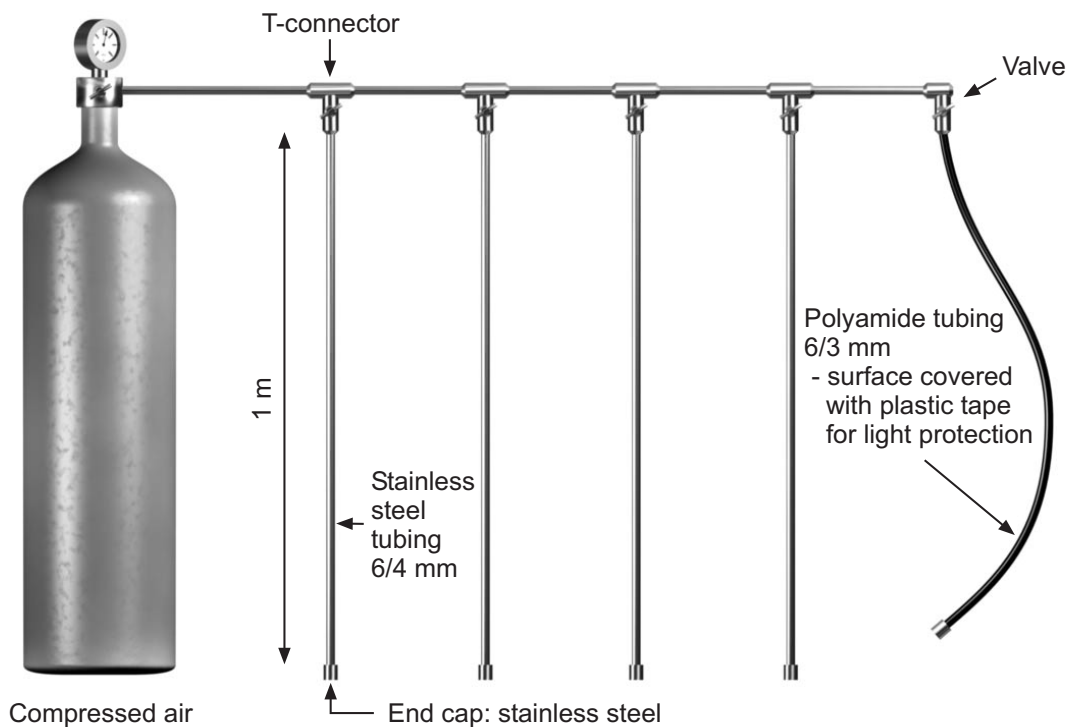


Fig. 2.3.1: Setup for the on site resin stability experiments on different tubing materials

### *In situ* feasibility experiments

The *in situ* feasibility experiments were performed at the GTS in the granodiorite matrix (in a zone with a weak cleavage). Sub-horizontal injection boreholes ( $\varnothing$  35 mm) with a length of 0.7 – 1.3 m were drilled. Parallel observation boreholes ( $\varnothing$  16 mm) were drilled at differing distances from the injection borehole. The injection borehole was equipped with a single packer system containing a heating system (heating wire and thermocouple). The borehole was filled with resin prior to packing-off the interval and connection to the injection vessel. The resin was pressurised by nitrogen or compressed air at pressures up to 10 bars. During the injection

period, which lasted between 4 to 15 days depending on the resin tested, the resin flow rate into the rock matrix was automatically monitored via weight loss measurement of the resin in the vessel. The injection phase was followed by a heating period where the temperature in the heating element was set to 80 °C and temperatures in the observation boreholes was monitored. The duration of the heating period was in the range of 2 to 4 weeks after which the packer system was removed and the injection borehole was overcored. The recovered core samples were then macroscopically and microscopically analysed under UV light in order to assess the extent and quality of resin impregnation of the pore space within the rock matrix (see Fig. 1.1.1).

### 2.3.3 Evaluation procedure

A total of 12 feasibility tests were performed until the optimum resin composition, appropriate injection equipment materials and injection and heating techniques were defined. The resins were named 'NHC' followed by a number indicating the version of the modification. Successfully impregnated rock samples have been analysed by UV microscopy to assess the quality and extent of resin impregnation (for details see also MÖRI et al. 1996). The experimental chronology and results are shown in Fig. 2.3.2.

#### Step 1: Laboratory investigation of the impregnation properties of two fluoresceine-doped acrylic resins NHC-1 and NHC-2<sup>8</sup>

These two single component resins showed no visible impregnation of pore space and this was thought to be mainly due to the following effects: i) a high surface tension at the resin rock interface prevents the resin from entering the pore spaces and / or ii) due to solubility problems, the fluorescent agent in the resin coagulates into aggregates whose size exceeds that of the matrix pores (in this case the resin enters the pore space but the fluorescent agent does not). Closer examination of the samples clearly showed that the latter effect had occurred, namely the resin had indeed filled all the pores but the dye had been filtered out and excluded from the smaller pores. As far as the authors were aware, no reports of such observations exist in the literature and so this mechanism was not expected to occur.

As yet, the process is not fully understood, but it was decided to change the procedure and the following changes in resin composition were initiated: addition of a surfactant to improve the wetting properties of the resin and the use of eosine instead of fluoresceine (Fluorol yellow-088, BASF) as fluorescent agent because eosine is more readily soluble in water and was therefore expected to be also in acrylic resins.

#### Step 2: Laboratory investigation of the impregnation properties of eosine-doped acrylic resin NHC-3

The new resin NHC-3 (based on NHC-1) showed good impregnation of pore space for both air-dried and water-saturated samples and was thus considered to be suitable for a preliminary *in situ* experiment.

---

<sup>8</sup> NHC-2 is based on NHC-1 but with a different cross-linking agent, responsible for polymerisation (chain forming).

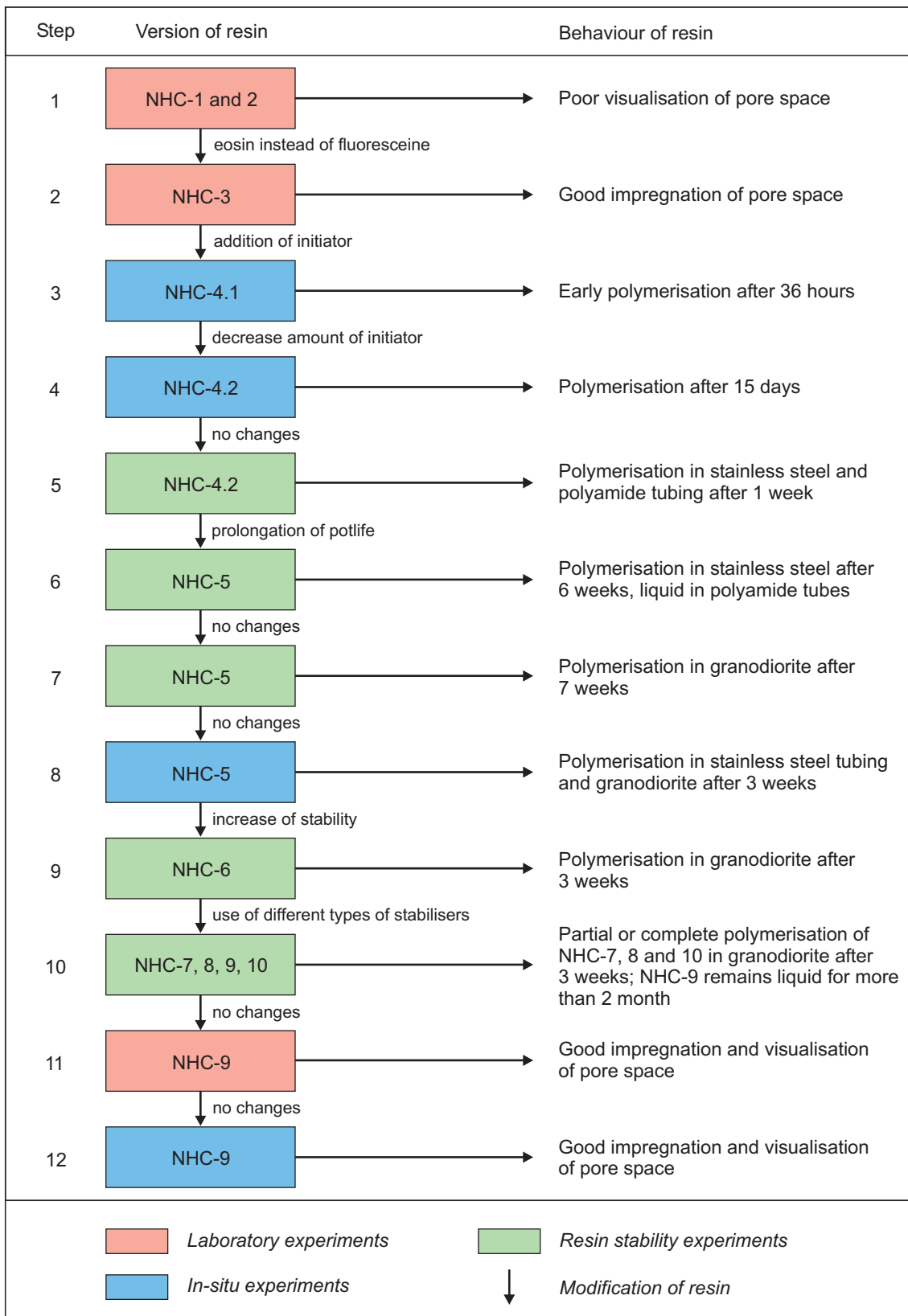


Fig. 2.3.2: Schematic illustration of the chronology of the feasibility experiments and their results

**Step 3: First *in situ* testing of injection equipment and resin NHC-4.1 with 3 % initiator**

Based on design calculations of heat flux in the granodiorite, it was decided to change the initiator of resin NHC-3 and set the polymerisation temperature at 30 °C. This modification reduced the potlife of the resin from 6 month for NHC-3 down to 1 month. The *in situ* injection of NHC-4.1 was only partially successful, the main problem being early spontaneous polymerisation of the resin after 36 hours. This was attributed to the use of nitrogen as the pressurising medium during injection of the resin which interfered with the inhibitor (decrease of the partial pressure of oxygen in the resin), and to too large a volume of resin in the injection vessel. It was therefore decided to use compressed air, to reduce the amount of initiator in the resin in order to elongate potlife again and to minimise the volumes within the injection equipment.

**Step 4: Second *in situ* testing of injection equipment and resin NHC-4.2 with 2 % initiator**

The modified resin formula, the use of pressurised air and the modified injection equipment (smaller injection vessel) led to a slight increase in the potlife of the resin but polymerisation in the tubing and the borehole interval occurred after only 15 days without heating.

**Step 5: On site resin stability experiment on NHC-4.2 in stainless steel and polyamide tubing**

In order to check the influence of light and tubing material at ambient tunnel temperatures (14 °C) on the stability of the resin, a resin stability experiment was performed in the GTS (see Fig. 2.3.1). The resin polymerised in stainless steel and polyamide tubing after only one week.

Up to that point, the fluorescence and viscosity properties of the resin were felt to be satisfactory. In contrast, the potlife of the resin had to be extended in order to allow longer injection periods of at least 4 weeks. A new resin NHC-5 was therefore formulated (based again on NHC-3 but with increased eosine content) and which had a longer potlife than NHC-4.2.

**Step 6: On site resin stability experiment on NHC-5 in stainless steel and polyamide tubing**

The new resin NHC-5 polymerised in stainless steel tubes after six weeks and remained liquid in polyamide tubing over more than one month.

**Step 7: On site resin stability experiment on NHC-5 in granodiorite**

As the previous experiment had shown that the NHC-5 polymerisation behaviour is influenced by the material in contact with the resin, its stability in granodiorite was checked directly. A borehole in the GTS was filled with resin NHC-5 and closed with a plastic lid. The resin was found to have polymerised completely after 7 weeks in the borehole.

**Step 8: Third *in situ* testing of injection equipment and resin NHC-5**

Early polymerisation occurred in the stainless steel tubing and in the injection borehole, while resin in the polyamide tubing was still liquid after 3 weeks. Subsequent modification of the resin formulation aimed at increasing the stability of the resin at 14 °C. The polymerisation temperature of the new resin NHC-6 was maintained at 40 °C and steel parts on the injection equipment were replaced whenever possible by polyamide.



#### **Step 9: Resin stability experiment on NHC-6 in granodiorite**

The new resin, NHC-6, polymerised in the borehole after 3 weeks. After this negative result, four new resins NHC-7, 8, 9, 10 were formulated with different types of stabilisers and tested at GTS.

#### **Step 10: Resin stability experiment on NHC-7, 8, 9, 10 in granodiorite**

After 3 weeks, the resins NHC-7 and 8 showed an increase in viscosity, while NHC-10 was completely polymerised. In contrast, NHC-9 was still liquid after 2 months.

#### **Step 11: Investigation of impregnation properties of resin NHC-9 in the laboratory**

Resin NHC-9 showed good impregnation of pore space for both air-dried and water-saturated samples.

#### **Step 12: Fourth *in situ* testing of injection equipment and resin NHC-9**

Injection of the resin was carried out at an increased pressure of 15 bars to increase the injection rate. The resin remained liquid during the entire injection period of 4 weeks and polymerised after heating. Microscopic analysis showed good impregnation and visualisation of pore space in an area of about 5 cm around the injection borehole.

### **2.4 Heating experiments**

To heat the rock, it was planned to introduce a heating element (which could attain a maximum temperature of about 200 °C) into the packed off interval of the injection boreholes. The temperature sensors were introduced into small diameter observation boreholes (at radial distances of 5.2, 7.2 and 15.7 cm from the wall of the injection borehole), which were filled with an epoxy resin after instrumentation.

The first *in situ* heating tests (performed in step 3 and 4 in Fig. 2.3.2) showed that, with the heating element set at a constant temperature of 80 °C, maximum rock temperature in the three observation boreholes varied from 32.7 °C at 5.2 cm to 23.3 °C at 15.7 cm from the injection borehole. These temperatures were reached after 72 h and were not exceeded even after 12 days when the experiment was stopped. These results were in good agreement with the model calculations, taking into account the presence of the resin between the heating element and the borehole wall. The comparison between the calculated and the measured matrix temperature is shown in Fig. 2.4.1. The lower temperatures obtained by the calculations of about 3 °C may be a consequence of an underestimation of the values for specific heat capacity of the resin which was not precisely known. Nevertheless, the calculated temperature curve represents the shape of the actual temperature curve quite well. Calculations and the field experiments showed that the necessary polymerisation temperature of 40 °C around the injection borehole could not be reached with the selected layout. It was therefore decided to optimise heat conduction into the rock matrix by replacing the resin left over in the borehole after injection with heating oil. The temperature of the heating element was set to 180 °C in order to attain a temperature of at least 40 °C in the adjacent rock matrix aiding complete polymerisation of the resin. The related temperature curves of the heating elements and the temperature sensors are shown in Fig. 3.3.1.

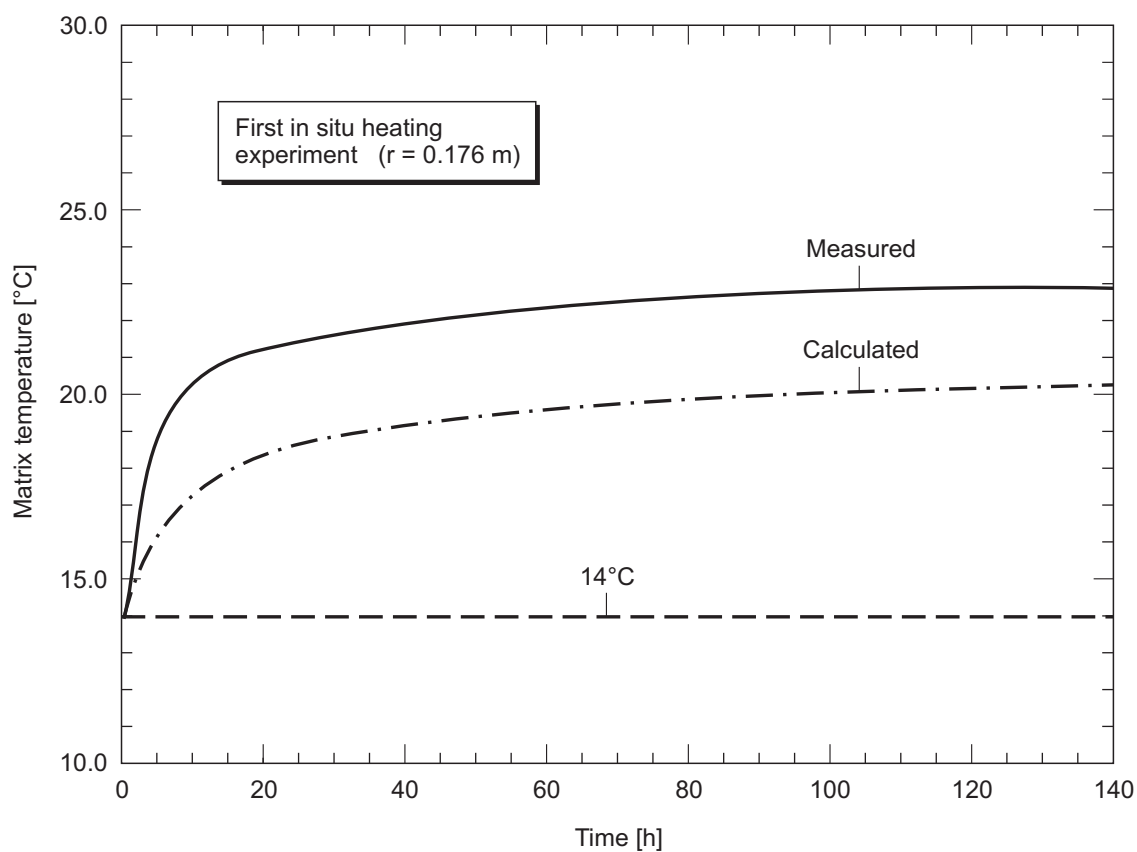


Fig. 2.4.1: Comparison of calculated and measured matrix temperature

The heating oil used was a standard product from Shell Asea called Parapharm 68 and is normally used for greasing fine mechanical tools. The properties of the oil are shown in Tab. 2.4.1. The heating oil was emplaced in the injection boreholes after removing the injection packer system and before replacing them with the heating packers.

Tab. 2.4.1: Properties of heating oil Parapharm 68

Property	Unit	Value / Description
Colour	[-]	white
Density at 20 °C	[kg m <sup>-3</sup> ]	870
Flashpoint	[°C]	215
Pourpoint	[°C]	-12
Kinematic viscosity at 40 °C at 100 °C	[mm <sup>2</sup> s <sup>-1</sup> ]	68 7.8
Toxicity class	[-]	none

## 2.5 Conclusions

The acrylic resin NHC-9 with the eosine dye proved to be the most appropriate resin for the final *in situ* impregnation experiment, providing complete impregnation (no shrinkage of the resin was observed in the investigated rock samples; see also comments in Chapter 8) and good visualisation of the pore space. It exhibited a minimum *in situ* potlife of 40 days at ambient temperature in the 14 °C tunnel as well as in the equipment and in contact with the Grimsel granodiorite. The relevant physical properties of resin NHC-9 are summarised in Tab. 2.5.1. In order to avoid early polymerisation, direct contact of the resin with metallic parts in the injection equipment was avoided and compressed air was used as the pressurising medium. To attain the required heat flux from the heating element into the surrounding rock mass, the borehole was filled with heating oil and the output temperature of the heating element was set at 180 °C to reach the polymerisation temperature of at least 40 °C in the rock matrix around the borehole.

Tab. 2.5.1: Properties of NHC-9 acrylic resin

Properties	NHC-9 acrylic resin
Material basis	Single component acrylate + dye (eosine) + heat initiator
Polymerisation start	by heat (> 40 °C)
Density (20 °C) [kg m <sup>-3</sup> ]	1070
Viscosity [mPa s]	5 °C: ≈ 30; 20 °C: < 10
Tensile strength [MPa]	6
Compressive strength [MPa]	16
Gel time	6 months (room temperature); 36 h (50 °C); 6 h (70 °C)
Boiling point [°C]	> 100
Melting point [°C]	< -10
Storage stability	6 months



### 3 *IN SITU* PORE SPACE IMPREGNATION EXPERIMENT

*A. Möri, M. Adler and C. Bühler*

#### 3.1 Site description and geological overview

The final *in situ* impregnation experiment was performed in the rear chamber of the ventilation drift (VE) at the GTS (Fig. 3.1.1). Six boreholes were drilled into the eastern tunnel wall between tunnel metre 488.85 and 490.92. A shear zone intersects the ventilation drift at tunnel metre 494 with an orientation of 144 / 80 (dip direction / dip angle). The same shear zone can be traced into the AU gallery, where it is called 'AU126'.

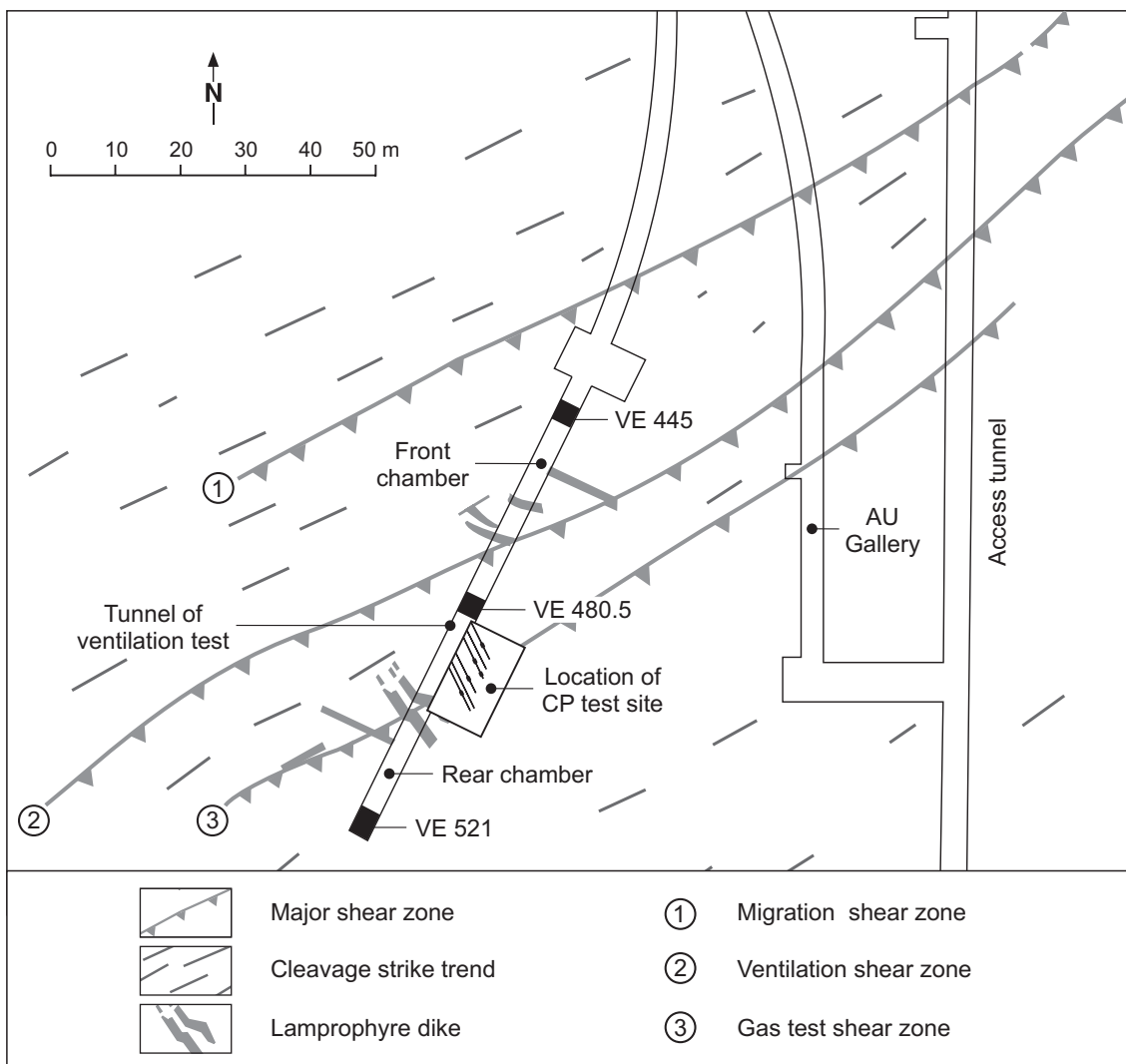


Fig. 3.1.1: Overview of ventilation drift at GTS

The granodiorite rocks at GTS show varying degrees of deformation (detailed petrographic description is given in Chap. 4.1). Ductile deformation of the granodiorite during Alpine greenschist facies metamorphism produced weak cleavage and discrete shear zones. The shear zone in the ventilation drift is characterised by drastic grain size reduction and growth of greenschist facies mineral assemblage consisting of muscovite, chlorite and epidote. It contains a fine-grained mylonitic zone in its centre, which underwent brittle reactivation.

A lamprophyre dike intersects the ventilation tunnel at the same position as the shear zone. It has an orientation almost perpendicular to the shear zone and has no influence on the experiment.

### 3.2 Experimental layout

Four parallel injection boreholes were drilled almost perpendicular to the shear zone and two parallel temperature observation boreholes were drilled between the injection holes. Intervals within the injection boreholes were isolated with mechanical packer systems in a way that no interval intersects the shear zone, that the intervals are at least one metre beyond the tunnel wall (avoid effects of excavation disturbed zone EDZ of the tunnel and desaturation of the matrix) and, finally, that there is a continuous profile through matrix rock on both sides of the shear zone. The positions of the boreholes and the packed-off intervals are illustrated in Fig. 3.2.1. The boreholes were drilled with a HILTI drilling machine using water-cooled single core barrels. The technical data for all boreholes are given in Tab. 3.2.1.

Tab. 3.2.1: Technical data for the boreholes drilled for the final *in situ* experiment; all boreholes have an orientation subparallel to 144 / 07

Borehole (BOVE)	Tunnel metre	Diameter	Length [m]	Purpose	Packed-off interval [cm]	Length or packed-off interval [cm]
97.004	490.92	40 mm	2.48	Injection	170 – 248	78
97.005	490.25	40 mm	2.21	Injection	160 – 221	61
97.006	489.54	40 mm	2.12	Injection	128 – 188	60
97.007	488.85	40 mm	1.82	Injection	120 – 182	62
97.008	490.65	16 mm	2.65	Temperature observation	none	-
97.009	489.22	16 mm	2.05	Temperature observation	none	-
97.010 <sup>9</sup>	~ 490.00	200	1.50	Drillcore for laboratory experiments	none	-

<sup>9</sup> not shown in Fig. 3.2.1.

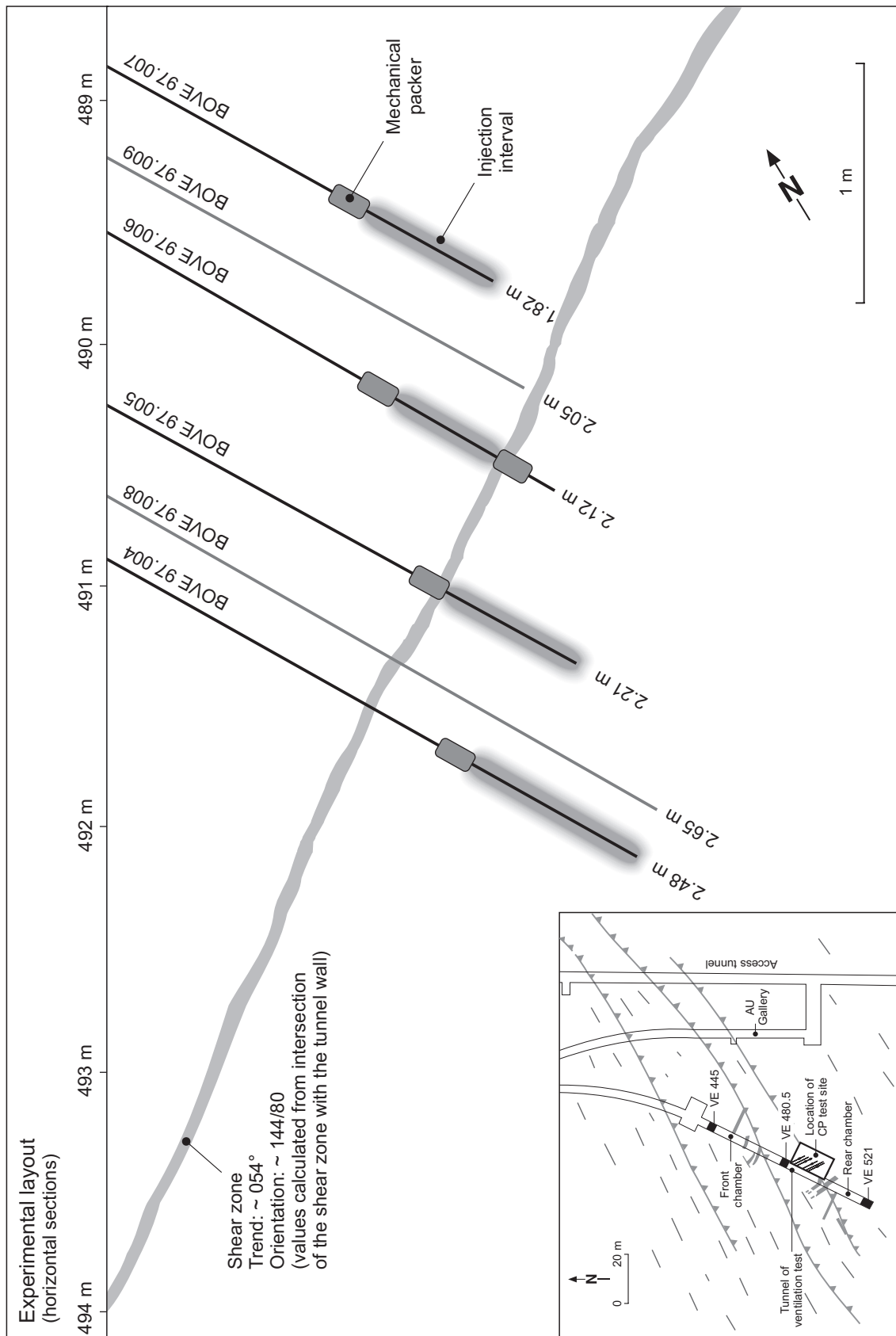


Fig. 3.2.1: Layout of the final *in situ* experiment in the ventilation drift

### 3.3 Injection of resin and heating

The three boreholes 97.004, 97.005 and 97.007 were equipped with mechanical single packer systems and borehole 97.006 with a double packer system, each equipped with lines for resin injection. Each packer system was connected to a pressure vessel containing the resin and each vessel was placed on a digital balance connected to a data acquisition system to monitor resin flow during injection. The resin was injected into the four boreholes using compressed air as the pressurising medium and applying a constant pressure of 10 bars.

The injection period ended after 6 weeks and at that time the resin in the tubing and the borehole was still liquid. The total mass of resin injected into each borehole is listed in Tab. 3.3.1 and the injection curves are shown in Fig. 3.3.1.

The total mass injected into borehole 97.004 is much higher than that for the other boreholes. This is because large amounts of resin were lost at the beginning of the injection phase due to the presence of a couple of open fractures in the bottom part of the injection interval. In order to stop this resin loss and to force the resin to penetrate the matrix, it was decided to pack off this part of the injection interval with an additional packer which reduced the length of the interval to 58 cm. After that, the injection rates for 97.004 were in the same range as in the other boreholes.

A rough estimation of impregnation depth revealed a value of about 8 cm, assuming 1 vol% of matrix porosity around the injection interval.

Tab. 3.3.1: Total mass of resin injected after 6 weeks

Borehole	Injected mass [g]	Injected mass / interval length [g cm <sup>-1</sup> ]
97.004	692	8.9
97.005	194	3.2
97.006	162	2.7
97.007	83	1.3

After termination of the injection phase, the remaining resin in each borehole was replaced by heating oil and the heating element was inserted. The heating oil was added to enhance heat conduction between the heating element and the borehole wall. During the heating phase, the heating element temperature in the boreholes was set to 180 °C. Temperatures between 40 and 60 °C were attained, as monitored in observation boreholes in the rock matrix at a distance of 25 cm from the heating borehole (this distance was chosen in order to minimise rock damage to the rock matrix in the vicinity of the injection borehole). The heating phase was terminated after 37 days (see Fig. 3.3.1).



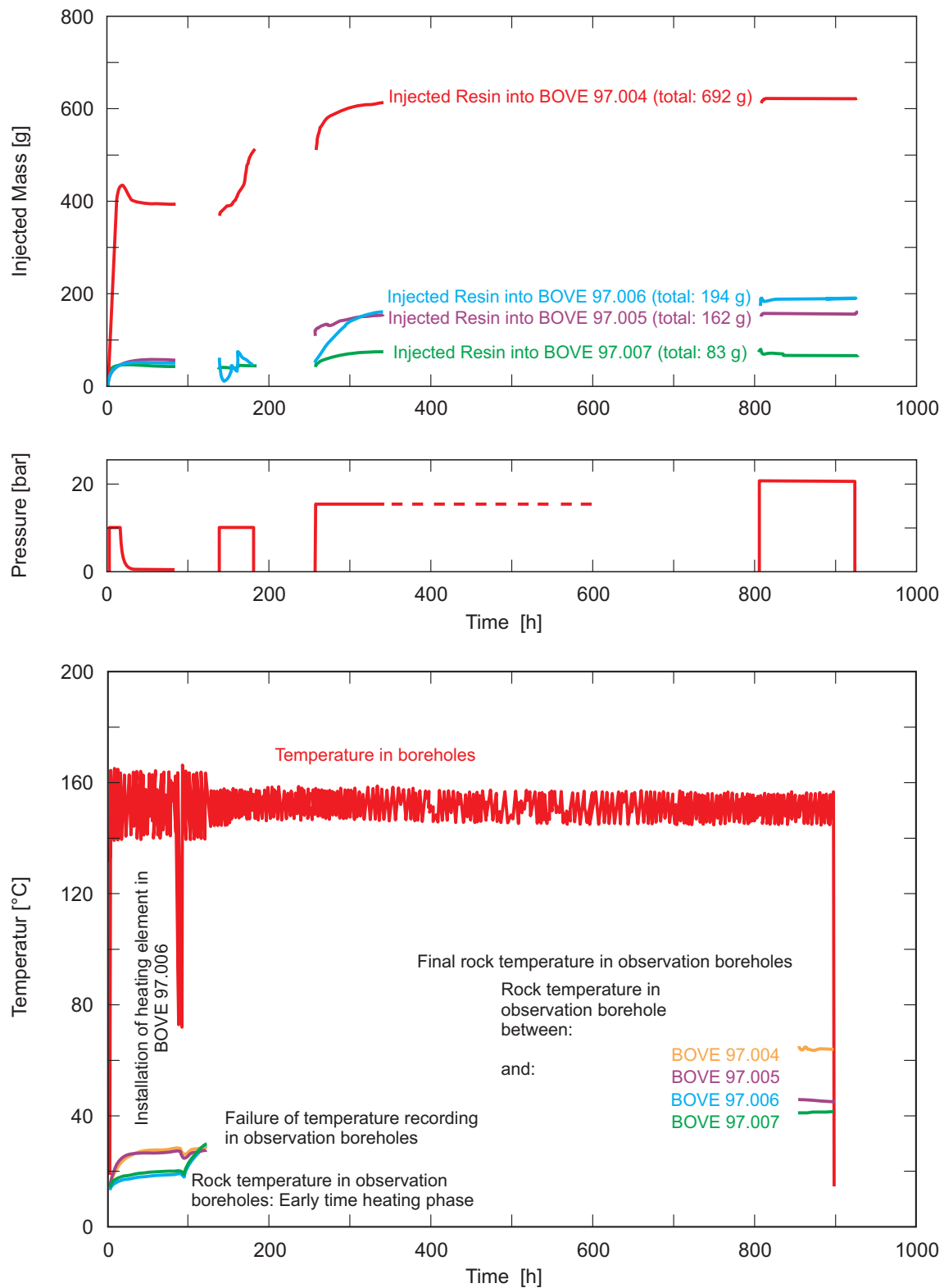


Fig. 3.3.1: Injection pressure and mass of injected resin (top); heating curves of temperature sensors in observation boreholes and of the heating element (below)

### 3.4 Overcoring and sub-sampling

The four injection boreholes were overcored with a 200 mm single core barrel. The impregnated parts in overcores BOVE 97.004, 97.005, 97.006 and 97.007 were sawn into slabs normal to the axis of the injection borehole and were used for macroscopic analyses. Some of these slabs were sub-sampled for preparation of thin sections<sup>10</sup>. The relative orientations of overcore, slabs and thin sections with regard to the three principal planes (x'y'-, x'z'- and y'z'- plane) are shown in Fig. 3.4.1. Tab. 3.4.1 provides the dimensions of the four overcores as well as the exact position of sawed slab surfaces.

Tab. 3.4.1: Dimensions of overcores BOVE 97.004 to 007 with the positions of the slab surfaces

Borehole	Diameter [mm]	Length [m]	Packed -off interval during injection [m]	Position of slab surfaces [m]*	Distance from the shear zone [cm]*
BOVE 97.004	200	2.75	1.70 – 2.48	<b>1.63</b>	<b>36</b>
				1.80	50
				2.00	72
				2.13	86
				<b>2.45</b>	<b>116</b>
BOVE 97.005	200	2.40	1.60 – 2.21	<b>1.58</b>	<b>2</b>
				1.65	10
				1.80	24
				2.20	64
BOVE 97.006	200	1.98	1.28 – 1.88	1.28	58
				1.60	26
				1.75	12
				1.88	2
BOVE 97.007	200	1.94	1.20 – 1.82	1.20	98
				1.40	76
				<b>1.60</b>	<b>56</b>
				1.80	48

\* Bold numbers indicate slab surfaces which were broken during drilling and normal style numbers indicate sawn slab surfaces.

<sup>10</sup> Note that sub-sampling for microspopic, geophysical and porosimetry investigations were taken outwith the range of influence of the borehole disturbed zone (BDZ) which was observed around the injection boreholes and outwith the contact surface of the heating oil to the matrix (see details below).

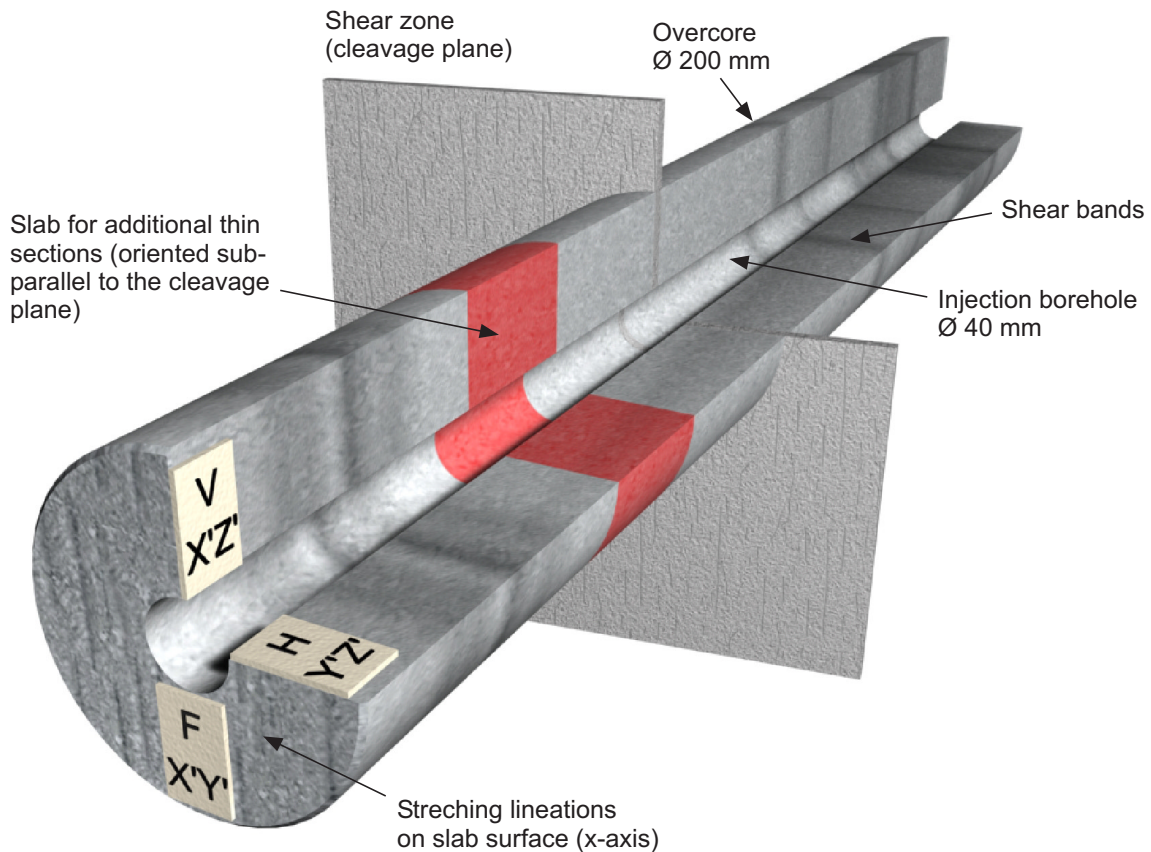


Fig. 3.4.1: Intersections of the boreholes with the shear zone T

The borehole is oriented almost normal to the shear zone. The thin sections (V = vertical, H = horizontal, F = flat) have an orientation sub-parallel to the three principal planes  $x'y'$ ,  $x'z'$  and  $y'z'$ .

### 3.5 Summary

The experimental layout covered about 2.40 m of rock matrix distributed on both sides of the shear zone. This revealed a continuous profile of *in situ* impregnated Grimsel granodiorite matrix. Resin injection was stopped after 6 weeks and the resin within the equipment and in the injection interval still remained liquid. A rough estimation of impregnation depth (based on an assumed matrix porosity of 1 %) revealed a value of about 8 cm around the injection borehole which would be completely covered by the overcoring. The achieved rock temperature in the observation boreholes varied between 40 and 60 °C at a distance of 25 cm to the injection boreholes. This temperature guaranteed good polymerisation of the resin and overcoring was successfully performed.



## 4 PETROGRAPHY OF GRIMSEL GRANODIORITE AND DEFINITION OF STRUCTURAL ELEMENTS AND PORE TYPES

*A. Möri, M. Adler, M. Mazurek, M. Schild and K. Ota*

In the previous chapter, the development of a suitable resin formulation and a methodology for impregnation and immobilisation of matrix rock was described. The *in situ* matrix impregnation was successfully carried out and provided matrix samples that enabled the investigation of the *in situ* pore structure of granodiorite matrix.

The main focus of analytical work was the investigation of the form, distribution and connectivity of the porosity in the undisturbed rock matrix and comparison of these features with those from "disturbed" rock samples. The investigations were carried out at different scales (macroscopic, microscopic, nanometre scale). Standard thin section petrography under normal and UV light, cathodo-luminescence microscopy and SEM (Scanning Electron Microscope) were all used to characterise samples. Frequency counting methods, orientation measurements on microstructures and determination of seismic velocities in the rock matrix were aimed at investigating the spatial distribution of pore space and are reported in Chapters 5 and 7.

### 4.1 Petrography of Grimsel granodiorite matrix

The Grimsel Test Site (GTS) is situated in the Aare Massif, a basement high in the Helvetic realm of the Alps. The Aare Massif consists of a metasedimentary envelope that was intruded by Hercynian granitoids (320 – 280 Ma) such as the Central Aare granite and the Grimsel granodiorite (the host rocks of the GTS). All rocks of the Aare Massif have been affected by Alpine greenschist metamorphism and deformation at about 25 Ma BP and the plutonic rocks were metamorphosed to gneisses. Structures in the Hercynian plutonic rocks are mostly attributed to Alpine deformation (STECK 1968, MARQUER & GAPAIS 1985).

Peak Alpine metamorphic conditions in the vicinity of the GTS are estimated at 400 °C and 2.5 to 3 kbar (CHOUKROUNE & GAPAIS 1983, MARQUER et al. 1985). The following structural features can be assigned to this greenschist facies metamorphism and associated ductile deformation: cleavage, mylonitisation (including formation of quartz ribbons), mineral stretching lineation, extension fractures and quartz recrystallisation.

The formation of brittle structures, which are common in the crystalline rocks at Grimsel, post-dates the ductile deformation and can be attributed to the post-metamorphic regional uplift that still operates to the present day (current uplift of 1 – 2 mm/a). In most cases, faults run along pre-existing mylonitic zones and are parallel to metamorphic cleavage. Brittle structural features include both cataclastic fault breccias and discrete faults and deformation occurred at significantly lower temperatures and pressures compared with the preceding ductile deformation (see also BOSSART & MAZUREK 1991 for details).

All samples that were investigated show a rather uniform mineralogical composition of K-feldspar (12 – 24 vol%), plagioclase (29 – 33 vol%), quartz (27 – 28 vol%) and biotite (7 – 11 vol%), with accessory muscovite/sericite, apatite, sphene, epidote, zircon, chlorite, calcite and ore minerals.

In the weakly to undeformed matrix of Grimsel granodiorite, medium-grained quartz shows undulatory extinction as well as sub-grain formation. Highly deformed rock portions comprise recrystallised, mosaic textured quartz which forms elongated quartz ribbons parallel to the cleavage. In shear bands, quartz is extremely fine-grained and shows lobate to round grain boundaries indicating dynamic recrystallisation.

Plagioclase occurs as coarse grains with polysynthetic twinning in undeformed rock portions and most grains are intensely altered to sericite and epidote. Growth zonation of the plagioclase (albite growth seams) and alteration of the feldspars was detected by cathodo-luminescence. The different cathodo-luminescence colours of the feldspars can be explained by chemical alterations: with progressing deformation, the Na<sub>2</sub>O, CaO and MgO concentrations increase, while the K<sub>2</sub>O concentrations decrease (KEUSEN et al. 1989). Unlike quartz, plagioclase underwent cataclastic deformation indicated either by brittle cracks or by fragmentation of plagioclase grains in shear bands. K-feldspar appears as porphyroblasts with grain sizes of up to a few cm in weakly deformed rock matrix. The porphyroblasts exhibit perthitic exsolution lamellae as well as carlsbad and microcline twinning. Angular to roundish K-feldspar clasts in shear bands indicate cataclastic deformation of K-feldspar. A weak stretching lineation of K-feldspar grains occurs in the cleavage plane. Primary magmatic biotite appears as single sheets in undeformed rock portions and the sheets show ilmenite exsolution phenomena and weak chloritisation. Biotite in shear bands forms aggregates with chlorite and muscovite. In undeformed rock matrix, fine-grained muscovite occurs as sericite in altered plagioclase. In shear bands, muscovite is a major component forming aggregates with biotite and chlorite. Readily oriented and syntaxially grown muscovite also forms narrow mica bands that outline grain boundaries of K-feldspar, plagioclase and quartz. Epidote either occurs as an alteration product in plagioclase grains or as a major component in shear bands, where it often forms large aggregates.

## 4.2 Structural elements

As pointed out earlier, the CP experiment focuses on the *in situ* porosity of the matrix of the Grimsel granodiorite in the vicinity of a water-conducting shear zone. A weak foliation is developed in all matrix samples that were excavated for the CP experiment, and it is defined by compositional banding of alternating dark biotite layers and bright, quartz-rich layers. The extent of this weak cleavage varies in cm scale between undeformed to weakly and, near the shear zone, to highly deformed rock portions. The degree of metamorphism of the rock matrix is asymmetrical about the shear zone. On the northern side, there is little deformation outside a narrow intensely deformed zone of several cm width immediately in the vicinity of the shear zone. On the southern side, the degree of deformation is less intense but can be traced up to several metres from the shear zone.

The textures found in the drillcores from Grimsel granodiorite matrix have been subdivided into the following structural elements:

- *Weakly to undeformed rock matrix* shows granoblastic textures with medium- to coarse-grained plagioclase, K-feldspar and quartz. Faint cleavage is displayed by scattered alignment of biotite.
- *Shear bands* are 0.5 to 10 mm in width and define the main cleavage. They are characterised by an extreme reduction in grain sizes and dynamic recrystallisation. Major components in shear bands include aggregates of muscovite, biotite and chlorite, aggregates of extremely fine-grained quartz, feldspar clasts and coarse idiomorphic epidote and sphene. Fragments of plagioclase and K-feldspar often show asymmetric pressure shadows.
- *Quartz ribbons* consist of recrystallised, mosaic textured quartz and single grains of muscovite. They are stretched out parallel to the cleavage. No preferred orientation of the crystallographic c-axes of quartz in the ribbons was found. Quartz ribbons often extend into shear bands.

- *Mica bands* (width < 4 mm) consist of syntaxially grown and randomly oriented muscovite, epidote and mosaic textured quartz. They often branch off from shear bands and follow grain boundaries of feldspars and quartz in the coarse-grained matrix.
- *Microfractures* predominantly occur in large feldspar grains but also crosscutting other minerals and aggregates of minerals within the rock matrix.

### 4.3 Pore types

Numerous pore types have been distinguished by microscopic analyses of UV illuminated thin sections. Some of the pore types were already described by BOSSART & MAZUREK (1991) who investigated water flow paths in a GTS shear zone. As the present report deals with the matrix of Grimsel granodiorite, additional pore types have been introduced. A summary of the characteristics of each pore type is given in Tab. 4.3.1. An important point is that most apertures of pores in the matrix were found to be below the detection limit of optical microscopy. Overshining effects of the fluorescence under UV light at high magnifications as well as oblique intersection of the section surface with the pore may also lead to an overestimation of the aperture. Using confocal scanning laser microscopy would avoid these overshining effects but it was decided not to use this technique due to the very small viewing area covered by this technique (for details see MONTOTO et al. 1995). Additional aperture measurements were performed on SEM (scanning electron microscopy) and backscattered electron (BSE) images (see Chapter 6).

Tab. 4.3.1: Summary of pore type characteristics

Pore type	Shape on thin section	Range of apertures <sup>11</sup> [µm]	Occurrence
Grain boundary pores	fine channels	< 5 – 20	<ul style="list-style-type: none"> <li>- in weakly deformed matrix along feldspar and quartz grains</li> <li>- shear bands</li> <li>- quartz ribbons</li> <li>- mica bands</li> </ul>
Sheet silicate pores	very fine, parallel cleavage	0.1 – 10	<ul style="list-style-type: none"> <li>- shear bands</li> <li>- mica bands</li> </ul>
Solution pores	cloudy spots	< 5	<ul style="list-style-type: none"> <li>- altered plagioclase</li> <li>- along perthitic exsolution lamellae in K-feldspar</li> </ul>
Microfractures	channels	< 5 – 10	<ul style="list-style-type: none"> <li>- not bound to any mineralogical, textural or deformational feature</li> <li>- cracks parallel to drilling axis only adjacent to borehole</li> </ul>

<sup>11</sup> Most pore apertures in the matrix were found to be below detection limit of optical microscopy. Overshining effects of the fluorescence under UV light at high magnifications as well as oblique intersection of the section surface with the pore may also lead to an overestimation of the aperture.

The different pore types can be described as follows:

- *Grain boundary pores* (Fig. 4.3.1a) are the most abundant pore type. In weakly deformed matrix, they form channels along feldspar and quartz grains and show a random orientation. Their aperture ranges between  $< 5$  to  $20\ \mu\text{m}$ . Dense networks of grain boundary pores occur in quartz ribbons. Grains of feldspars, epidote and sphene embedded in shear and mica bands are usually bordered by grain boundary pores as well.
- *Sheet silicate pores* (Fig. 4.3.1b) are present in shear bands and to a lesser extent in mica bands. In shear bands, very thin parallel channels cross the cleavage of muscovite, biotite and chlorite. Syntaxially grown muscovite in mica bands, on the other hand, contains very few sheet silicate pores. Sheet silicate pores generally have apertures of less than  $5\ \mu\text{m}$ . Due to their restricted occurrence in shear bands, they usually have a preferred orientation parallel to the cleavage. The speckled (or stain-like) appearance of the sheet silicate pores, with dimensions of up to several tens of  $\mu\text{m}$ , was commonly observed in mica bands and along intense alteration (i.e. sericitisation) of plagioclase, which shows indistinct outlines. Cleavage of biotite in sheet silicate pores is distinct and displays a planar, elongated geometry with apertures of  $100\ \text{nm}$  to  $10\ \mu\text{m}$ .
- *Solution pores* (Fig. 4.3.1c,d) are associated with alteration and exsolution phenomena mainly in feldspars, but also in epidote and micas. Diffuse, cloudy solution pores occur in sericitised parts of plagioclase. Cloudy solution pores in K-feldspar run parallel to the perthitic exsolution lamellae and microcline twinning. The size of solution pores is usually smaller than  $5\ \mu\text{m}$ . SEM investigations revealed apertures of up to several tens of  $\mu\text{m}$ , mostly associated with exsolution lamellae within K-feldspar porphyroblasts.
- *Microfractures* (Fig. 4.3.1e) are represented by long channels with comparatively large apertures of up to  $10\ \mu\text{m}$ . Microfractures running parallel to the borehole axis are restricted to a  $3\ \text{cm}$  wide zone adjacent to the borehole and are interpreted as an artefact of the stress redistribution around the injection boreholes (stress relief). Most of the randomly oriented microfractures are found in large feldspar grains and reflect brittle behaviour of these grains during deformation. Microfractures are the only pore type that is not bound to any textural or structural feature of the rock. A detailed analysis of microfractures fabrics is given in Chapters 6 and 7.



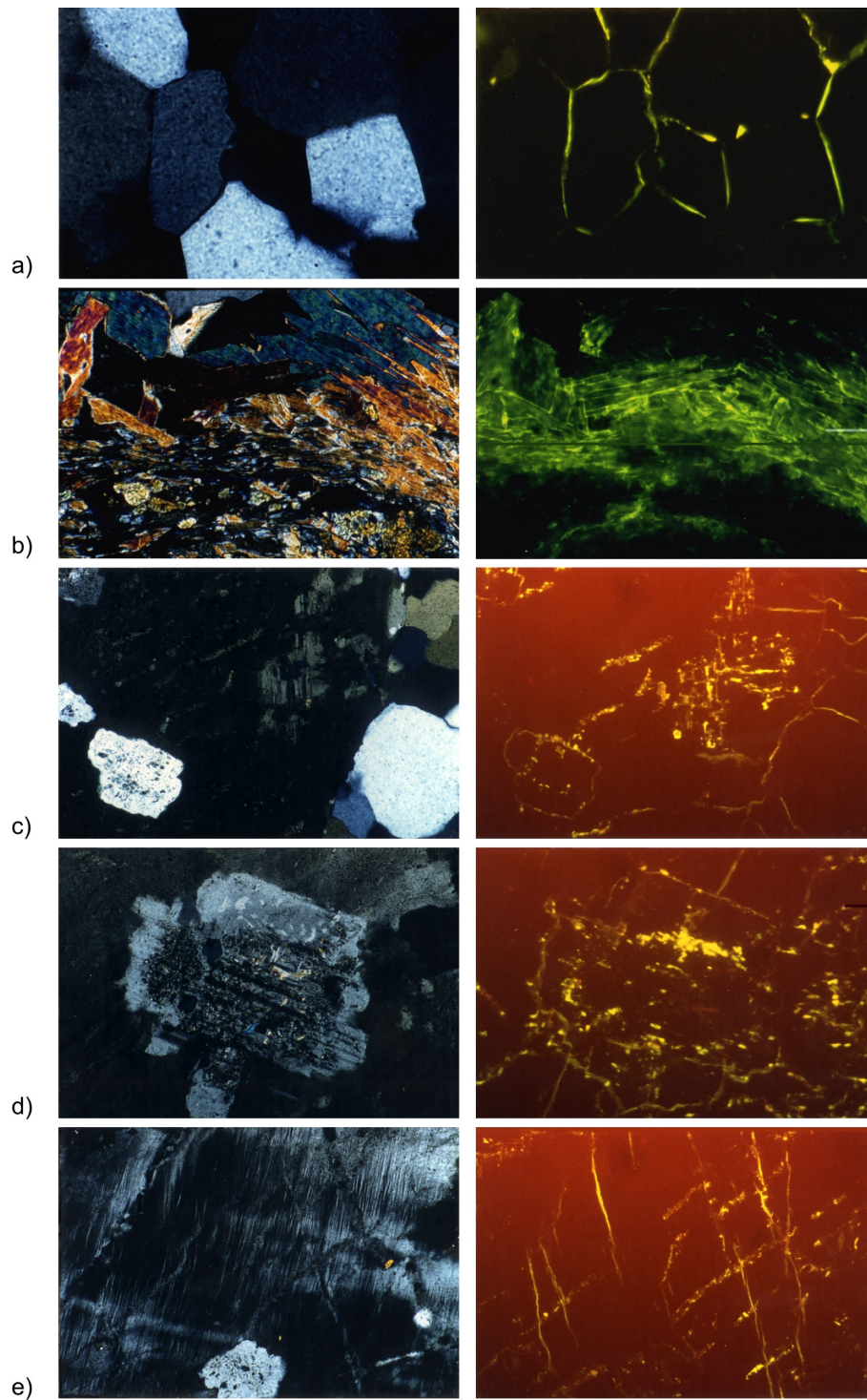


Fig. 4.3.1: Thin section photomicrographs of pore types under crossed nicols (left) and under UV light (right)

a) Grain boundary pores around mosaic textured quartz in quartz ribbons (width of image is 5 mm), b) Sheet silicate pores in shear band (width of image is 10 mm), c) Cloudy solution pores in K-feldspar grain with perthitic exsolution lamellae and microcline twinning (width of image is 10 mm), d) Solution pores in sericitised parts in plagioclase (width of image is 10 mm), e) Microfractures in large K-feldspar grain with perthitic exsolution lamellae (width of image is 10 mm).

#### 4.4 Summary

Weakly to undeformed rock matrix displays granoblastic textures with medium- to coarse-grained plagioclase, K-feldspar and quartz. Here, zones of enhanced porosity occur along grain boundaries (grain boundary pores) and, along with exsolution and twinning phenomena, in large feldspar grains (solution pores). In zones of enhanced ductile deformation, the amount of large feldspar grains is smaller due to grain size reduction, and the abundance of solution porosity therefore decreases. Sheet silicate porosity in weakly to undeformed matrix is bound to mica bands. High sheet silicate porosity is found in shear bands, i.e. in zones of ductile deformation. Quartz ribbons usually contain a dense network of grain boundary pores, and occur in shear bands as well as weakly deformed rock matrix. Microfractures were mainly found in weakly to undeformed matrix and in feldspar grains. Fig. 4.4.1 illustrates the distribution of the different pore types at their typical position in the matrix rock.

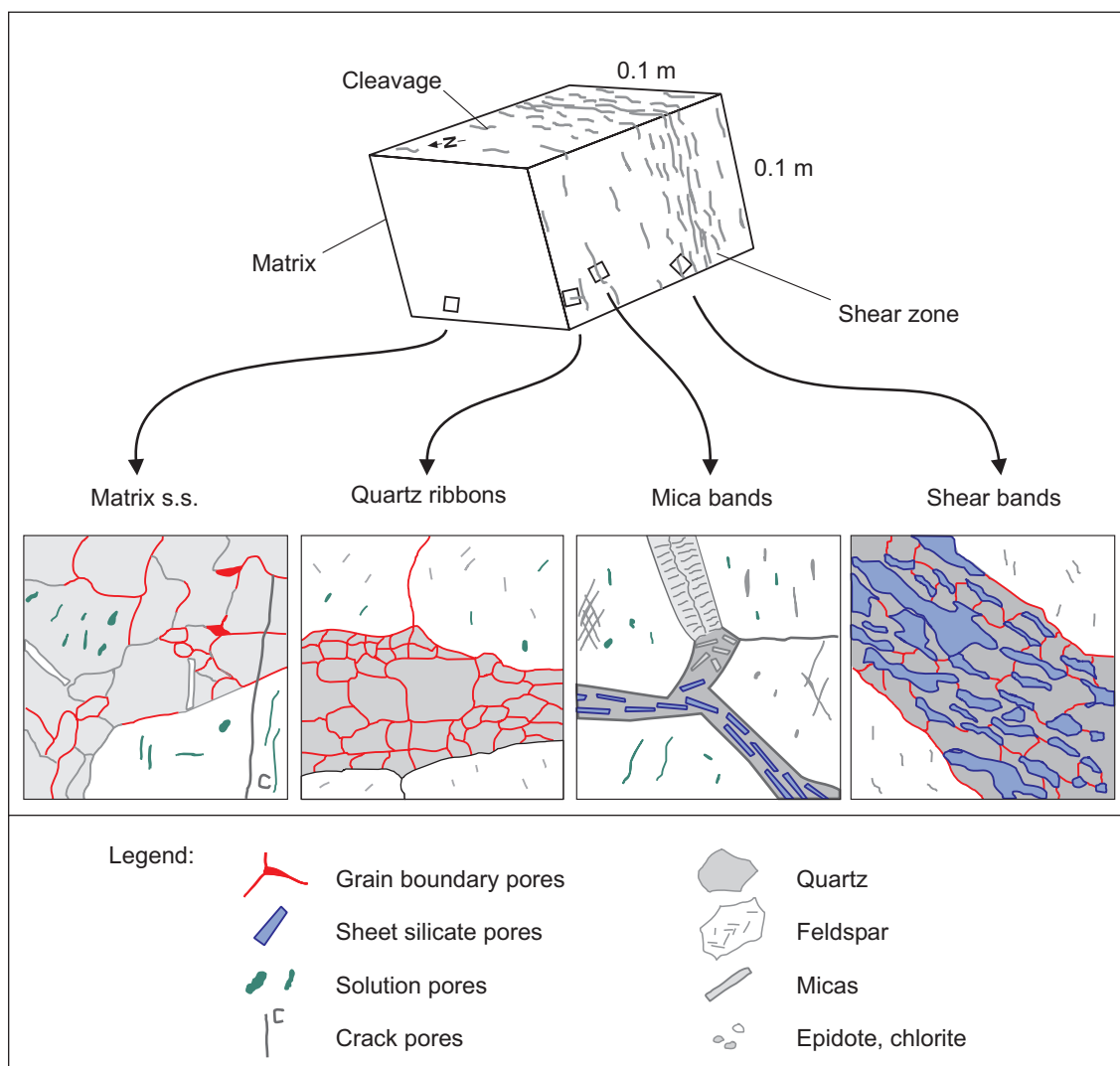


Fig. 4.4.1: Pore type distribution in granodiorite matrix

## **5 PORE SPACE DESCRIPTION UNDER UV LIGHT AT DIFFERENT SCALES AND FREQUENCY COUNTING METHODS**

*M. Adler and A. Möri*

### **5.1 Methods**

The aim of this investigation was to characterise the appearance and distribution of pore space in the rock matrix macroscopically as well as microscopically. Special emphasis was placed on the question of whether the appearance and distribution of pore space in the rock matrix depends on its relative position to the main shear zone.

The impregnated (packed off) intervals of overcores BOVE 97.004, 97.005, 97.006 and 97.007 covered both sides of the shear zone. The impregnated core sections were sawn into slabs of 15 – 40 cm length normal to the injection borehole. Fig. 5.1.1 displays the results of the drillcore mapping on the overcores and the corresponding position of the slab surfaces. The surfaces of the slabs were photographed under UV light in order to more easily visualise the volume of resin-filled pore space around the injection borehole. Macroscopic observations of impregnated pore structures were compared with structural core logs.

The microscopic distribution of pore space was investigated in 16 thin sections from overcore BOVE 97.006 which covers the matrix adjacent to one side of the shear zone. Three different sets of thin sections were produced for each position relative to the core axis (see Fig. 3.4.1): one in the y'z' plane (H-sections), one in the x'z' plane (V-sections), and one in the x'y' plane (F-sections). This arrangement enabled the investigation of the pore space distribution normal to the injection borehole, and as a function of distance from the shear zone. The length of the matrix profiles perpendicular to the injection borehole that were investigated is 8 cm and thus exceeds the macroscopically visible impregnation depth.

Line countings and aperture measurements of pore structures were performed under the UV microscope. In order to minimise the effects of small-scale mineralogical and structural heterogeneities, the intersections of pore structures were counted along two parallel lines within the same thin section.

### **5.2 Results**

#### **5.2.1 Pore space distribution on macroscopic scale**

Photographs of all slab surfaces under UV light are shown in Fig. 5.2.1. The impregnation haloes of the rock matrix around the injection borehole have a roundish or elliptic shape. They are defined by bright yellow spots of impregnated K-feldspar and plagioclase grains, whereas quartz grains within the haloes show on a macroscopic scale only diffuse or no impregnation.

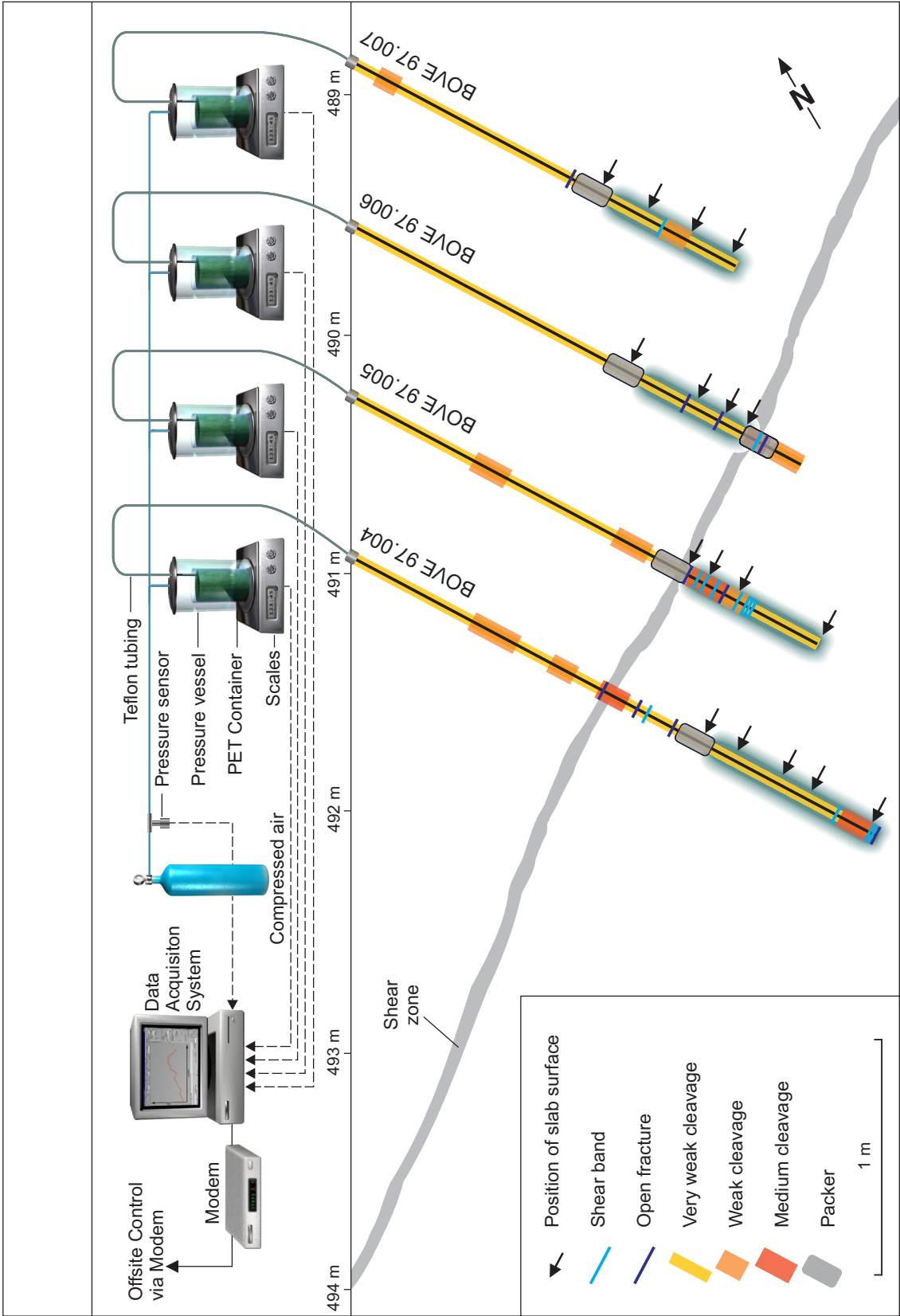


Fig. 5.1.1: Drillcore mapping and position of slab surfaces

Note the asymmetric shape of the ductile deformation on both sides of the shear zone.

The most intensive and extended impregnation occurred in the bottom part of BOVE 97.004 at 2.45 m (Fig. 5.2.1, see also Fig. 5.1.1), where a lot of resin was lost at the beginning of the injection phase (see Chap. 3.3). Structural analysis of the core shows that this section is characterised by a high density of shear bands, which partially underwent brittle reactivation indicated by open fractures and cohesionless rock parts (breccia components, fault gouge was not preserved/present). Brittly reactivated shear bands therefore induce a high transmissivity compared to the surrounding rock matrix.

The horizontal and vertical extent of the impregnation haloes were measured on each of the slab surfaces. On most of the slab surfaces, the longer axis of the fluorescent halo runs parallel to the mineral stretching lineation of the rock, which is defined by elongated feldspar grains, quartz ribbons and aligned sheet silicates.

Surface of impregnated slab:

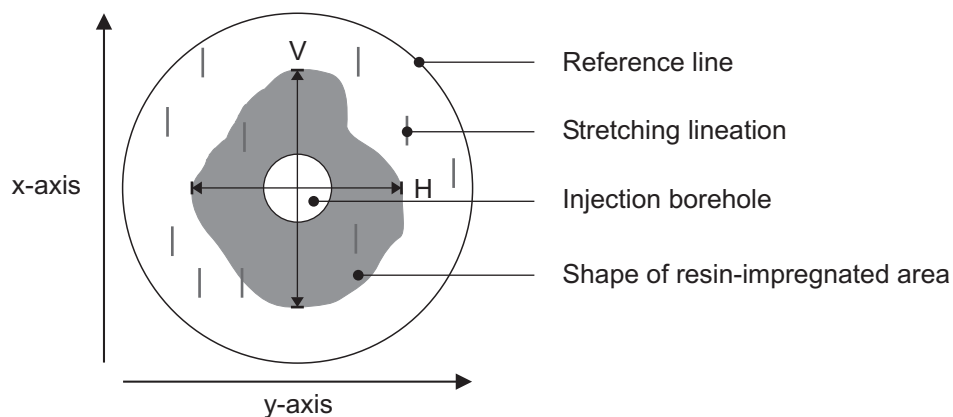


Fig. 5.2.1: General orientation of elliptic resin halo on slab surfaces

This trend is also obvious when plotting absolute x- and y-values of the measurements against each other (Fig. 5.2.2). Surfaces which were broken during overcoring showed the strongest elongation of the ellipse, reflecting the ductile precursor structures (shear bands) and the (weak) brittle reactivation. A systematic change in shape and extent of the impregnated holes with increasing distance to the shear zone could not be observed.

The impregnated section of overcore 97.006 was cut along its axis in order to investigate macroscopically visible rock matrix impregnation as a function of distance to the shear zone. Fig. 5.2.3 shows the core under normal and UV light as well as the positions of the shear zone and thin sections which were used for microscopic analyses. Although the shear zone and the matrix beyond (south part of the shear zone in Fig. 5.2.3) were isolated from the injection borehole by a packer, they have been affected by resin-impregnation and exhibit yellow coloured feldspar grains. However, there is a slight decrease in brightness and penetration depth of resin into the rock matrix with increasing vicinity to the shear zone. The poor impregnation close to the shear zone may be related to the lack of shear bands in the northern part of the matrix close to the shear zone (see Fig. 5.1.1).

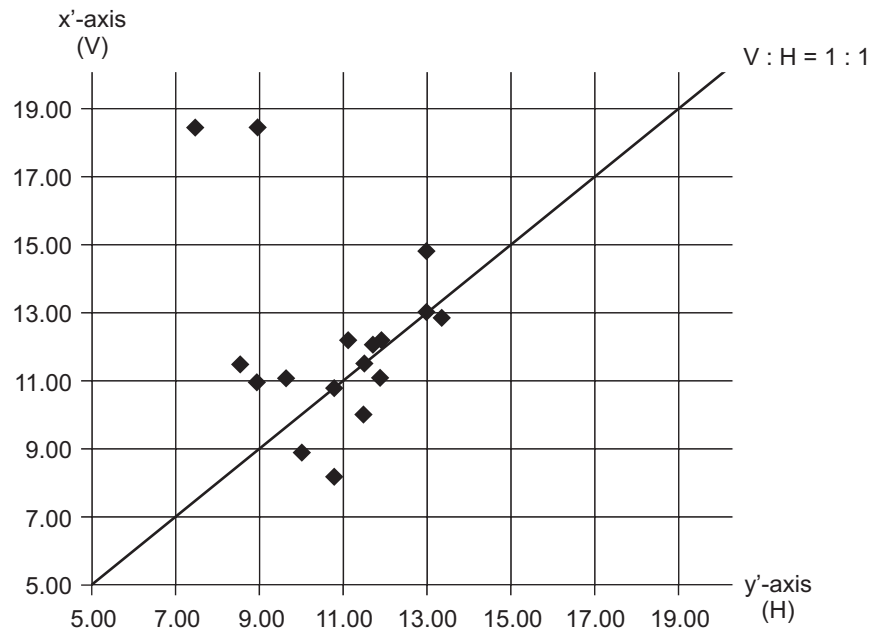


Fig. 5.2.2: x' and y' axis of ellipsoids of macroscopically visible pore space filling [cm]

### 5.2.2 Pore space distribution on microscopic scale

The distribution of each pore type was extensively investigated under the UV microscope at different distances from the shear zone in the y'z'- as well as the x'z'-plane by registering the number of intersections of each pore type with a counting line. The results are illustrated in Fig. 5.2.4 and show that grain-boundary pores are the most abundant pore type in this part of the matrix. Their average frequency per unit distance normal to the injection borehole is 14.8 pores per cm. Solution pores have an average frequency of 4.0, microfractures of 2.6 and sheet silicate pores of 1.2 pores per cm. The results also illustrate that all pore types in the matrix are equally distributed independent of their distance from the shear zone. Although the precise distance of minerals could influence the form of the pore type curves (Fig. 5.2.5), the granodiorite rock matrix generally shows a homogeneous mineral distribution, even at short distances from any shear zone (see BOSSART & MAZUREK 1991) and so this plays no role in these samples.

Looking at the distribution of pores along the individual counting lines in Fig. 5.2.4, i.e. perpendicular to the injection borehole, it can be seen that grain-boundary and microfractures show a more or less abrupt decrease in frequency within 3 to 4 cm from the injection borehole. This was thought to be attributable to the presence of a borehole disturbed zone (BDZ)<sup>12</sup>. Mechanical stress loosens the original grain texture creating grain-boundary pores and even fractures mineral grains producing microfractures. The presence of a BDZ within this zone is further evidenced by the observation of microfractures exhibiting a preferred subparallel orientation to the axis of the injection borehole (see also section 7.2.2 and comments in BLÜMLING 1997, ALEXANDER et al. 2001 and VILKS et al. 2001).

<sup>12</sup> Similar BDZ artefacts have been observed in many rock types from around the world, for example in Finnish cores where discing was related to stress release (K.-H. HELLMUTH, pers. comm. 2001) and in Canadian crystalline rocks (VILKS et al. 2001) related to large horizontal stresses.



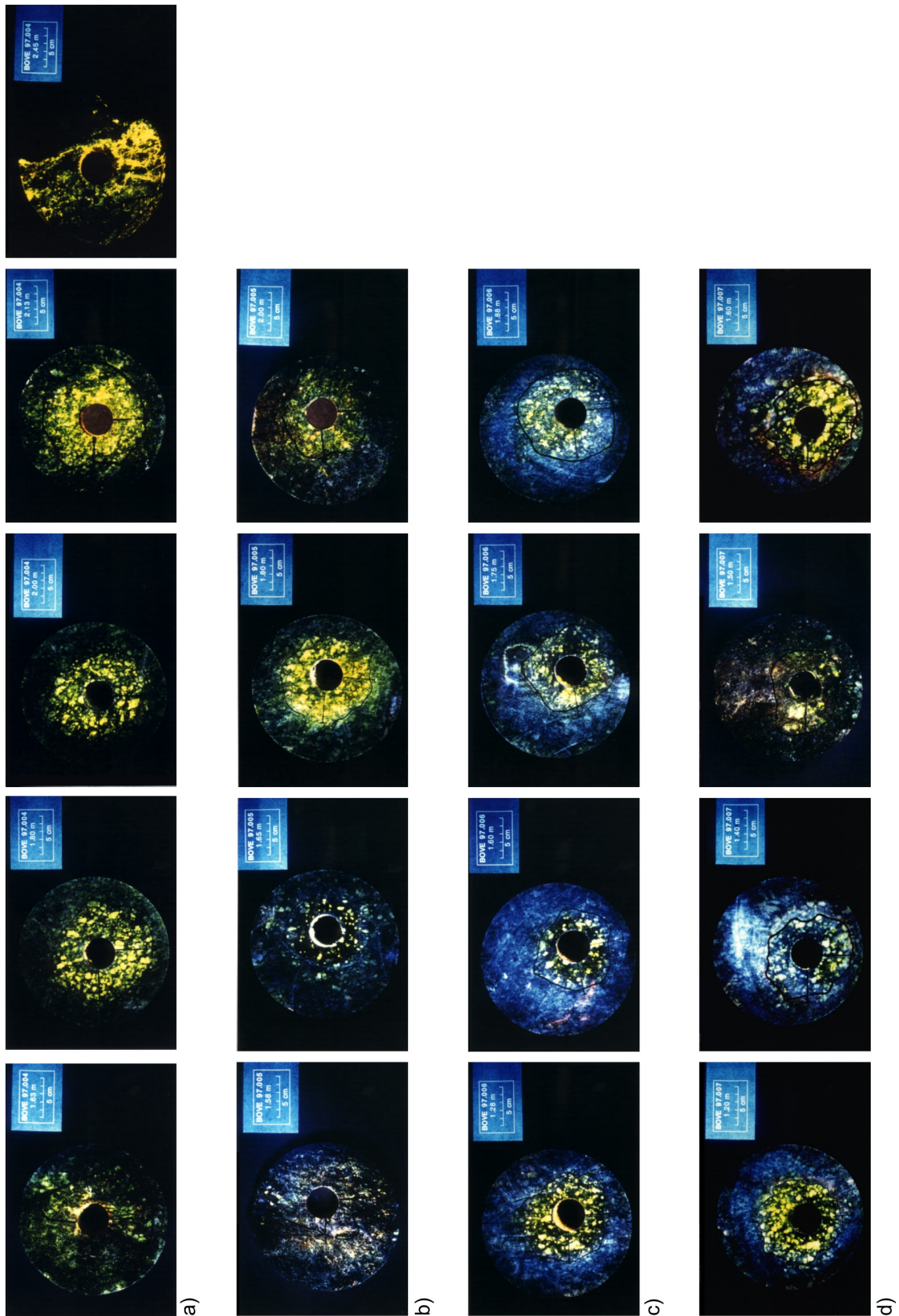


Fig. 5.2.3: Slab surfaces photographed under UV light (position of surface is indicated in photograph): a) BOVE 97.004, b) BOVE 97.005, c) BOVE 97.006, d) BOVE 97.007

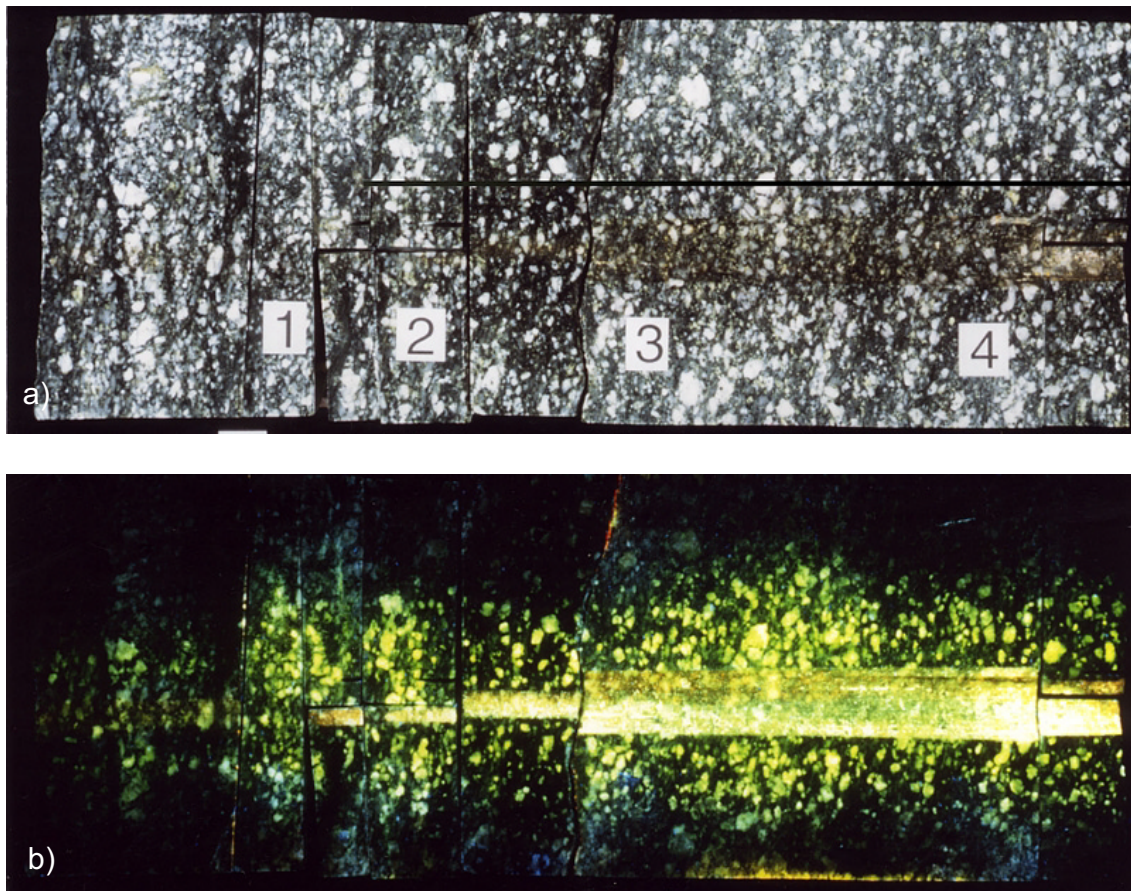


Fig. 5.2.4: a) Cross-section of the impregnated interval of overcore BOVE 97.006 between 1.28 m and 1.88 m, numbers 1 to 4 indicate the position of thin sections used for microscopic analyses; b) Cross-section of the same interval under UV light, the bright central partly reflects the injection borehole

The extent of pore space impregnation in the  $x'z'$ -plane is equal to the one in the  $x'y'$ -plane, both directions showing impregnation depths between 4.7 and 6.1 cm normal to the injection borehole. Grain boundary pores show the deepest penetration into the rock matrix with a mean penetration depth of 5.7 cm. Mean penetration depths of the other pore types are 5.6 cm for solution pores, 5.3 cm for microfractures and 4.7 cm for sheet silicate pores which appears to indicate that highest impregnation depth was found in pore types with highest apertures. However, this observation should be treated with caution due to the fact that some of the pores are below the UV microscopy detection limit and therefore additional investigations with other techniques should be carried out (see comments above).

Grain boundary and microfractures show the widest range of apertures between  $< 5 \mu\text{m}$  up to  $20 \mu\text{m}$  and  $< 5 \mu\text{m}$  up to  $10 \mu\text{m}$ , respectively. The apertures of sheet silicate and solution pores are generally smaller than  $5 \mu\text{m}$  lying below the resolution of the applied optical method. The apertures of any pore type showed no systematic changes with increasing distance from the injection borehole.



### 5.3 Conclusions

The abundance and distribution of pore space strongly depends on the mineralogical and structural composition of the rock. Macroscopic investigations revealed highest porosities in rock portions where ductile deformation underwent brittle reactivation producing open fractures. Such features are rare in the matrix and are more abundant in the vicinity of the shear zone. The ellipsoidal shape of the impregnated hole around the injection borehole shows its larger axis parallel to the stretching lineation direction, which is defined by elongated feldspar grains, quartz ribbons and aligned sheet silicates. The main pore types found in these structures are grain boundary pores and sheet silicate pores.

Microscopic investigations have shown that in weakly to undeformed rock matrix, most of the porosity is made up of grain boundary pores around granoblastic K-feldspar, plagioclase and quartz. Grain boundary pores show highest frequencies as well as widest apertures. Additional pore space is provided by solution pores, microfractures and sheet silicate pores in order of decreasing abundance. All of these pore types are filled with resin and therefore interconnected and permeable for pore waters which migrate through in the Grimsel granodiorite matrix.

An abrupt decrease in the frequency of grain-boundary pores, microfractures and borehole parallel orientated microfractures at a distance of 3 – 4 cm normal to the injection borehole confirms the presence of a borehole disturbed zone (BDZ) surrounding the injection borehole (see the discussion above) and this zone is expected to influence the matrix impregnation. This slight increase in porosity and perhaps also in the aperture of existing pores was not observed in solution and sheet silicate pores. Nevertheless, all pore types were found to be impregnated beyond this zone and are therefore assumed to be inter-connected. Tab. 5.3.1 is a summary of the microscopically quantified parameters (frequencies, apertures, impregnation depths) for the individual pore types.

Tab. 5.3.1: Summary of quantified parameters for all pore types

Parameter	Grain boundary pores	Sheet silicate pores	Solution pores	Microfractures
Frequency <sup>13</sup>	14.8 pores cm <sup>-1</sup>	1.2 pores cm <sup>-1</sup>	4.0 pores cm <sup>-1</sup>	2.6 pores cm <sup>-1</sup>
Width <sup>14</sup>	< 5 – 20 µm	< 5 µm	< 5 µm	< 5 – 10 µm
Mean impregnation depth	57 mm	47 mm	56 mm	53 mm
Maximum impregnation depth	72 mm	55 mm	66 mm	61 mm

<sup>13</sup> Mean value of number of structures between 0 and 7.5 cm perpendicular to the injection borehole.

<sup>14</sup> Only apertures from optical investigations, resolution > 5 µm.

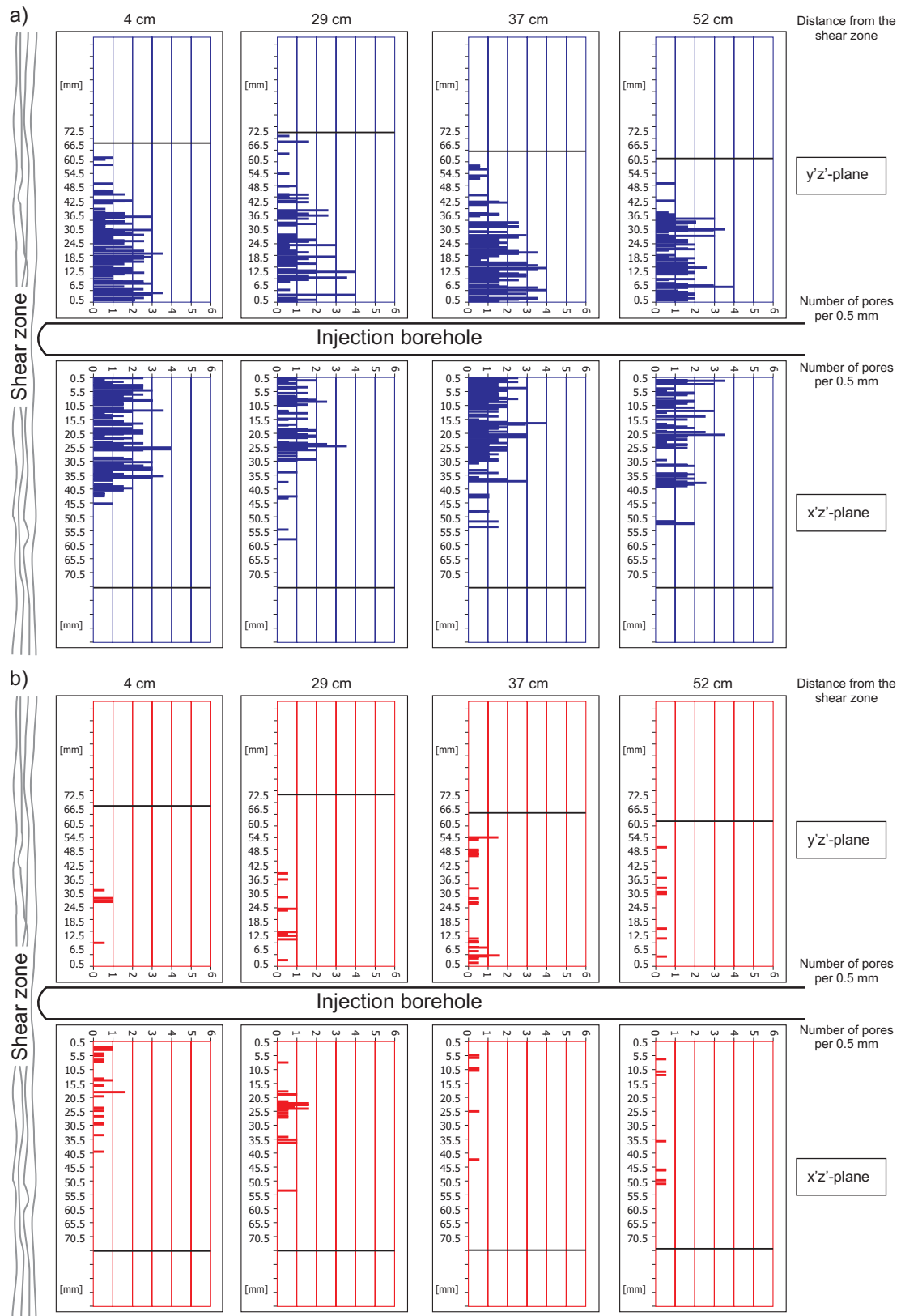


Fig. 5.2.5: Distribution of different pore types perpendicular to injection borehole (vertical axis) and with increasing distance from the shear zone (horizontal axis): a) Grain boundary pores, b) sheet silicate pores, c) solution pores and d) microfractures

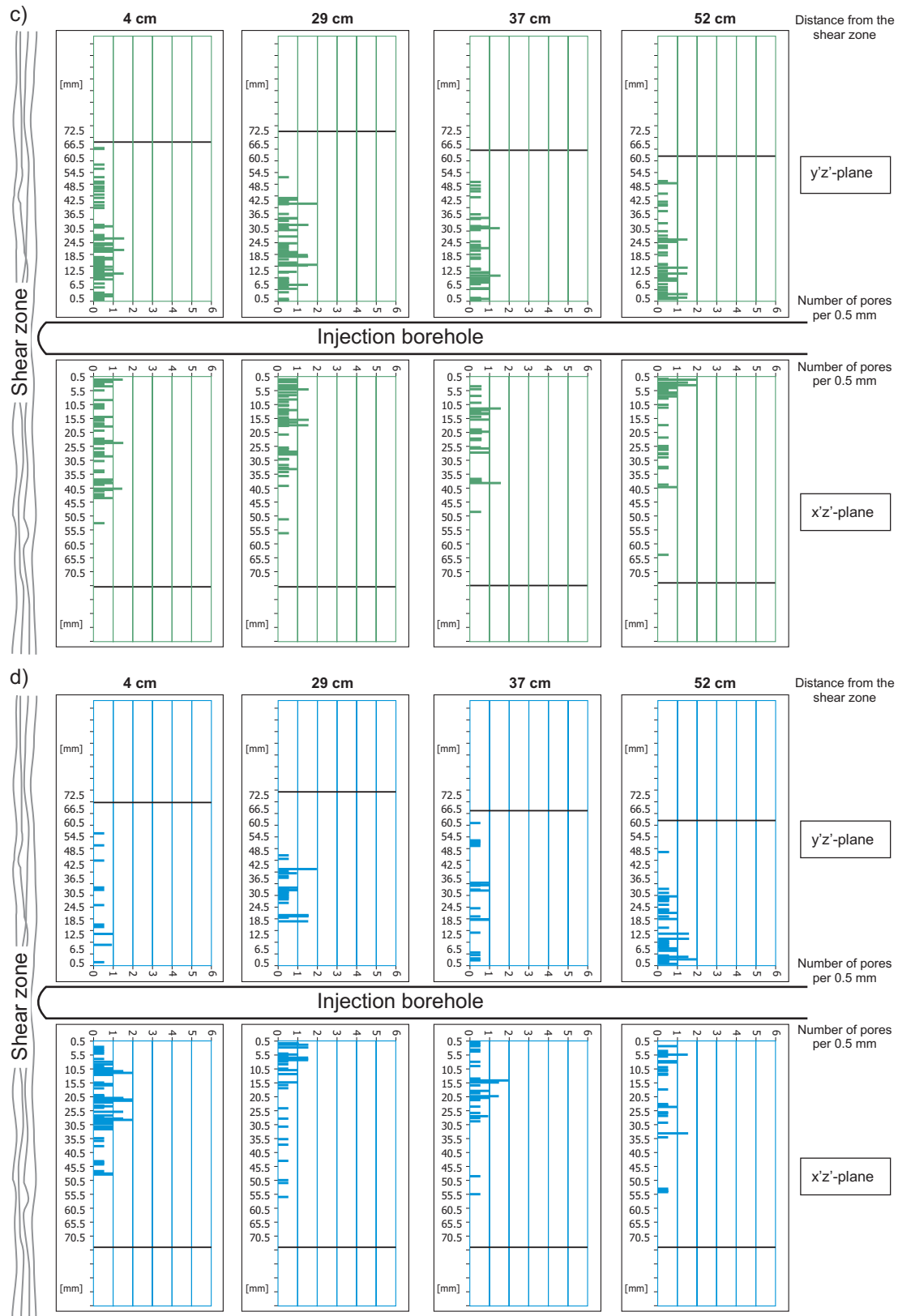


Fig. 5.2.5: (Continuation)



## 6 SCANNING ELECTRON MICROSCOPE INVESTIGATIONS OF *IN SITU* POROSITY

*K. Ota and T. Ando*

### 6.1 Methods

Numerous techniques exist for 2-D and 3-D imaging of pore space geometry so a literature study was conducted to evaluate the most appropriate method for the CP project. In the end, it was decided to evaluate a novel system with serial sectioning combined with scanning electron microscope (SEM) imaging, where the minimum pore size detectable is about 100 nm. In comparison to this technique, the shortcomings of the other methods may be summarised as follows:

1. CLSM (confocal laser scanning microscopy): see FREDRICH (1999) for a detailed discussion of the method, and FREDRICH et al. (1995) and HEATH & MONTOTO (1996) for examples of the application of the technique on rock samples. Resolution is only  $\sim 200$  nm and the volume of rock sample examined in each sweep is 2 to 3 orders of magnitude less than with the SEM.
2. 3-D reconstruction of sequential optical photomicrographs obtained by repeated polishing: while this method is effective, it is very time-consuming/tedious (see, for example, KOPLIK et al. 1984, LIN et al. 1986 and BYEGÅRD et al. 2001).
3. X-ray CT (computer tomography) and gamma-ray CT: according to BROWN et al. (1993) both methods have a lower resolution than SEM ( $100\ \mu\text{m} - 1\ \text{mm}$  and  $1\ \text{mm}$ , respectively).
4. MRI (magnetic resonance imaging): also has a lower resolution ( $\sim 25\ \mu\text{m}$ ).
5. Synchrotron computed microtomography: has a slightly higher resolution ( $7.5 - 10\ \mu\text{m}$ , SPANNE et al. 1994, AUZERAIS et al. 1996), but is presently not applicable to rock samples.

Here, detailed SEM examinations were performed on the sub-samples of core slab BOVE 97.007 at 1.40 m. The sub-samples at 30 to 55 mm from the injection borehole were examined, and those free of BDZ artefacts<sup>15</sup> were used for further study. Unpolished, broken surfaces and thin section (i.e. polished) surfaces were carefully examined in order to understand the nature of *in situ* connected porosity. Standard petrological observation was performed on the thin section by fluorescent microscopy for direct comparison with the SEM examination results.

A series of successive 2-D images of the resin-filled pore space was obtained by repeatedly grinding / polishing  $10\ \mu\text{m}$  off the sub-sample and capturing backscattered electron (BSE) images using the SEM. The BSE images clearly show atomic number contrast, which enable the easy distinction of resin-filled pore spaces from constituent minerals. 3-D reconstruction of the *in situ* connected porosity was created after a total of 51 pictures were digitised and appropriate 2-D images were processed through several steps of data treatment (e.g. line-thinning and thresholding) using commercially available visualisation software, which had been developed through JNC's Kamaishi *In Situ* Experiments (OTA et al. 1999). These images were finally used to produce a 3-D reconstruction of the *in situ* connected porosity.

---

<sup>15</sup> Core examinations in UV light revealed a 30 – 40 mm BDZ around the injection borehole.

## 6.2 Results and discussion

### 6.2.1 Visualisation of impregnated pore spaces with SEM

Fairly good impregnation was attained in pore spaces with apertures larger than a few  $\mu\text{m}$  along microfractures (Fig. 6.2.1) and also along grain boundaries (Fig. 6.2.2). Resin-filled pores with apertures of about 100 nm were occasionally identified along grain boundaries of quartz grains (Fig. 6.2.2) and along exsolution lamellae within K-feldspar grains. It is also expected that the acrylic resin NHC-9 may penetrate into pore spaces with apertures smaller than 100 nm because of its very small molecule size which is a few nm, as indicated from the results of the measurement of resin molecule sizes carried out at the JNC Tono Geoscience Centre (see also HASTRUP 1976).

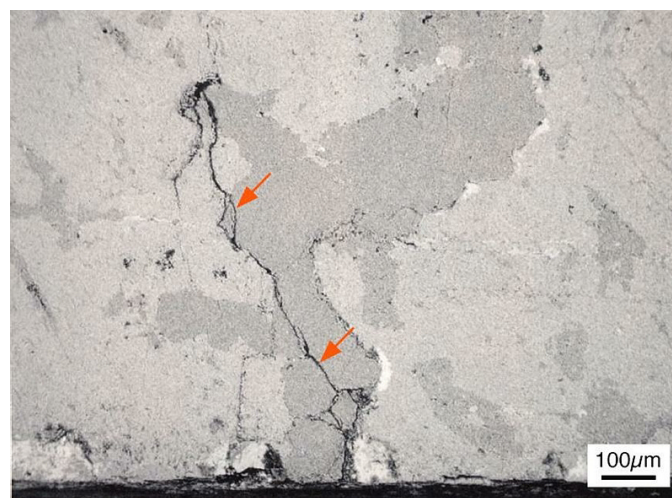


Fig. 6.2.1: BSE image of microfractures (orange arrows) within the Grimsel granodiorite matrix; the microfractures with apertures of larger than a few  $\mu\text{m}$  were fully filled with resin

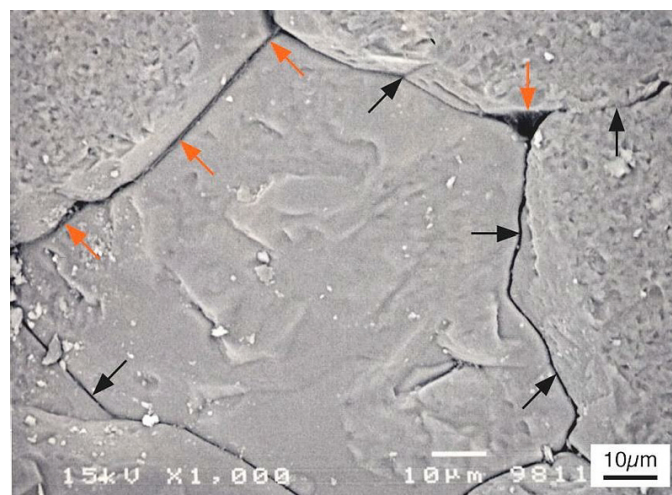


Fig. 6.2.2: BSE image of grain boundary pores showing various resin-filled pore spaces (orange arrows) with apertures ranging in size from about 100 nm up to a few  $\mu\text{m}$ ; resin-free pore spaces (black arrows) are also identified along grain boundaries

The SEM examination, however, revealed that the entire pore space was not filled with resin, even though the same pores were identified as thin yellow lines on the thin sections investigated under the fluorescent microscope at lower resolutions (Figs. 6.2.3a and b). This disagreement might be caused by partial resin lost from the sample surface during thin section preparation or by the effect that, even though resin impregnation is not complete through the whole thin section, UV illumination passes through and might induce fluorescence in the "hidden" part of the resin, giving the appearance of complete resin impregnation of the pore space on the surface (Fig. 6.2.4, case A; see Fig. 6.2.3a and b).

A similar appearance will also be produced when a pore space fully filled with the resin exists just below the surface (Fig. 6.2.4, case B; see Fig. 6.2.3a and b). Hence, in some cases, images obtained under UV illumination may represent neither the actual distribution, geometry nor interconnection of pore spaces in the matrix, tending to overestimate pore space frequency, aperture and availability. For example, the results of image analysis on both the BSE image (top image of Fig. 6.2.3a) and corresponding thin section photomicrograph (clipped image out of Fig. 6.2.3b) demonstrate that the percentage of the total area of resin-filled spaces estimated on the photomicrograph ( $0.023 \pm 0.007$ ) is approximately 2.6 times higher than that given by the BSE image ( $0.0089 \pm 0.0027$ ).

## 6.2.2 3-D reconstruction of impregnated pore space

Matrix porosity is made up of a network of four interconnected pore types: grain boundary pores, solution pores, sheet silicate pores and microfractures. It was shown that not all pore spaces along a certain pore type are accessible to the acrylic resin. The grain boundary pores and the microfractures have thin and elongated pore shapes in which "microchannels" (i.e. accessible spaces) and "barriers" (i.e. non-accessible spaces) certainly exist. In particular, 3-D reconstructions of matrix porosity revealed in detail its non-planar geometry and the "microchannel and barrier" structure (Fig. 6.2.5a).

An uneven microfracture plane is irregularly bent and often locally kinked and the barriers are mostly defined by sharp angular hinges, which suggests that such changes of the microporosity probably affect its accessibility to contaminants (Fig. 6.2.5b and c). Specifically, the following changes of pore space geometry can be considered:

- Pore spaces might be rather constricted near and at the hinge, reducing accessibility to contaminants.
- High tortuosity of pore spaces would lengthen pathways, causing a significant delay in the diffusion of contaminants into the barrier<sup>16</sup>.
- Rough surface of pore spaces might hinder the resin from diffusing into the barrier.

<sup>16</sup> Such tortuosity and constrictivity in the matrix pore space is usually treated simply in transport codes and combined into a single factor,  $G$ , the geometry factor. This is usually taken to be  $G = \bar{\sigma} t^2$  where  $\bar{\sigma}$  is constrictivity and  $t$  is tortuosity. The pore diffusion coefficient,  $D_p$ , is simply the quotient of the free water diffusion coefficient,  $D_w$ , and the geometry factor,  $G$ . This being the case, changes in  $G$  are normally treated by varying  $D_p$  in the transport codes (see also treatment in Chapter 9 and comments in Chapter 10).



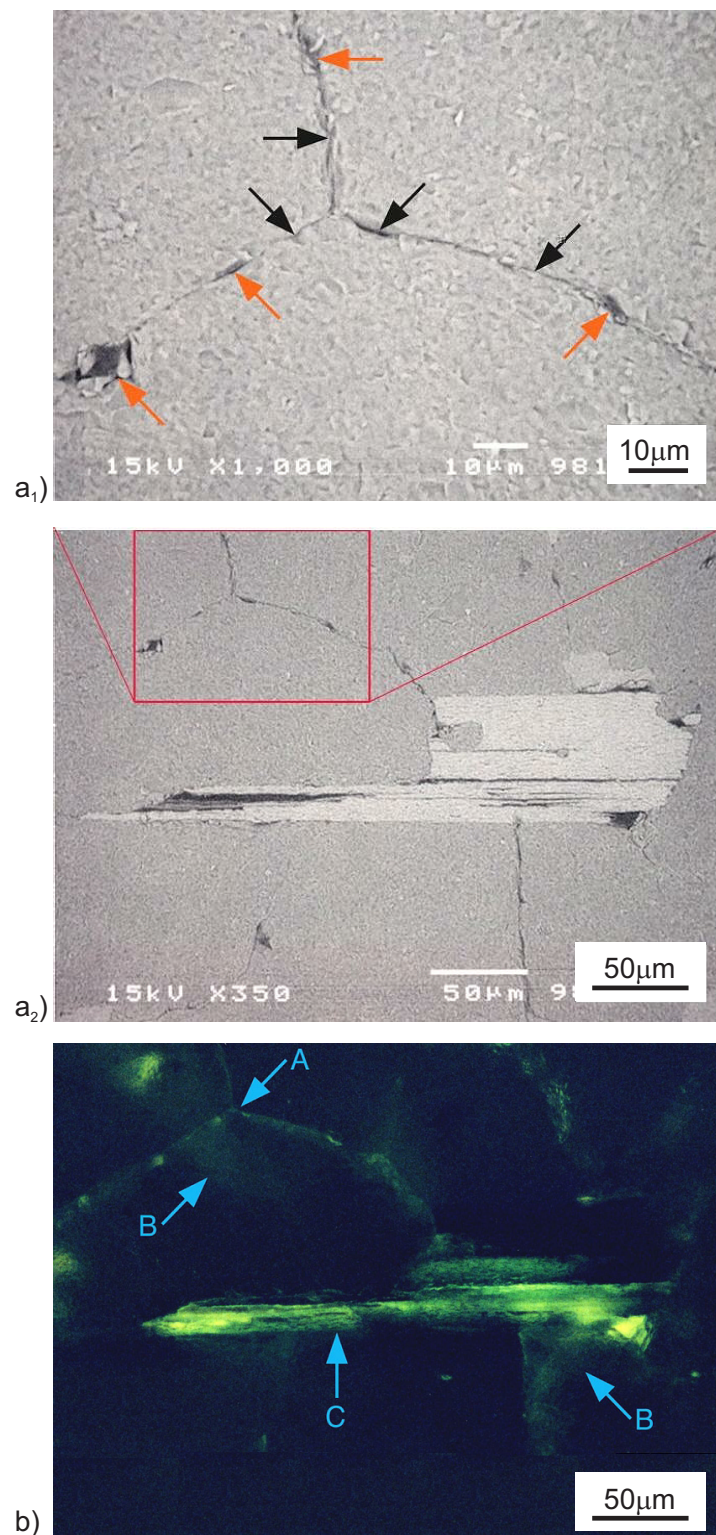


Fig. 6.2.3: BSE images (a<sub>1</sub> and a<sub>2</sub>) and corresponding photomicrograph (b) of pore types in the Grimsel granodiorite matrix, a disagreement in the appearance of the pore spaces is obviously seen between (a) and (b); (a) All pore spaces are not accessible to the resin (orange arrow: resin-filled pore space, black arrow: resin-free pore space), b) Labelled A, B and C are corresponding to the cases A, B and C, respectively, shown in Fig. 6.2.4



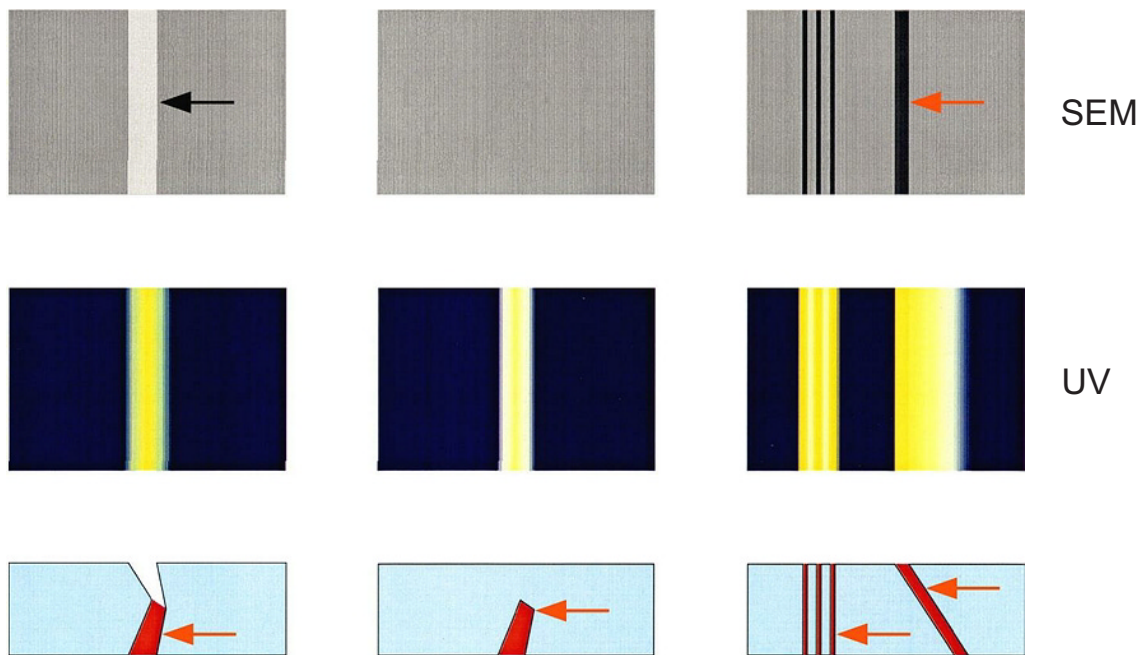


Fig. 6.2.4: Schematic representations of three possible cases of resin impregnation, which could cause differences in the appearance of the pores between SEM examination and fluorescent microscopy UV

Orange arrow: resin-filled pore space, black arrow: resin-free pore space.

### 6.3 Conclusions

Only part of the pore space within the matrix was found to be accessible for the resin due to the presence of "channel and barrier" structures with dimensions less than 1  $\mu\text{m}$ . 3-D images of the matrix porosity showed that the constrictive and/or tortuous geometry of the pore space is likely to reduce accessibility to diffusing contaminants and resin. Characterisation of the matrix porosity by standard petrological techniques may, in some cases, cause an overestimation of apertures, frequency and availability of pore space. Consequently, additional techniques were evaluated for the determination of the parameters so allowing estimation of the diffusion-accessible rock volume in the matrix (e.g. microscopic examinations in the order of nm to  $\mu\text{m}$  or chemical analysis of resin-filled pore space, see Chapters 7 and 8).

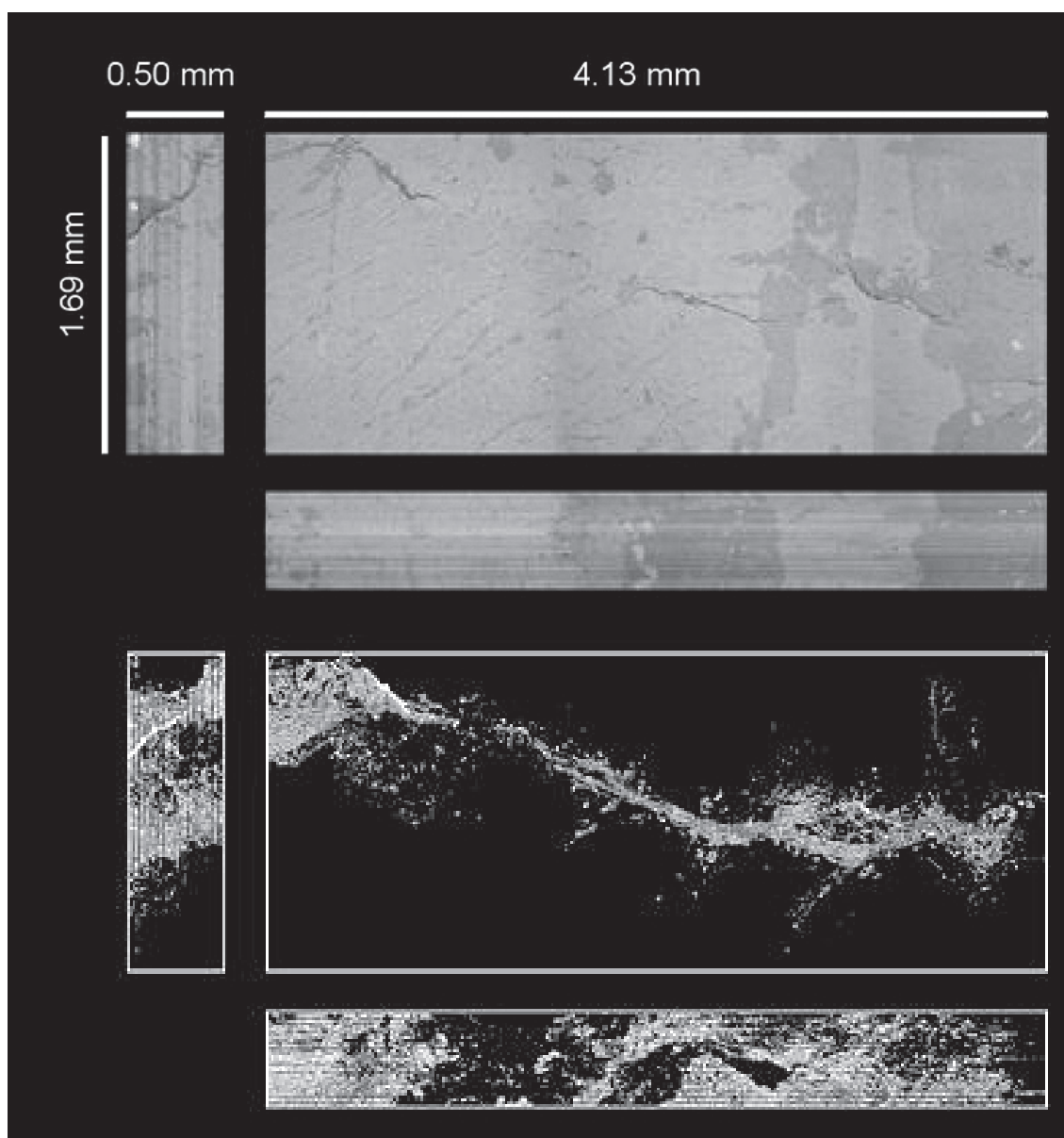


Fig. 6.2.5a: Top, left and bottom views of 3-D reconstructions of rock sample (top) and *in situ* connected porosity (bottom); these 3-D images consist of 51 2-D images that are 10  $\mu\text{m}$  apart

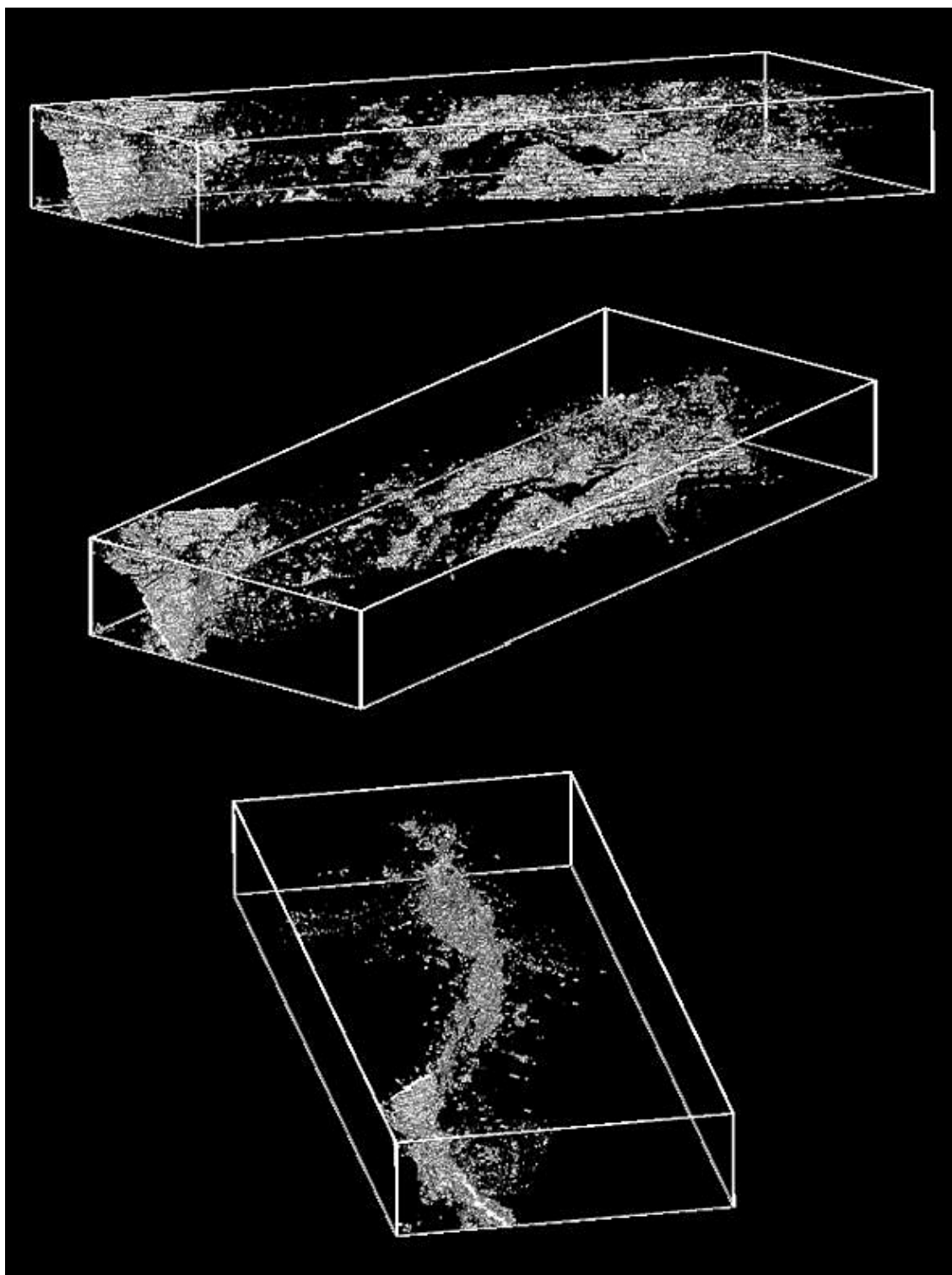


Fig. 6.2.5b: 3-D representations of *in situ* connected porosity from different viewpoints, showing the "microchannel and barrier" structure that reflects the constrictive and tortuous geometry of the rock matrix

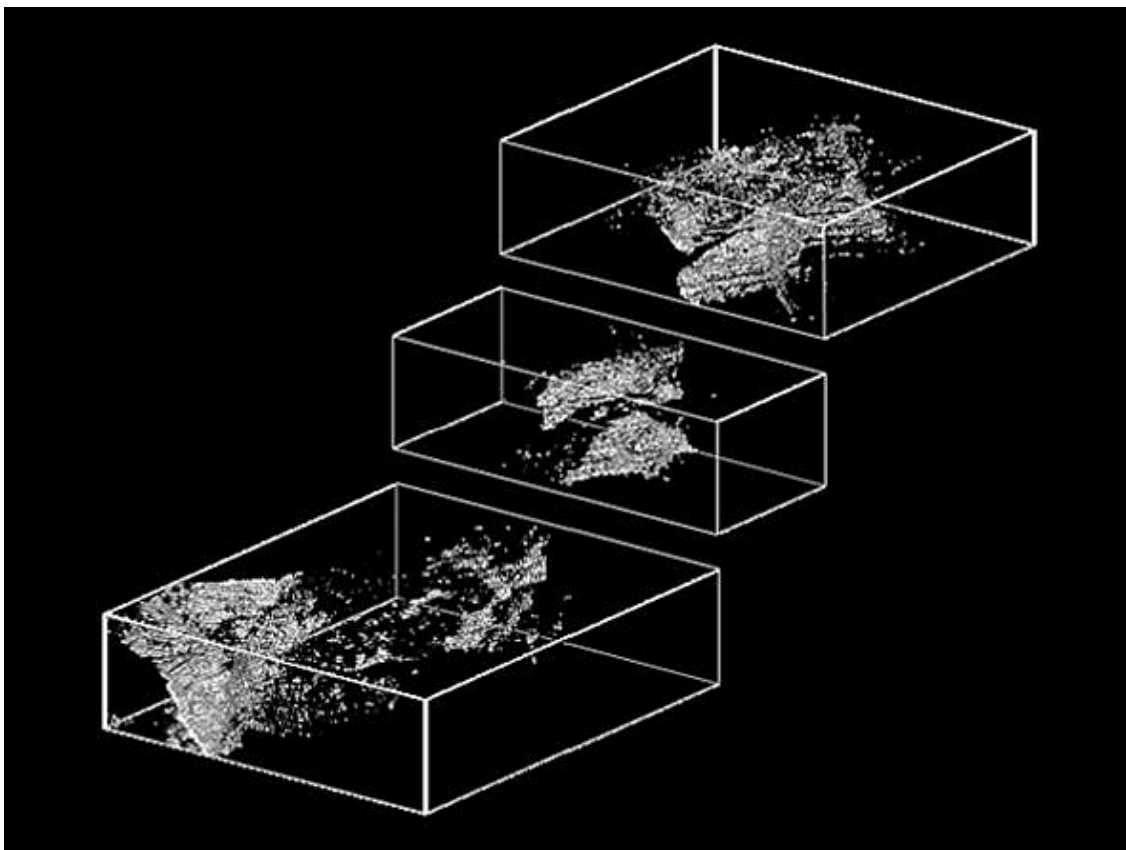


Fig. 6.2.5c: 3-D representations of *in situ* connected porosity in 3 segmented portions of the rock volume; the whole 3-D image from the same viewpoint is shown in Fig. 6.2.5b (middle)

## 7 UNIVERSAL-STAGE MEASUREMENTS AND DETERMINATION OF POROSITY, PERMEABILITY AND SEISMIC VELOCITIES

*M. Schild, S. Siegesmund, A. Vollbrecht and M. Mazurek*

A large laboratory programme of optical and petrophysical techniques was carried out at the University of Göttingen, Germany. The investigations were aimed at:

- determining the general orientations and frequencies of pore types
- determining the variation in permeability as a function of rock fabric
- determining the effective porosity on *in situ* impregnated and laboratory-impregnated samples
- determining the P-wave pattern

as a function of rock fabric, particularly with increasing ductile deformation in the vicinity of a shear zone. This work was intended to complement the work carried out in Switzerland and Japan by employing additional methods to assess the same questions being addressed by these two groups.

### 7.1 Methods

In addition to the analytical techniques mentioned below, the mineralogical composition of the samples was determined by transmitted light microscopy in combination with point counting and scanning electron microscopy (SEM) and cathodo-luminescence microscopy (see also Chapter 4).

#### 7.1.1 Sample reference system

The three samples examined for these studies came from sub-samples of the cores BOVE 97.004 and 97.005 and were named LS, SZ and HS. Sample SZ was taken from the immediate shear zone, sample LS from the southern side of the shear zone and sample HS from the northern side of the shear zone in order to check whether matrix porosity is a function of distance to the shear zone. All samples (thin sections, cylinders and spheres) were oriented with respect to the macroscopic fabric elements (cleavage, stretching lineation) as shown in Fig. 7.1.1. Like all other fabric diagrams, the pole figures were plotted on a Schmidt net (lower hemisphere) with the X axis oriented parallel to the stretching lineation, and Z axis lying coaxial to the foliation pole, and the XY plane parallel cleavage or foliation.

#### 7.1.2 Universal-stage measurements

The 3-D pattern (orientations and frequencies) of different pore types was measured on standard thin sections using a fluorescence microscope equipped with an Universal-stage. Around 200 pores in quartz, about 150 in feldspar, and about 200 mica cleavage planes were measured per section. In order to record all pore orientations, the measurements for each sample were carried out in three mutually perpendicular sections.

Composite pole figures were computed from the three sections and errors induced by the overlap of Schmidt net areas were eliminated statistically (for details see VOLLBRECHT et al. 1991). During Universal-stage measurements, the pore types are classified (SCHILD 1999) according to their host grain, their position (inter- or intragranular, interphase), and their state

(open, healed, sealed). For this particular study, however, only *in situ* impregnated pores and non-impregnated open pores were considered in order to discriminate *in situ* porosity from pores formed during core relaxation and sample preparation.

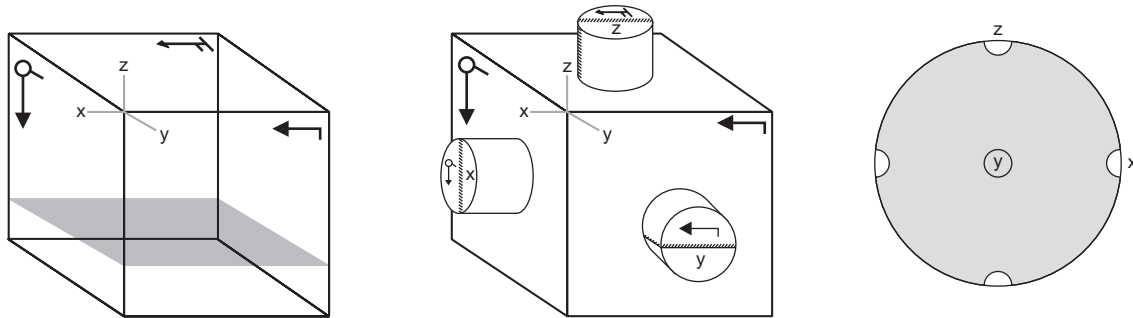


Fig. 7.1.1: Reference system of the sample orientation; a) schematic cube with foliation (XY-cleavage-plane) and lineation (x-direction), the arrows indicate the orientation of the thin sections, b) orientation of cylindrical samples for the permeability measurements, c) projection of the foliation and lineation in the Schmidt net, lower hemisphere, as used in the following

### 7.1.3 Porosity and permeability measurements

Porosity was determined by buoyancy weighting at room temperature on impregnated and non-impregnated samples. For the investigation of permeability, three cylindrical specimens were drilled orthogonally with respect to the microscopic fabric elements (see Fig. 7.1.1). The measurements were performed up to a confining pressure of 200 MPa. A pressure transient method using Argon gas as a flow medium was used. The gas pressure at the front of the sample was kept constant at 5 MPa. The pressure increase at the back, measured in a constant volume as a function of time, were used to calculate the permeability (for details see NOVER et al. 1995). The permeability was then used to calculate the hydraulic conductivity.

### 7.1.4 Seismic velocities

An experimental determination of the compressional wave velocities ( $V_p$ ) was performed to indirectly quantify the observed pore type patterns (see HEATH & MONTOTO 1996). The  $V_p$  measurements were carried out on spherical samples ( $\varnothing = 50 \text{ mm} \pm 0.01 \text{ mm}$ ) on dry and water saturated conditions at atmospheric pressure. Additionally, the complete patterns of  $V_p$  were determined up to a confining pressure of 100 MPa (see SIEGESMUND et al. 1993). The samples were covered by an epoxy resin film to protect them against the pressure medium.

The measuring system in which the samples were mounted allows a rotation of  $360^\circ$  on the vertical axes and  $75^\circ$  around the horizontal axes. Within this system it is possible to measure the P-wave velocity in any direction with the same accuracy. Usually, 132 independent measuring directions are analysed. The waves were generated and measured by piezoceramic transducers with a 2 MHz resonant frequency. Three different approaches were introduced: (i) velocity measurements at selected confining pressure levels, (ii)  $V_p$  at atmospheric pressures under dry and saturated (sat) conditions and (iii) analyses of the  $V_p$  pattern for comparable impregnated (labelled HS, SZ, LS) and non-impregnated (labelled HS<sub>(ni)</sub>, SZ<sub>(ni)</sub>, LS<sub>(ni)</sub>) rock samples.

## 7.2 Results

### 7.2.1 Petrography

The three investigated samples (HS, SZ and LS) show a comparable mineralogical composition. They are mainly composed of K-feldspar (12 – 24 vol%), plagioclase (29 – 30 vol%), quartz (27 – 28 vol%) and biotite (7 – 11 vol%) with accessory muscovite / sericite, apatite, sphene, epidote, zircon, chlorite, calcite and opaques. The samples show a clear foliation, which is most clearly pronounced in SZ samples. The foliation is indicated by quartz lenses and micaceous minerals with preferred orientation. Besides the various forms of the foliation the samples also show differences in terms of their brittle deformation fabric. The sample (LS) with the weakest foliation has a more marked cataclasis of the feldspars. These observations were confirmed by microscopic investigations.

### 7.2.2 Pore space fabrics

The pore types observed in these samples are sheet silicate pores, grain boundary pores within quartz polycrystals and microfractures in feldspars formed along cleavage planes. In addition, grain boundary pores between quartz and feldspars have been detected. There is no evidence that a significant number of open fractures were produced during sample preparation, since they show a consistent orientation in different thin sections. Moreover, the orientation and geometry of the micro-fractures is independent of the sample geometry.

A larger number of open non-impregnated sheet silicate pores were only observed parallel to the (001)-cleavage planes of micas and a distinction between open and non-impregnated pores was only possible by fluorescence microscopy at high magnification. Because alteration phenomena or mineral coatings along open non-impregnated cleavage planes are lacking, it is assumed that they mostly formed during core relaxation or sample preparation. It cannot be excluded that individual open cleavage planes formed earlier but were isolated from the interconnected network. The corresponding pole figures for grain boundary pores and microfractures are directly correlated with the mica textures and show comparable patterns for the three samples, i.e., a concentration close to the foliation normal (Z) and tendency to form a girdle around the lineation (Fig. 7.2.1a-c). The sample from the immediate shear zone (SZ) shows the strongest preferred orientation which corresponds to the distinct mylonitic foliation and the related mica textures. The scattering of poles from the Z- to the X-direction may be explained by lens-shaped feldspar porphyroclasts which control the shape orientation of the mica flakes. Accordingly, for sample SZ the stronger concentration of poles around Z can be related to increasing mylonitisation which causes a flattening and grain size reduction of the porphyroclasts.

Grain boundary pores around quartz polycrystals form a well developed inter-connected network which is almost completely impregnated indicating that these existed *in situ*. Their lengths range approximately between 100 and 200 µm. Scanning electron microscopy reveals that these pores display rather rough surfaces. In contrast, non-impregnated open grain boundary pores in quartz are comparatively rare and show maximum length of only 100 µm and smaller widths. In addition, few open microfractures were observed. The pole figures for open interconnected *in situ* pores (Fig. 7.2.1d-f) which are controlled by the prevailing grain boundary network show for all three samples an orthogonal pattern with a tendency of girdles around the reference axes (X, Y, Z). The intensity of preferred orientation, however, is low as compared with other pore types. The lowest intensity and a comparably diffuse pattern is developed in sample LS.

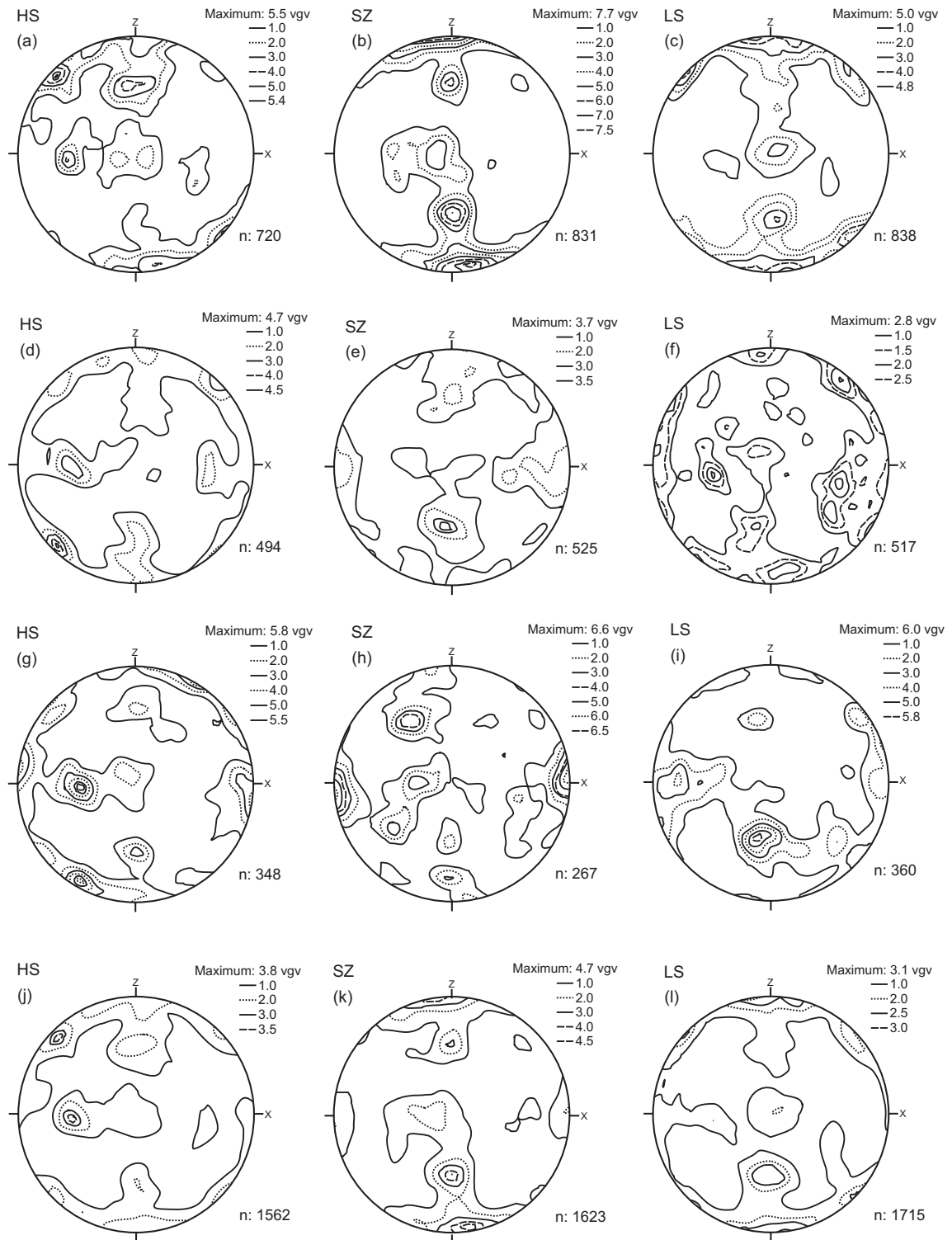


Fig. 7.2.1: Pole figures of pores for the samples HS, SZ and LS in: (a) to (c) (001) cleavage planes of micas; (d) to (f) grain boundary pores in quartz; (g) to (i) microfractures in feldspars; and (j) to (l) bulk microfractures fabric

Schmidt net, lower hemisphere; n = number of measured cracks and vgv = multiple of random distribution



The population of impregnated microfractures in K-feldspar comprises one or two sets of cleavage-parallel fracture sets and, in addition, irregular-shaped micro fractures often form an anastomosing network which usually cuts the cleavage parallel fractures at high angles (Fig. 7.2.1g-i). The widths of these irregular pores vary from section to section. For cleavage-parallel microfractures, it is apparent that *in situ* opening and impregnation preferentially occurred on pores which are inclined at high angle to the foliation (XY plane). In a few cases, impregnated microfractures were observed along K-feldspar phase boundaries too. The lengths of both cleavage parallel and irregular microfractures vary extremely with a maximum of about some 100  $\mu\text{m}$ , while the length of grain boundary pores is strongly dependent on the grain size. In contrast, non-impregnated microfractures in K-feldspar are very rare and often lack any connection with grain boundaries (as indicated by 2D observation in thin sections).

The impregnated microfractures in plagioclase display the same features as those in K-feldspar although the relative frequencies of the considered microfractures are different. In plagioclase, microfractures are less frequent, while grain boundary pores are more frequent than in K-feldspar. The intragranular microfractures are dominated by the irregular type described above. In contact zones between plagioclase and quartz polycrystals, the grain boundary pores of both phases form a common interconnected network, which sometimes also comprises microfractures in plagioclase. Plagioclase grain boundary pores are often decorated by mica flakes, these also contain minute microfractures which are connected with this network. As observed for K-feldspar, plagioclase also displays only few non-impregnated open pores. Most of them are very small isolated microfractures with irregular curved shapes. In addition, very few non-impregnated open microfractures parallel to twin lamellae have been observed.

In addition to the pores in the principal minerals of the rock described above, microfractures which run perpendicularly through the tight foliation also play an important role for the connected porosity, although they are rarely observed. Particularly in the sample SZ, they represent a more direct connection of the areas above and below mylonitic zones since, in these fine-grained areas the pore spaces are greatly reduced. Compared to the typical grain boundary-parallel fissures in quartz, they have a noticeably larger aperture, although the fissure generally runs parallel to the grain boundary.

Considering impregnated pores in K-feldspar and plagioclase together (Fig. 7.2.1j-l), the composite microfracture pole figures display orthogonal patterns which are comparable with those described for quartz (Fig. 7.2.1d-f). The intensity of preferred orientation, however is slightly lower for quartz. A significant deviation from this pattern is only given for sample LS.

All investigated samples of the granodiorite show a range of different *in situ* impregnated pore types. For non-impregnated open pores, however, it is still questionable whether they existed *in situ* but were not interconnected with the pore network or formed during core relaxation or later sample treatment. Microstructural features which are unequivocally indicative of an artificial origin of open pores in the prolongation of impregnated fractures were not observed. It was possible to identify distinct sets of pore patterns which strongly depend on the size, shape parameters and texture of their host minerals. For this reason, the geometry of the pore types is closely related to the bulk rock fabrics, i.e. it varies significantly from the shear zone into the less deformed wall rocks. The relative frequency and orientation of the different sets of pore types are schematically illustrated for each sample in Fig. 7.2.2 which is based on the intensity and the position of maxima in the corresponding pole figures (Fig. 7.2.1). Only the pores in feldspars and micas could be represented in this way because of the weak preferred orientation of the microfractures and grain boundary pores in quartz.

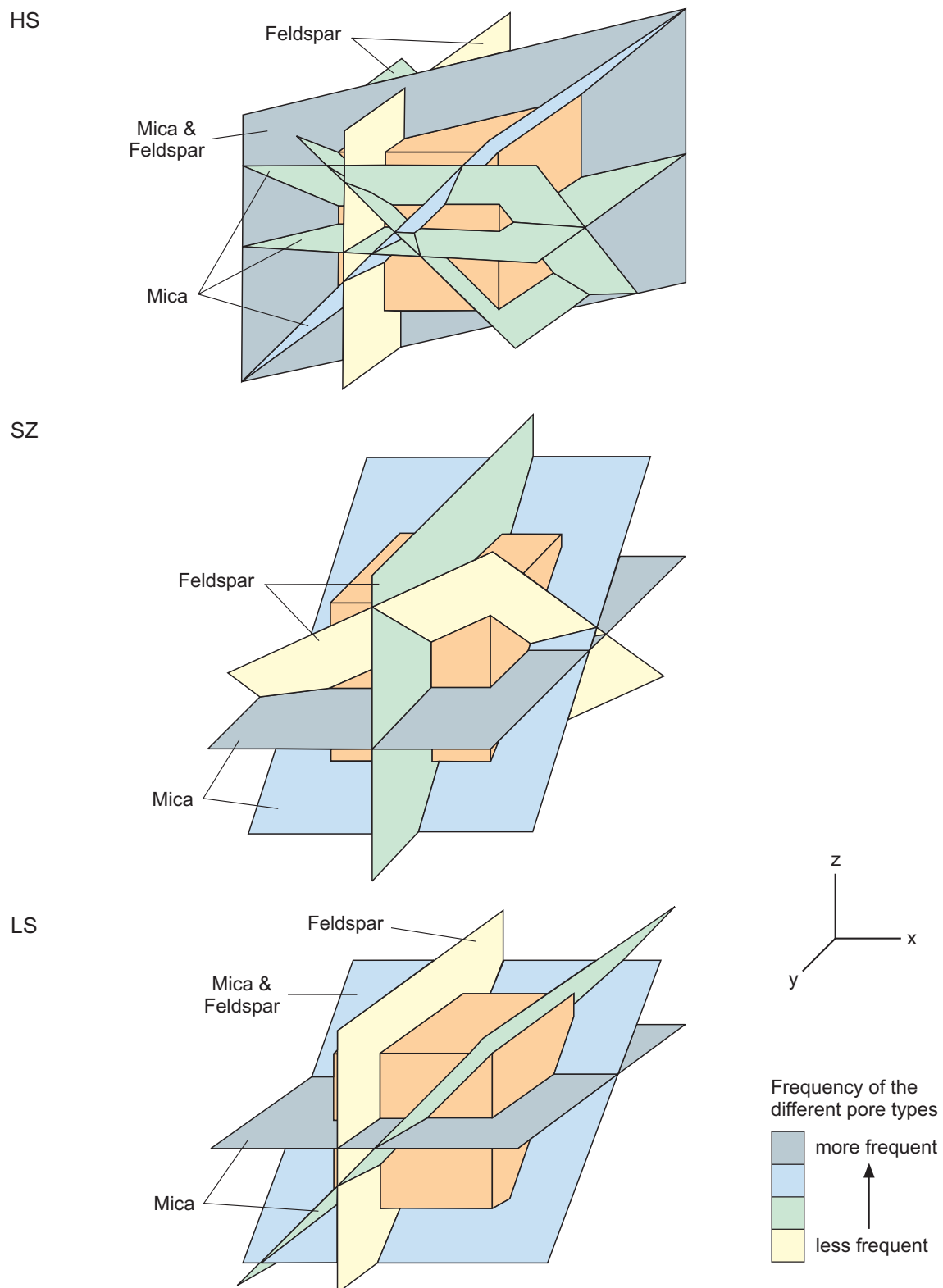


Fig. 7.2.2: Schematic illustrations of pore orientation (coloured planes) in sample cubes for HS, SZ and LS with reference axes (x, y, z)

From direct observation in thin sections, it is obvious that in all samples the intersections of different pore types build an interconnected network, which may allow diffusion of contaminants in all directions (see also SARDINI et al. 1999). Nevertheless, the main flow directions will be parallel to the cleavage planes, which represent favoured planar pathways due to their smooth surface. Rough microfracture surfaces induce a lower hydraulic aperture. A second subordinate flow direction may be given by intersection lines between prominent microfracture sets. As mentioned above, the preferred orientation of the (001)-cleavage parallel microfractures in the micas is an indicator for the foliation strength. It is most clearly developed in the sample of the immediate shear zone (SZ) and the sample from the southern side of the shear zone (LS).

Quartz-related microfractures and grain boundary pores should have no significant influence on any anisotropic properties (e.g., canalised fluid flow, mechanical behaviour) because of their weak preferred orientation, as mentioned above. However, their high frequency must be considered for potential nuclide retardation.

### 7.2.3 Porosity

The results of the porosity measurements are shown in Fig. 7.2.3. The porosity in the standard non-impregnated (ni) samples covers at GTS usually the range of 0.8 to 1.5 vol% (BOSSART & MAZUREK 1991). The *in situ* impregnated samples clearly show a lower porosity for all samples with values between 0.55 and 0.59 %.

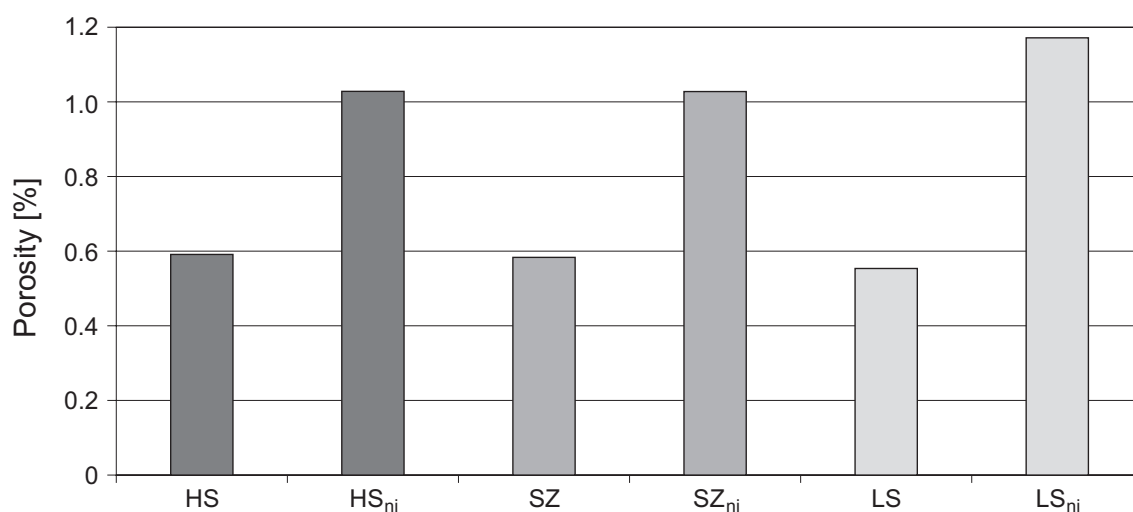


Fig. 7.2.3: Porosity of impregnated and non-impregnated (ni) samples

In crystalline rocks in general, porosity determined in the laboratory usually yields consistent results, irrespective of the applied analytical method (e.g. RASILAINEN et al. 1996). However, all laboratory methods suffer from the same systematic errors, namely the effects of stress relaxation, sampling procedures and sample preparation methods on the results.

Hg injection porosity measurements on undeformed Grimsel granodiorite samples in the laboratory revealed porosities in the range of 0.8 – 1.5 vol% (BOSSART & MAZUREK 1991). For crystalline rocks that were not subjected to hydrothermal alteration, these are relatively high values and are explained by the abundance of a natural system of different pore types and the substantial albitisation of magmatic plagioclase during greenschist-stage metamorphism. These values are consistent with the data presented in Fig. 7.2.3 for samples that were not impregnated *in situ*.

Samples that were impregnated by resin injection *in situ* should result in zero porosity in the laboratory. However, as Fig. 7.2.3 shows, this is not the case, and ca. 0.6 vol% is measured. This porosity is most likely an artefact, i.e. created by unloading and sample treatment. Thus, *in situ* matrix porosity, calculated by difference between the values for impregnated and non-impregnated samples, is ca. 0.4 – 0.5 vol%, i.e. one third to one half the porosity that is measured on conventional samples in the laboratory. Thus either the pore apertures in the natural pore system were enhanced, or new pores were created as a result of unloading and sample treatment.

#### 7.2.4 Hydraulic conductivity

The dependence of the permeability / hydraulic conductivity on the applied confining pressure is shown in Fig. 7.2.4 and Tab. 7.2.2. The permeability decreases by about one order in magnitude at pressure between 5 MPa up to 20 MPa (Fig. 7.2.4). The anisotropy of the permeability that was measured in different directions regarding to the foliation is obvious. In general the permeability is low normal to the foliation plane while larger values were detected even at high confining pressures within the foliation plane thus indicating that pores remain still open up to pressures of 20 MPa (e.g. see Tab. 7.2.2).

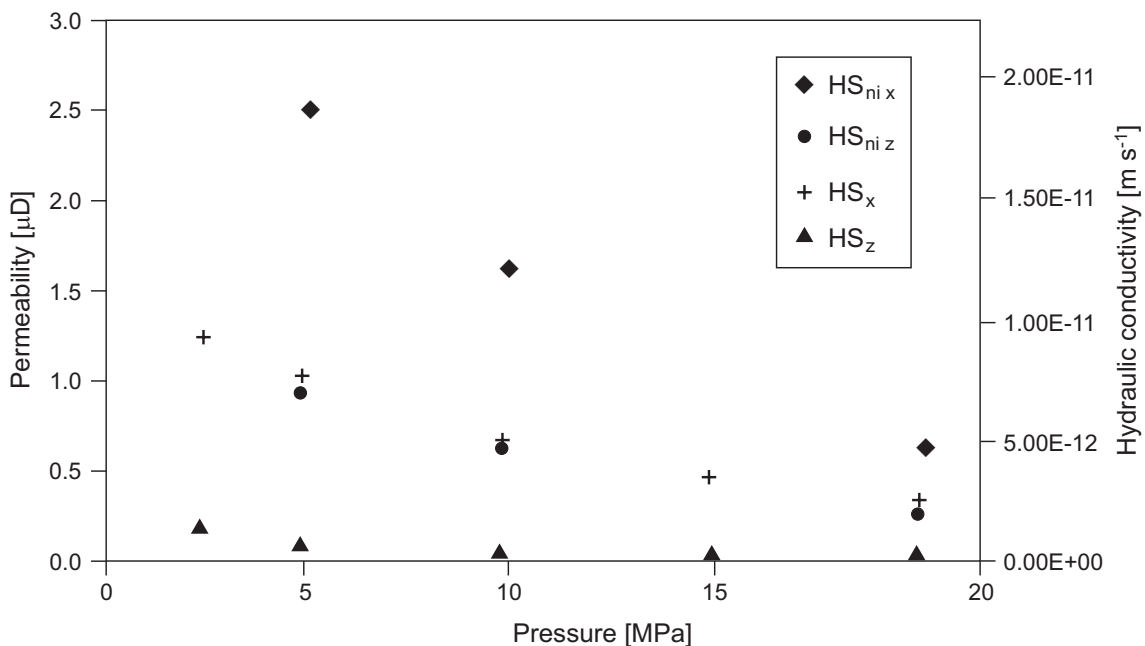


Fig. 7.2.4: Pressure dependent permeability/hydraulic conductivity of HS impregnated and non-impregnated (ni) in X- and Z-direction

A comparison of the permeability / hydraulic conductivity for the non-impregnated and the impregnated sample of HS shows lower permeabilities for the impregnated sample. The difference parallel to the lineation (X-direction) is 1.5  $\mu\text{D}$  at 5 MPa. With increasing pressure, the difference decreases to 0.3  $\mu\text{D}$  at 20 MPa while in the direction normal to the foliation (Z), it is 0.8  $\mu\text{D}$  at 5 MPa and 0.2  $\mu\text{D}$  at 20 MPa.

For the other samples (SZ, LS) the permeability / hydraulic conductivity is generally lower (see Tab. 7.2.2). Furthermore, in the Z-direction, the permeability of the non-impregnated samples is greater than that of the impregnated samples. The inverted difference in X-direction is possibly

caused by larger crystals of feldspar within the cylindrical specimen. This would also affect the preferred orientation of microfractures which may serve as pathways for the flow medium.

Tab. 7.2.2: Pressure dependent permeability and hydraulic conductivity of impregnated (imp) and non-impregnated (ni) samples in the direction parallel to the lineation (x) and perpendicular to the foliation (z)

Sample	Permeability [μD]	Conductivity [m s <sup>-1</sup> ]	Permeability [μD]	Conductivity [m s <sup>-1</sup> ]
Pressure [MPa]	5	5	20	20
HS x	1.0506	$7.89 \times 10^{-12}$	0.3841	$2.89 \times 10^{-12}$
HS z	0.1189	$8.93 \times 10^{-13}$	0.0355	$2.67 \times 10^{-13}$
HS <sub>ni</sub> x	2.5241	$1.90 \times 10^{-11}$	0.6513	$4.89 \times 10^{-12}$
HS <sub>ni</sub> z	0.8947	$6.72 \times 10^{-12}$	0.2247	$1.69 \times 10^{-12}$
Pressure [MPa]	2.5	2.5	20	20
SZ x	0.7654	$5.75 \times 10^{-12}$	0.2152	$1.62 \times 10^{-12}$
SZ z	0.1743	$1.31 \times 10^{-12}$	0.057	$4.28 \times 10^{-13}$
SZ <sub>ni</sub> x	0.5783	$4.35 \times 10^{-12}$	0.1522	$1.14 \times 10^{-12}$
SZ <sub>ni</sub> z	0.3487	$2.62 \times 10^{-12}$	0.0948	$7.12 \times 10^{-13}$
Pressure [MPa]	5	5	20	20
LS x	0.7998	$6.01 \times 10^{-12}$	0.2046	$1.52 \times 10^{-12}$
LS z	0.213	$1.60 \times 10^{-12}$	0.0602	$4.52 \times 10^{-13}$
LS <sub>ni</sub> x	0.5129	$3.85 \times 10^{-12}$	0.0753	$5.66 \times 10^{-13}$
LS <sub>ni</sub> z	0.433	$3.25 \times 10^{-12}$	0.1334	$1.00 \times 10^{-12}$

In order to estimate the *in situ* permeability / hydraulic conductivity, it is necessary to consider the *in situ* stress field. In the GTS, the maximum principle stress ( $\sigma_H$ ) ranges between 18 and 45 MPa, the minimum horizontal stress ( $\sigma_h$ ) is almost 10 MPa less (KEUSEN et al. 1989). The lithostatic principal stress ( $\sigma_v$ ) reaches 8 to 12 MPa, the hydrostatic pressure (P) is 4 MPa. For average values, the effective stress ( $\sigma_{\text{eff}} = \sigma - P$ ) is estimated to  $\sigma_{\text{Heff}} = 30$  MPa,  $\sigma_{\text{heff}} = 19$  MPa and  $\sigma_{\text{veff}} = 7$  MPa. Hence measurements at a confining pressure of 20 MPa and 30 MPa should give the most appropriate approximation of *in situ* conditions (although this is obviously only applicable for the non-impregnated samples, because in the impregnated samples only the artificial component was measured).

The hydraulic conductivity at a confining pressure of 20 MPa ranges between  $4.9 \times 10^{-12}$  m s<sup>-1</sup> in x-direction and  $1.7 \times 10^{-12}$  m s<sup>-1</sup> in z-direction for the non-impregnated sample HS<sub>ni</sub>. For SZ<sub>ni</sub> the permeability is  $1.14 \times 10^{-12}$  m s<sup>-1</sup> and  $7.12 \times 10^{-13}$  m s<sup>-1</sup>, respectively, and for LS<sub>ni</sub>  $5.7 \times 10^{-13}$  m s<sup>-1</sup> and  $1.0 \times 10^{-12}$  m s<sup>-1</sup>, respectively (see Tab. 7.2.2).

The dependence of hydraulic conductivity on confining pressure is relatively small. As shown in Fig. 7.2.4, the hydraulic conductivity of impregnated samples is less than half that of non-impregnated samples and the measured values are on the order of  $1 \times 10^{-11}$  m s<sup>-1</sup>. KULL et al. (1993) derived large-scale (decametres along tunnel) matrix conductivities by measuring the evaporative water discharge from the unfractured tunnel surface and obtains typical values of 1 to  $3 \times 10^{-11}$  m s<sup>-1</sup>. Thus the large-scale *in situ* measurements are quite consistent with the small-scale laboratory values presented here. It appears that unloading / sample preparation does not critically affect laboratory measurements and applying confining pressure for laboratory tests appears to yield hydraulic conductivities similar to those measured *in situ*.

### 7.2.5 Seismic velocities

A characteristic experimental data set for P-wave velocities as a function of the confining pressure at room temperature is shown in Fig. 7.2.5. The general behaviour of  $V_p$  for the applied approaches can be inferred by comparing Fig. 7.2.6 and 7.2.7. The P wave velocities at atmospheric pressure are higher in saturated rocks than unsaturated rocks due to the limited compressibility of water-saturated pores in contrast to air-filled ones (MONTOTO et al. 1992 obtained the same results for a variety of crystalline rocks). At higher confining pressures, the curves are only slightly different (see NUR & SIMMONS 1969, POPP 1994). The degree of influence of saturation depends on the matrix porosity. For impregnated rock samples, the  $V_p$  may be higher due to the higher Young's modulus of the acrylic resin compared to water (see Fig. 7.2.6d-e and Fig. 7.2.7d-e).

The Grimsel granodiorite samples show, at low confining pressure, a pronounced directional dependence (Fig. 7.2.6a, Fig. 7.2.7a).  $V_{p_{\min}}$  can be observed normal to the foliation ( $3.22 \text{ km s}^{-1}$ ) whereas  $V_{p_{\max}}$  is parallel to the lineation ( $4.85 \text{ km s}^{-1}$ ) for SZ<sub>ni</sub>. This sample shows a remarkable pressure dependence. The velocities of elastic waves increase with confining pressure which is usually attributed to progressive closure of pores (see Fig. 7.2.6b, Fig. 7.2.7b). The maximum pressure-dependent increase of  $V_p$  can be observed for the Z-direction. In order to explain the low pressure phenomena,  $\Delta V_p$  (given by the difference between  $V_p$  values measured at 100 MPa and at 3 MPa) were calculated for SZ<sub>ni</sub> (Fig. 7.2.7c). As mentioned above, the corresponding pore types are dominated by microfractures and grain boundary pores in biotite and muscovite. Grain boundary pores commonly extend into the (001)-mica cleavage planes as represented by the pole figures (Fig. 7.2.1a-c). For water saturated conditions, the most pronounced  $V_p$  increase as compared with dry conditions is observed sub-parallel to the foliation pole which can be related to the saturation of grain boundary pores. This is clearly demonstrated in the  $\Delta V_p$  stereogram (Fig. 7.2.7f) where the difference is given for saturated and dry conditions. To illustrate the effect of impregnation samples, SZ and SZ<sub>ni</sub> can be directly compared:  $V_{p_{\text{SZ}_{ni} \max}} = 4.70 \text{ km s}^{-1}$  (dry),  $5.56 \text{ km s}^{-1}$  (sat),  $V_{p_{\text{SZ} \max}} = 5.14 \text{ km s}^{-1}$  (dry) and  $5.66 \text{ km s}^{-1}$  (sat), respectively. Both samples (impregnated and non-impregnated) show comparable velocity distributions (Fig. 7.2.6d-f). The velocity patterns agree with those obtained from the non-impregnated ones. However, the impregnated sample shows a significantly higher velocity, especially normal to the foliation, while the high velocity direction is less affected (Fig. 7.2.6d-f). Comparing Fig. 7.2.6f and Fig. 7.2.7f, it becomes evident that the observed pore type population was sealed with acrylic resin. The grain boundary pores which are mainly oriented parallel to the foliation reflect the *in situ* connected porosity.

A quantitative estimate of the total *in situ* open interconnected porosity in relation to their position to the shear zone, i.e. southern part of the shear zone (LS), northern part of the shear zone (HS) and directly from the centre of the shear zone (SZ), the maximum anisotropy [ $A_{V_p}(\%) = (V_{p_{\max}} - V_{p_{\min}}) / V_{p_{\max}} \times 100$ ] can be used;  $A_{V_p}$ : 21.8 % (SZ), 10.3 % (LS) and 17.0 % (HS), respectively.

The rapid  $V_p$  increase at lower pressures up to 100 MPa (as shown in Fig. 7.2.5) is associated with the progressive closure of pores (e.g. BIRCH 1960a and b, BRACE 1965). At higher pressures, the curves become nearly linear, indicating that intrinsic velocities are approached, reflecting the properties of a nearly pore-free rock volume. The assumption of isotropy is valid only for rocks with a random distribution of minerals, pores etc., a very special case and generally not realised in natural rocks. Commonly, most of the rocks are anisotropic when considering physical rock parameters as well as fabrics. It is important to note that the intrinsic elastic properties and its anisotropy at higher pressures originate from the elastic properties of the constituent minerals and their crystallographic fabrics. The difference of velocities measured at high and low confining pressures (below the pore-closing pressure) should be mainly attrib-

uted to the contribution of pores. Therefore, the spatial dependence of  $V_p$  has been studied exclusively on spherical samples, allowing the determination in any direction.

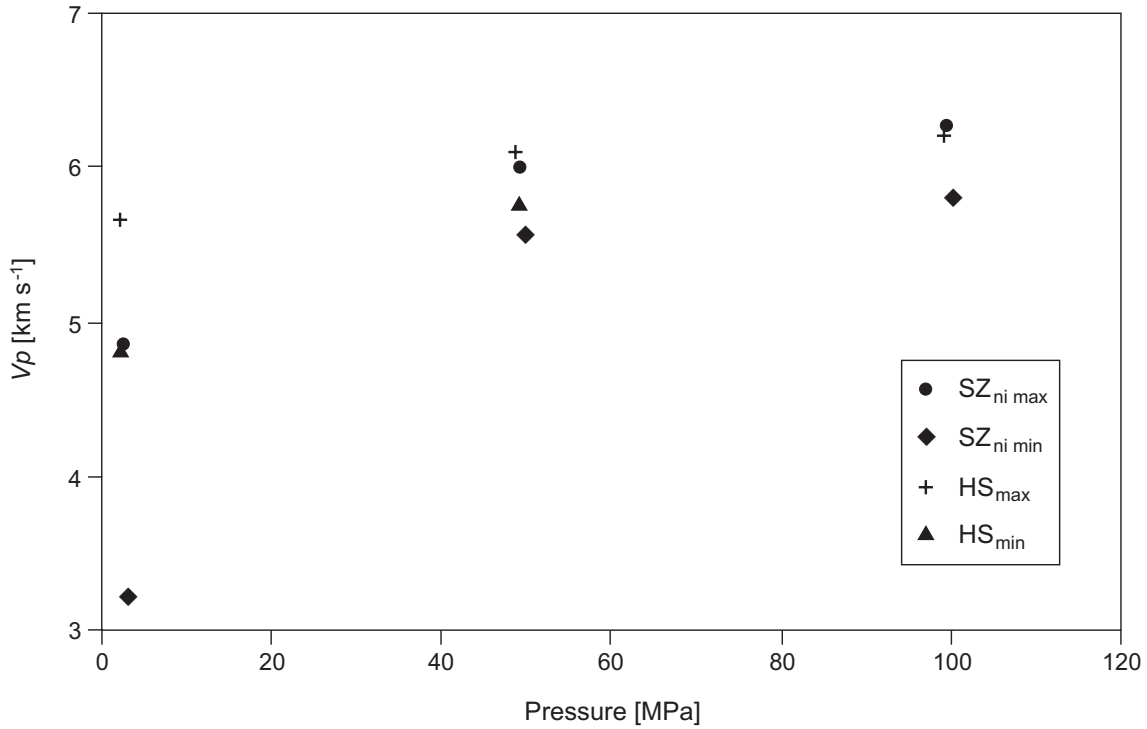


Fig. 7.2.5: Pressure dependent seismic velocity of the non-impregnated sample SZ and the impregnated sample HS of two selected propagation directions

The correspondence between the pressure dependence of the complete  $V_p$  distribution and the observed dominant pore type populations shows that they control the seismic anisotropy at low confining pressures. The most important observation is that the symmetry of the  $V_p$  distribution does not change with either pressure or saturation in both the impregnated and non-impregnated samples. At high pressures, where most of the pores are closed, the residual anisotropy is mainly controlled by the texture of biotite and muscovite. The significance and effective influence of the bulk microfracture fabrics on  $V_p$  can be best demonstrated by the  $\Delta V_p$  patterns. This is clearly indicated by the very good correlation between pole figures and the corresponding  $V_p$  stereograms (compare Fig. 7.2.2 and 7.2.6). Therefore, the influence of the preferred orientation of biotite and muscovite is twofold. They control the intrinsic properties and the orientation of the most significant pore types, i.e., sheet silicate pores parallel to the (001)-cleavage planes. Moreover, from comparison of the  $V_p$  characteristics of impregnated and non-impregnated samples and their saturation behaviour, it follows that the *in situ* pores are mostly interconnected.

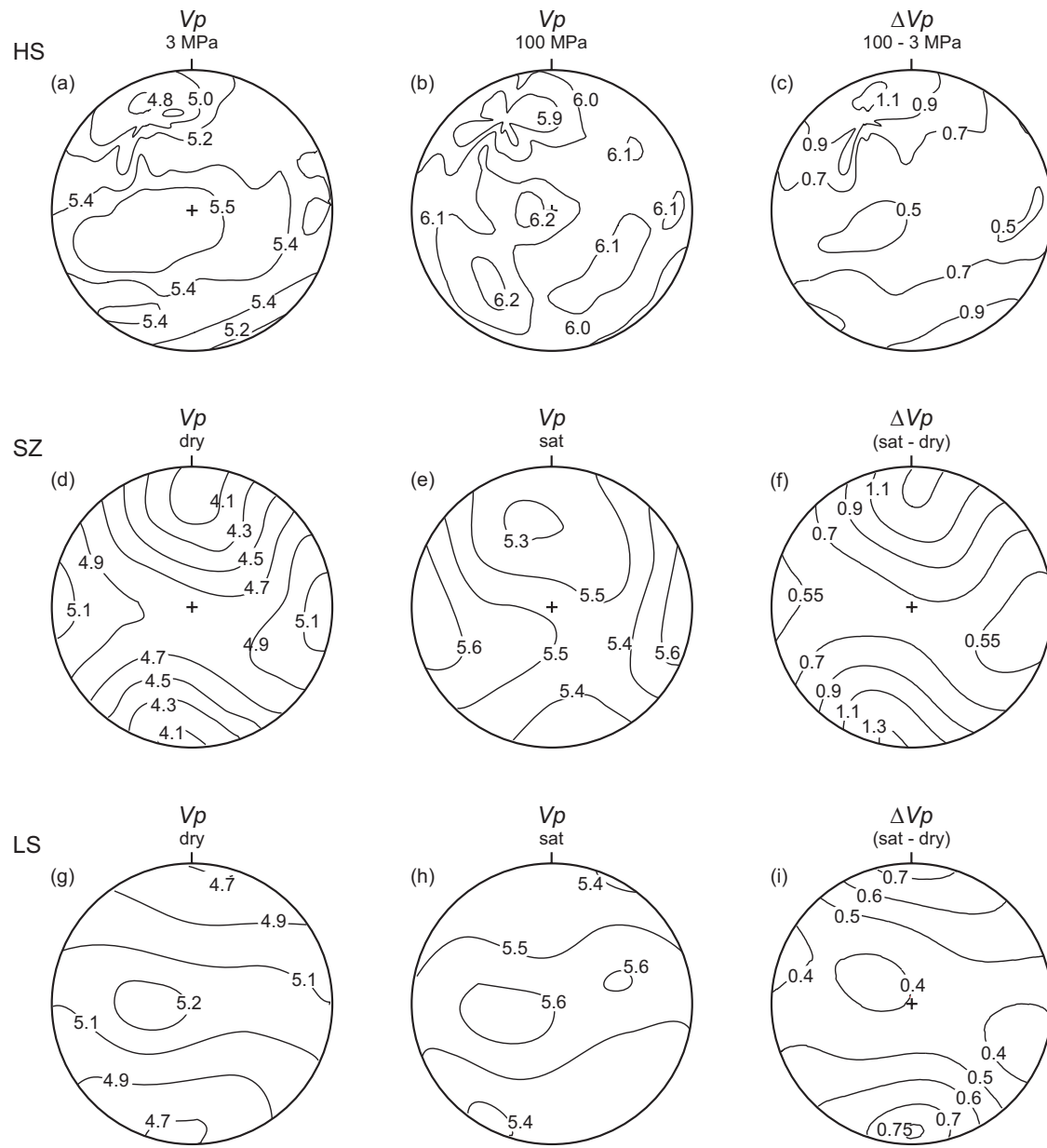


Fig. 7.2.6: Experimentally determined directional dependence of compressional wave velocities [ $\text{km s}^{-1}$ ] for the impregnated samples HS, SZ and LS: (a) and (b)  $V_p$  as a function of confining pressure, (c)  $\Delta V_p$  between 100 and 3 MPa confining pressure, (d) and (g)  $V_p$  under dry conditions, (e) and (h)  $V_p$  under saturated conditions; and (f) and (i)  $\Delta V_p$  (sat - dry) as a measure of the microfracture induced anisotropy; Schmidt net, lower hemisphere



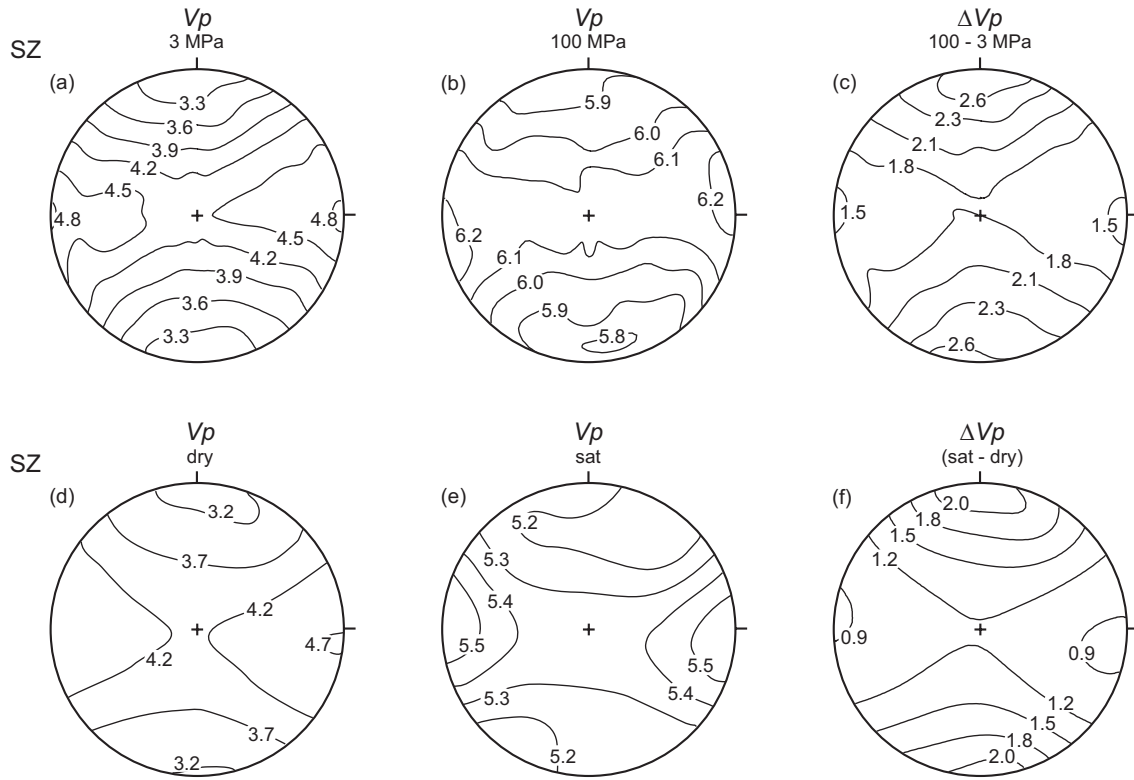


Fig. 7.2.7: Seismic velocity [ $\text{km s}^{-1}$ ] of the non-impregnated sample SZ: (a) at a confining pressure of 3 MPa, (b) at a confining pressure of 100 MPa, (c)  $\Delta Vp$  between 100 and 3 MPa confining pressure, (d)  $Vp$  under dry conditions, (e)  $Vp$  under saturated conditions, and (f)  $\Delta Vp$  (sat - dry) as a measure of the anisotropy induced by microfractures; Schmidt net, lower hemisphere

To quantify the influence of the *in situ* pores on the  $Vp$  pattern,  $\Delta Vp$  as a difference between  $Vp_{SZ_{dry}}$  and  $Vp_{SZ_{ni_{dry}}}$  has to be calculated. In this case, the residual  $Vp$  pattern only reflects the contributions of impregnated pores because the effect of the intrinsic properties of isolated (and therefore not impregnated) open pores originated by stress release after core extraction and sample treatment is eliminated. The  $\Delta Vp$  diagram indicate that, beside the sheet silicate pores, connected microfractures in quartz and, especially, in feldspar also contribute significantly. However, this observation is only valid if the core relaxation after impregnation and extraction is comparable for the samples SD and  $SZ_{ni}$  because the velocity difference between dry and saturated impregnated rock samples (Fig. 7.2.6d-e, 7.2.7d-e) indicates a distinct amount of pore opening. As a total, the *in situ* impregnated pores are responsible for a porosity of about 0.5 % (given as the difference between  $SZ_{ni}$  and SD).

### 7.3 Conclusions

Detailed microfabric analysis clearly revealed that the orientation and relative frequency of individual sets of pore types strongly depends on the fabric and texture of the related host rock minerals. The increase in intensity of planar (001)-cleavage planes towards the shear zone was observed and leads to an increase in the corresponding sheet silicate pores and intergranular microfractures. Similar conclusions could be drawn for matrix permeability where permeability/

hydraulic conductivity are strongly related to the rock foliation and are usually minimal perpendicular to the foliation. Assuming a confining pressure of 20 MPa, which closely approximates the *in situ* conditions, a hydraulic conductivity of about  $1 \times 10^{-12} \text{ m s}^{-1}$  was evaluated as realistic. The comparison of standard laboratory determinations of matrix porosity with the *in situ* values derived here indicate that stress release and sample preparation in the laboratory enhance *in situ* porosity values by a factor of 2 to 2.5. One additional unknown remains in the unquantified effects of drilling of the injection boreholes, such that the real *in situ* values could be even smaller (although, as the samples were taken from outwith the BDZ, this is unlikely).  $V_p$  data reflect a strong geometric relationship between the  $\Delta V_p$  stereograms and the microcrack pole figures considering the impregnated and non-impregnated samples under dry and water saturated conditions. The  $\Delta V_p$  values between impregnated and non-impregnated samples reflect the bulk microcrack patterns which effectively influence the  $V_p$  anisotropy at lower confining pressures (below 20 MPa). An influence especially on the cracks in mica, connected cracks in quartz and those in feldspar could be recognised in the  $\Delta V_p$  stereogram, too. These crack sets which are mainly oriented parallel to the foliation produce a marked open connected porosity also at *in situ* conditions at the Grimsel Test Site. Moreover, the direct comparison of  $V_p$  between dry and saturated conditions allow a quantitative measure between open *in situ* cracks and those effects originated by stress release after core extraction as well as sample treatment.

## 8 WATER SATURATION GRAVIMETRY, MERCURY INJECTION POROSIMETRY AND CHEMICAL ANALYSIS POROSIMETRY

*K. Ota*

### 8.1 Methods

#### 8.1.1 Sample preparation

A quarter of the slab, sawn off from the large-diameter ( $\varnothing$  200 mm) core BOVE 97.004 at 2.00 m, was used for quantitative porosimetry investigations with the following techniques:

- Water saturation gravimetry
- Mercury injection porosimetry
- Chemical analysis porosimetry.

Macroscopical examination ensured that the inner (half) zone of the slab (i.e. around the resin injection borehole) was completely impregnated with the acrylic resin NHC-9 but the outer zone was, by contrast, not impregnated. Four  $1\text{ cm}^3$  cubes A, B, C and D, neighbouring each other, were sawn off from the non-impregnated volume of the slab. Two  $1\text{ cm}^3$  rock cubes E and F and two aliquots of 3 – 5 g rock G and H were obtained from the impregnated volume (Fig. 8.1.1). These rock cubes A – F were ground with abrasives before the porosimetry investigations. In addition, a  $1\text{ cm}^3$  reference cube was also sawn off from the non-impregnated volume and its surfaces were completely polished for comparison.

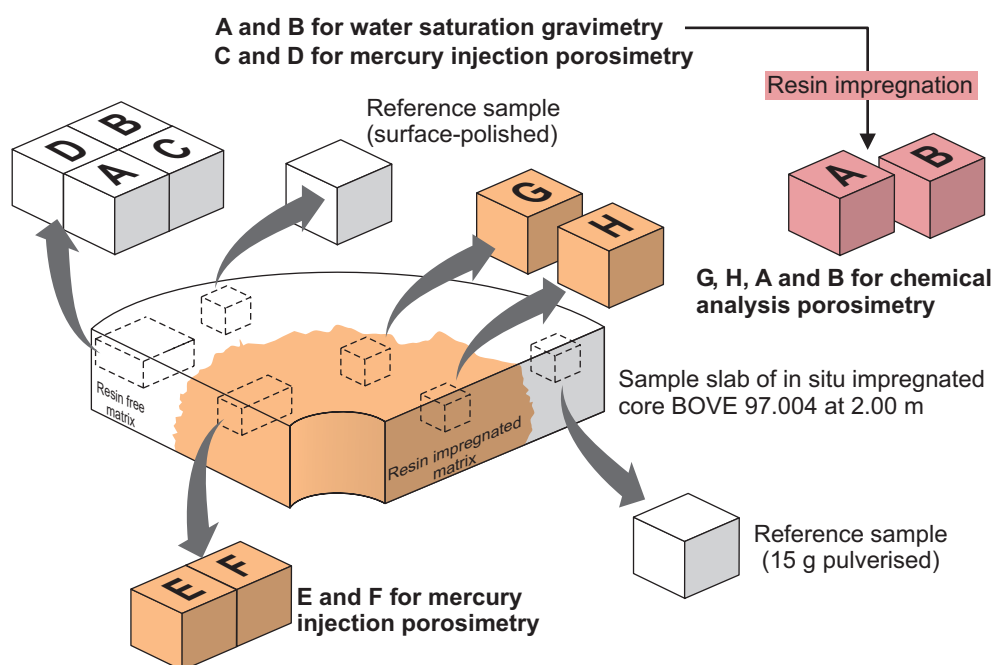


Fig. 8.1.1: Sub-samples A – H and the reference materials used for quantitative porosimetry investigations

The non-impregnated sub-samples A and B were utilised for two measurements: water saturation gravimetry and, after impregnation with resin in the laboratory, further chemical analysis porosimetry in order to check the consistency of two different techniques. The non-impregnated sub-samples C and D, the impregnated sub-sample E and F and the reference sample were used for mercury injection porosimetry. The use of both the impregnated and the non-impregnated sub-samples along with the surface-polished rock cube would allow the evaluation of sampling (overcoring, sawing, etc.) artefacts. For chemical analysis porosimetry, the sub-samples G and H (*in situ* impregnated matrix) and A and B (laboratory-impregnated matrix) were pulverised. A non-impregnated sub-sample of about 15 g was also taken and pulverised, as a reference sample, for chemical analysis porosimetry.

### 8.1.2 Water saturation gravimetry

The procedure for porosity and density determination follows basically the water saturation method proposed by FRANKLIN et al. (1979). Two sub-samples A and B were first dried in an oven at 105 °C for about 24 hours and were stored in a desiccator during cooling. The weight of dried samples was determined using a balance with an accuracy of 0.0001 g. Then the samples were immersed in de-ionised water for about 12 hours and were held under reduced pressure (below 0.01 MPa) for 12 hours, allowing them to be slowly saturated with de-ionised water. After the samples were wiped with a dry cloth, the weight of water-saturated sample was re-determined. Water temperature ( $T_1$ ) was measured simultaneously, providing water density. The volume of the sample was derived from the weight of water displaced by the sample (assuming a temperature ( $T_2$ ) corrected density). The surfaces of the water-saturated sample were dried and submerged in a volumetric flask containing a known volume of deionised water. The water displaced above a marked line on the flask was carefully extracted and weighed. Water temperature was also measured at each measurement step. Each of the measurements mentioned above was repeated at least five times (and up to forty-five times) to attain weight constancy. The connected porosity ( $\phi$ ), the bulk density ( $\rho_{bulk}$ ) and the skeletal density ( $\rho_{skeletal}$ ) of the samples can be given respectively by:

$$\Phi = \frac{V_{pore}}{V_{bulk}} \times 100 = \frac{\frac{W_{sat} - W_{dry}}{\rho_{water_1}}}{\frac{W_{water}}{\rho_{water_2}}} \times 100 \quad [\%] \quad (8.1)$$

$$\rho_{bulk} = \frac{W_{dry}}{V_{bulk}} = \frac{W_{dry}}{\frac{W_{water}}{\rho_{water_2}}} \quad [\text{kg dm}^{-3}] \quad (8.2)$$

$$\rho_{skeletal} = \frac{W_{dry}}{V_{bulk} - V_{pore}} = \frac{W_{dry}}{\frac{W_{water}}{\rho_{water_2}} - \frac{W_{sat} - W_{dry}}{\rho_{water_1}}} \quad [\text{kg dm}^{-3}] \quad (8.3)$$

where

$\phi$ :	connected porosity	[%]
$\rho_{bulk}$ :	bulk density	[kg dm <sup>-3</sup> ]
$\rho_{skeletal}$ :	skeletal density	[kg dm <sup>-3</sup> ]
$V_{pore}$ :	total water-accessible pore volume of sample	[dm <sup>3</sup> ]
$V_{bulk}$ :	bulk volume of sample	[dm <sup>3</sup> ]
$W_{dry}$ :	weight of dried sample	[kg]
$W_{sat}$ :	weight of water-saturated sample at temperature T <sub>1</sub>	[kg]
$W_{water}$ :	weight of water displaced by sample at temperature T <sub>2</sub>	[kg]
$\rho_{water\ 1,2}$ :	density of water sample at temperature T <sub>1,2</sub>	[kg dm <sup>-3</sup> ].

Analytical error (or precision, in this case) in the technique employed was statistically assessed following the measurement sequence and amounted to up to 23 % and 2 % for porosity and density determinations, respectively.

### 8.1.3 Mercury injection porosimetry

The connected porosity, pore size distribution, total pore area and density of four sub-samples C, D, E and F and the surface-polished reference sample were determined by a standard mercury injection porosimetry technique. A commercially available porosimeter was used with maximum injection pressures of about 230 MPa (for sub-samples C and D) and about 400 MPa (for sub-samples E and F). These maximum injection pressures allow mercury to intrude into only pores with equivalent (cylindrical) pore diameters over 6.4 nm and over 4.0 nm respectively. In each measurement, mercury injection pressure was stepped up and the volume of injected mercury into the sample at each step was directly monitored. The pore size distribution was then derived using the Washburn equation giving the relationship between the mercury injection pressure and the cylindrical pore diameter of mercury-injectable porosity:

$$D = - \frac{4\gamma \cos \theta}{P} \quad (8.4)$$

where

$D$ :	equivalent (cylindrical) pore diameter	[m]
$\gamma$ :	surface tension of mercury at 25 °C = 0.480	[N m <sup>-1</sup> ]
$\theta$ :	contact angle of mercury = 140	[°]
$P$ :	injection pressure of mercury	[MPa].

As these measurements yield the total intrusion volume of mercury to the sample, the connected porosity ( $\phi$ ) of the sample is derived from the total intrusion volume of mercury and the bulk volume of the sample, determined prior to mercury injection:

$$\Phi = \frac{V_{Hg}}{V_{bulk}} \times 100 = \frac{V_{Hg}}{V_{cell} - \frac{W_{Hg}}{\rho_{Hg}}} \times 100 \quad [\%] \quad (8.5)$$

where

$V_{Hg}$ :	total intrusion volume of Hg	$[\text{dm}^3 \text{ kg}^{-1}]$
$V_{bulk}$ :	bulk volume of sample	$[\text{dm}^3]$
$V_{cell}$ :	cell volume	$[\text{dm}^3]$
$W_{Hg}$ :	weight of Hg filled in cell	$[\text{kg}]$
$\rho_{Hg}$ :	density of Hg at 25 °C = 13.5335	$[\text{kg dm}^{-3}]$ .

Here the bulk density ( $\rho_{bulk}$ ) and the skeletal density ( $\rho_{skeletal}$ ) of the sample can also be calculated respectively by the following equations:

$$\rho_{bulk} = \frac{W_{dry}}{V_{bulk}} \quad [\text{kg dm}^{-3}] \quad (8.6)$$

$$\rho_{skeletal} = \frac{W_{dry}}{V_{bulk} - V_{Hg}} \quad [\text{kg dm}^{-3}] \quad (8.7)$$

where

$W_{dry}$ :	weight of dried sample	$[\text{kg}]$ .
-------------	------------------------	-----------------

Analytical error (or precision, in this case) in this mercury injection porosimetry technique employed is small and amounts to below 1.5 % for all measurements<sup>17</sup>.

#### 8.1.4 Chemical analysis porosimetry

Following *in situ* resin impregnation, the connected porosity of the rock matrix was determined by directly quantifying the resin content of the sub-sample using a novel analytical technique. Specifically, since the acrylic resin NHC-9 employed *in situ* contains carbon as a major constituent element but the rock matrix is, by contrast, originally poor in carbon, the resin-derived carbon content of the impregnated sample was determined.

To prepare standard materials for a calibration curve, a known amount of the resin powder was first homogeneously mixed with the pulverised reference sample. Standard additions of 0.1, 0.5 and 1.0 wt% of resin were made to obtain a linear relationship between the amount of resin and the resin-derived carbon content. After sample preparation and treatment, carbon analysis was carried out on 100 – 400 mg aliquots of the reference sample (with no added resin), on the standard materials and on the impregnated sub-samples G and H by the technique of thermal conductivity gas analysis, using a specialised NCH analyser, following the oxygen-enriched combustion of the sample at 850 °C. Each analysis was triplicated. The calibration curve within a 1 $\sigma$  deviation, obtained by a least squares fit, gives the weight fraction of the resin-derived carbon content in impregnated samples, corresponding to the resin content. The connected porosity ( $\phi$ ) of the *in situ* impregnated matrix can be calculated by converting weight fraction into volume fraction:

<sup>17</sup> Note that the application of mercury injection porosimetry is rock type dependent and so other aspects may need to be considered in other cases (see, for example, the comments in HELLMUTH et al. 1995).

$$\Phi = \frac{V_{resin}}{V_{bulk}} \times 100 = \frac{\frac{W_{resin}}{\rho_{resin}}}{\frac{W_{resin}}{\rho_{resin}} + \frac{(1 - W_{resin})}{\rho_{skeletal}}} \times 100 \quad [\%] \quad (8.8)$$

where

$V_{resin}$ :	total intrusion volume of resin	$[\text{dm}^3 \text{ kg}^{-1}]$
$V_{bulk}$ :	bulk volume of sample	$[\text{dm}^3]$
$W_{resin}$ :	weight fraction of resin per 1 kg sample	$[\text{kg}]$
$\rho_{resin}$ :	density of resin at 20 °C = 1.118	$[\text{kg dm}^{-3}]$
$\rho_{skeletal}$ :	skeletal density of sample	$[\text{kg dm}^{-3}]$ .

Here the skeletal density of the sample ( $\rho_{skeletal}$ ) was given by both water saturation gravimetry and mercury injection porosimetry as described before. This technique was also applied to the samples A and B, impregnated with different acrylic resin in the laboratory following the porosity measurements by water saturation gravimetry. The density of polymerised NHC-9 resin was found to be  $1.118 \pm 0.034 \text{ kg dm}^{-3}$  and is slightly higher than that of the liquid NHC-9 ( $1.070 \text{ kg dm}^{-3}$  reported by SIKA AG). This difference in density indicates that very minor shrinkage<sup>18</sup> actually occurred and that about 4 % of volume was lost during polymerisation. However, this small volume change does not affect the calculations of the chemical analysis porosimetry because the liquid density was used to convert the resin-derived carbon content into volume fraction.

Error propagation in this analytical technique was statistically assessed following the analytical sequence. Although the analytical error (or precision, in this case) itself is generally small, it may be estimated to be up to 8 % due to effects associated with data treatment. Although this is a well-established technique, the application in this case is rather novel. It is therefore recommended that further method development be carried out in future to assess potential artefacts (e.g. optimum combustion times or effects of grain size). However, the good agreement with porosity values determined with water-saturation gravimetry on the same rock samples (see Tab. 8.2.1) is very encouraging and suggests that this technique is probably applicable to rock samples.

## 8.2 Results and discussion

A total of 10 porosimetry measurements were conducted on *in situ* impregnated, laboratory-impregnated and non-impregnated sub-samples A – H obtained from the Grimsel granodiorite matrix. The results of the measurements are listed in Tab. 8.2.1.

---

<sup>18</sup> Unlike some of the cases reported in ALEXANDER et al. (2001), no shrinkage damage was observed in the samples investigated here.

Tab. 8.2.1: Porosimetry data for the Grimsel granodiorite matrix, obtained through quantitative investigations; analytical errors listed were assessed for each technique as described in the preceding sections

Method	Sub-samples		Connected Porosity [%]			Bulk Density [kg dm <sup>-3</sup> ]		Skeletal Density [kg dm <sup>-3</sup> ]	
		No.	Def.		Average		Average		Average
Water Saturation Gravimetry	laboratory-prepared	A	a + b	0.66 ± 0.08	0.72 ± 0.13 <sup>1</sup>	2.65 ± 0.07	2.65 ± 0.05	2.67 ± 0.07	2.67 ± 0.05
		B		0.77 ± 0.17		2.65 ± 0.02		2.67 ± 0.03	
Mercury Injection Porosimetry	laboratory-prepared	C	a + b	0.69 ± 0.01	0.61 ± 0.01 <sup>2</sup>	2.64 ± 0.00	2.64 ± 0.00	2.66 ± 0.00	2.66 ± 0.00
		D		0.53 ± 0.01		2.64 ± 0.00		2.66 ± 0.00	
Chemical Analysis Porosimetry	laboratory-impregnated	A	a + b	0.68 ± 0.01	0.74 ± 0.01	nd	nd	nd	nd
		B		0.80 ± 0.01					
Mercury Injection Porosimetry	<i>in situ</i> impregnated	E	b	0.39 ± 0.01	0.40 ± 0.01	nd	nd	nd	nd
				0.41 ± 0.01					
Chemical Analysis Porosimetry	<i>in situ</i> impregnated	F	a	0.21 ± 0.02	0.27 ± 0.02	nd	nd	nd	nd
		G		0.33 ± 0.01					

<sup>1</sup> This is comparable with existing data for water saturation gravimetry in Grimsel granodiorite (range 0.67 – 0.85 %, average 0.76 %; see Table 4 in BOSSART et al. 1991)

<sup>2</sup> This is comparable with existing data for mercury injection porosimetry in Grimsel granodiorite (range 0.52 – 1.53 %, average 0.93 %; see Table 3 in BOSSART et al. 1991)

a: *in situ*; b: artificial

nd: not determined

### 8.2.1 Comparison of connected porosities determined on laboratory samples

A comparison of the results of porosimetric measurements using three different techniques (water saturation gravimetry, mercury injection porosimetry and chemical analysis porosimetry) shows a generally good agreement (Tab. 8.2.1). In particular, there is a very good agreement between values for the connected porosities determined on the same sub-samples A and B by both water saturation gravimetry and chemical analysis porosimetry (and with existing data for non-impregnated samples from BOSSART et al. 1991).

It is however shown that the mercury injection porosimetry yields slightly lower porosity values than those derived from other measurements. Since the sub-samples A – D, each of about 1 cm<sup>3</sup>, neighbouring each other (Fig. 8.1.1), were taken from the rock matrix in as similar a manner as practicable, the geometrical and physical properties of the samples may be similar, but not identical. There is actually a very good agreement, between values for the bulk and skeletal densities respectively, measured on these sub-samples. A discrepancy between the measured connected porosities is attributed possibly to the presence of pores that were not intruded by mercury. Mercury can be intruded only into pores with an equivalent diameter over 6.4 nm (when using maximum injection pressure of 230 MPa) whereas the acrylic resin employed in



the laboratory is presumed to be injected deeper into very fine pores down to about 2 nm in size because of its very small molecular size (maximum 1.5 nm) and very low viscosity and surface tension (see ALEXANDER et al. 2001 for details).

### 8.2.2 Connected porosity and pore-size distribution of laboratory samples

Taking account of the sampling limitations, the agreement provides a convincing demonstration of the consistency of the porosimetric measurement techniques. The laboratory-prepared samples A – D have connected porosities between 0.53 and 0.80 vol% (Tab. 8.2.1; mean value of 0.69 vol%), irrespective of the technique applied, which is consistent with mercury injection porosimetry data (0.67 – 1.53 vol%) previously reported for non-impregnated, undeformed Grimsel granodiorites (BOSSART & MAZUREK 1991). The size distribution of pores in the laboratory samples can be represented as that of mercury injectable porosity. The laboratory-prepared samples give the maximum relative abundance of pore sizes around 0.4  $\mu\text{m}$  and are also abundant in larger pores with equivalent diameters over 10  $\mu\text{m}$  (Fig. 8.2.1).

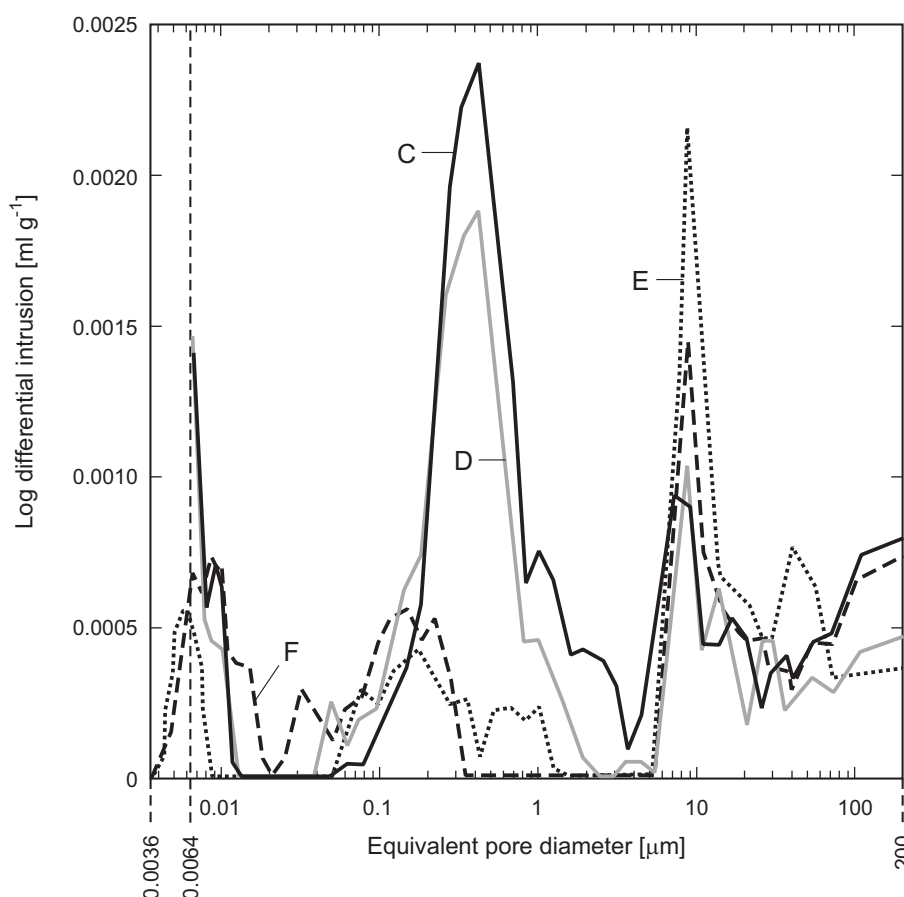


Fig. 8.2.1: Size distribution of mercury injectable porosity in the Grimsel granodiorite

Vertical axis corresponds to the relative abundance of pore size. C and D: non-impregnated samples, E and F: *in situ* impregnated samples.

### 8.2.3 Comparison of connected porosities for *in situ* and laboratory samples

Connected porosities, determined on the *in situ* impregnated samples G and H by chemical analysis porosimetry, have an average value of 0.27 vol%, which is 2 to 3 times lower than those measured on the laboratory-prepared samples (Tab. 8.2.1). Since the acrylic resin NHC-9 used *in situ* is similar in physical properties to the acrylic resin employed in the laboratory (i.e. very low viscosity and surface tension and, presumably, very small molecular size of about a few nm), it can penetrate fully into accessible pores greater than a few nm in size, which exist *in situ*.

It is of note that the architecture of the interconnected matrix porosity identified in the *in situ* impregnated samples is found to be similar, but not identical, to that observed in the laboratory-impregnated samples and this is presumably responsible for the disagreement between the values for the measured connected porosities.

The *in situ* impregnated sample E and F were further impregnated with mercury in the laboratory, producing mercury-injectable porosities of 0.39 and 0.41 vol% respectively (Tab. 8.2.1; average value of 0.40 vol%). If it is assumed that accessible matrix porosity *in situ* must be fully impregnated with the acrylic resin (as discussed above), this 'extra' porosity is an obvious indication of the extent of distressing and damage induced in the rock during sampling. Clearly, this fact supports the thesis that the geometry and structures of matrix porosity in the laboratory-impregnated samples are no longer identical to those in the undisturbed *in situ* rock matrix. In addition, the value of 0.40 vol% for the 'extra' is consistent with the difference between values for the connected porosities, determined on the *in situ* impregnated samples G and H (0.21 and 0.33 vol% respectively) and the laboratory-impregnated samples A – D (0.53 – 0.80 vol%). Combined with the observations on the differences in pore geometry between *in situ* impregnated and laboratory-prepared samples, this strongly suggests that the higher connected porosities given in the laboratory-prepared samples are due to the complex effects of the alteration of the existing matrix porosity and the creation of new types of pores, which were, most likely, induced by artefacts of stress release and sample preparation. Fig. 8.2.1 shows the size distribution of the 'extra' pores (in samples D and F), which gives the maximum relative abundance of pore sizes around 8  $\mu\text{m}$  and higher abundance of larger pores with equivalent diameters over 15  $\mu\text{m}$  (i.e. macroporosity).

A comparison of the pore size distribution curves in Fig. 8.2.1 shows that larger pores, with diameters over several  $\mu\text{m}$ , observed in all the laboratory-prepared samples are certainly sampling artefacts. Specifically, the macroporosity is most likely influenced by artefacts on the sample surfaces. This is supported by pore size distribution data produced on both the surface-ground and -polished samples: the abundance of macropores in the surface-ground samples C and D is quite high in comparison with that in the surface-polished reference sample (Fig. 8.2.2). Although the effects of the sample surface artefacts on the measured porosity can be excluded, other potential artefacts should be specified and the degree of change induced by such effects should be quantified. In this respect, it is necessary to carry out additional investigations such as a comparison of mercury injection porosimetry curves from laboratory and *in situ* impregnated samples.

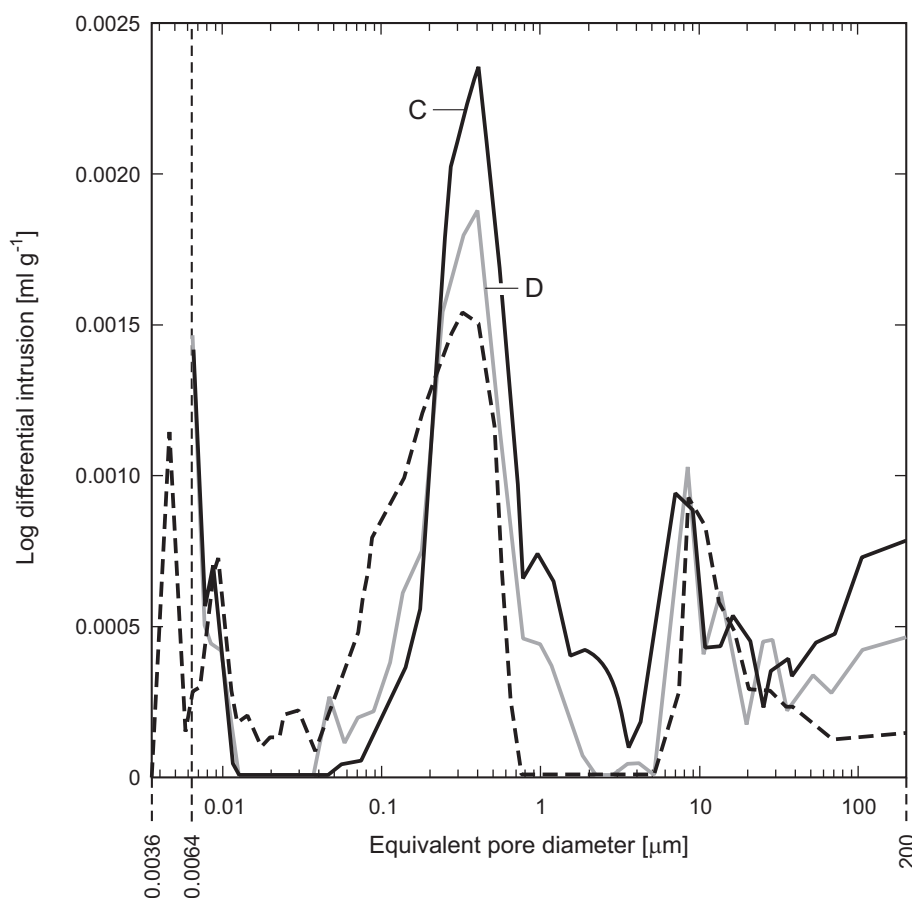


Fig. 8.2.2: Size distribution of mercury injectable porosity in the surface-ground samples and the surface-polished reference sample

Vertical axis corresponds to the relative abundance of pore size. Curves: surface-ground samples (sub-samples C and D), dashed curve: surface-polished sample.

#### 8.2.4 *In situ* connected porosity and pore-size distribution

Differences in the pore size distribution between the laboratory-prepared sample, in which both *in situ* and 'extra' porosities exist, and the *in situ* impregnated sample that has only the 'extra' porosity are attributed to the distribution of the *in situ* porosity. Fig. 8.2.3 shows the size distribution of the *in situ* porosity, which was estimated based upon the differences between both sample sets. The undisturbed *in situ* rock matrix, in comparison, has pores with diameters below 20 nm and between 0.1 μm and up to 10 μm with the maximum relative abundance of pore sizes around 0.4 μm.

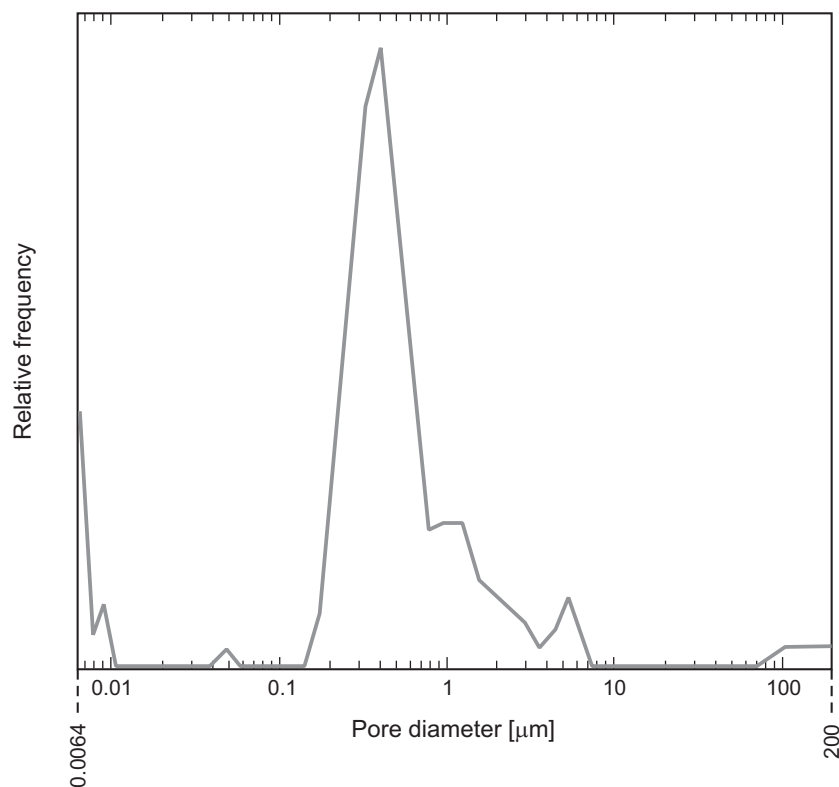


Fig. 8.2.3: Estimated size distribution of *in situ* porosity in the Grimsel granodiorite matrix

Calculation based upon results from mercury injection porosimetry on sub-samples C, D, E and F.

### 8.3 Conclusions

Although this work has been conducted on a limited number of samples, it seems likely that connected porosity values measured by standard laboratory techniques are too high. Here, up to 50 % of the porosity value measured on laboratory-prepared samples is probably an artefact of stress release and sample preparation. This will clearly influence subsequent laboratory parameter evaluations based on matrix porosity (e.g. diffusion coefficients) and should therefore be considered when assessing the likely retardation capacity of a repository host rock using calculations based purely on laboratory-derived data (see Chapter 9).

## 9 ILLUSTRATING THE EFFECTS OF THE MAGNITUDE AND EXTENT OF CONNECTED MATRIX POROSITY ON RADIONUCLIDE TRANSPORT IN A FRACTURED GEOLOGICAL MEDIUM

*P.A. Smith*

### 9.1 Introduction

The purpose of this chapter is to illustrate the effects of the assumed magnitude and extent of connected matrix porosity on radionuclide transport in fractured geological media as calculated in performance assessment (PA) geosphere transport models. Here, the particular model is that used to analyse the Reference Case in the Nagra Kristallin-1 (or K-1) PA (NAGRA 1994), with alternative datasets based on both the K-1 and JNC Second Progress Report (or J-2) PA (JNC 2000) Reference Cases. Since the purpose is to illustrate the sensitivity to geosphere parameters related to the matrix porosity, the differences between the J-2 and K-1 near-field models and data are not considered here (see, rather, NEALL 2001, for details). Releases from the near-field for all calculations here are carried out with the K-1 Reference Case model and data so that, in effect the repository considered in K-1 is assumed for all calculational cases, irrespective of whether the geosphere data are based on K-1 or J-2.

### 9.2 Model representation of the geosphere

The geosphere model is illustrated in Fig. 9.2.1 and shows an area,  $A$ , in a planar section through the host rock normal to the assumed direction of groundwater flow. The groundwater, containing radionuclides released from the near-field to the geosphere, is assumed to flow through discrete channels, also shown schematically in the figure.

In the geosphere transport model used in the present study (and used to analyse the Reference Case in K-1), it is assumed that all channels are identical and are described by the following parameters:

- the solid density of the matrix,  $\rho$  [ $\text{kg m}^{-3}$ ],
- the channel aperture,  $2b$  [m],
- the hydraulic gradient,  $i$ ,
- the transmissivities of the channels,  $T$  [ $\text{m}^2 \text{a}^{-1}$ ],
- the length of the channels,  $L$  [m],
- the depth of the diffusion-accessible matrix, measured from the centre of a channel,  $y_p$  [m],
- the matrix porosity,  $\varepsilon$ ,
- the pore diffusion coefficient of the matrix,  $D_p$  [ $\text{m}^2 \text{a}^{-1}$ ],
- the Peclet number describing longitudinal dispersion,  $Pe$ ,
- the nuclide-dependent sorption (or distribution) constants describing sorption on matrix pore surfaces,  $K_d$  [ $\text{m}^3 \text{kg}^{-1}$ ],
- the channel width,  $g_i$  [m].

The total number of channels and the specific widths of individual channels within the plane are not relevant to the geosphere transport model. The total flow at the near-field/geosphere

interface ( $Q$  [ $\text{m}^3 \text{a}^{-1}$ ]), a parameter of the near-field model, is, however, proportional to the summed widths of channels in the area  $A$ :

$$Q = Ti \sum_{\text{channels in area A}} g_i \quad (9.1)$$

In the K-1 Reference Case, and in all the following calculations, it is assumed that  $Q = 3 \text{ m}^3 \text{a}^{-1}$ .

### 9.3 Parameter values

Geosphere parameter sets based on the Reference Cases of K-1 and J-2, as well as variations on these to illustrate the effects of the magnitude and extent of connected matrix porosity and the magnitude of the pore diffusion coefficient, are given in Tab. 9.3.1 and 9.3.2. For simplicity, cases based on J-2 consider only the undisturbed host rock. Transport through a fault zone, which was included in the J-2 Reference Case, is not considered in the present study.

Cases K-1-1 and J-2-1 are based on the K-1 and J-2 Reference Cases, respectively. Cases K-1-2 and J-2-2 illustrate the effects of reduced matrix porosity. Cases K-1-3 and J-2-3 illustrate the effects of increased matrix porosity. Cases K-1-4 and J-2-4 illustrate the effects of reducing the depth of diffusion-accessible matrix from the centre of the channels whereas cases K-1-5 and J-2-5 illustrate the effects of increasing the depth of diffusion-accessible matrix. Finally, cases K-1-6 and J-2-6 illustrate the effects of a reduced pore diffusion coefficient in the matrix.

The radionuclides considered are the fission products  $^{79}\text{Se}$ ,  $^{135}\text{Cs}$  and  $^{99}\text{Tc}$  which, in K-1, dominated the calculated doses at times up to about 2 Ma after repository closure.  $^{237}\text{Np}$  is also considered as an example of a long-lived actinide as, in K-1, the actinide chains dominated the calculated doses at times beyond about 2 Ma (see NAGRA 1994, for details).

Considering Tab. 9.3.1 and 9.3.2, the most significant differences in the geosphere data for all cases are the lower channel transmissivity and lower fracture aperture used in the cases based on J-2 data. While fracture aperture is known to be an insensitive parameter (as discussed in NAGRA 1994 and JNC 2000), the calculated results clearly show that the lower channel transmissivity for the J-2 cases gives rise to longer transport times, more time for radioactive decay, and lower geosphere releases when compared to the K-1 cases.

### 9.4 Results

The effects of varying the main geosphere parameters on radionuclide reatrdation in the geosphere can be represented graphically by comparing the time dependent release of radionuclides from the geosphere to the biosphere (the so-called 'geosphere release') to that of the time dependent release of radionuclides from the engineered barriers in the repository (the so-called 'near-field release'). The comparison of geosphere and near-field releases for all J-2 and K-1 cases are shown in the upper and lower parts of Fig. 9.4.1 ( $^{79}\text{Se}$ ) and 9.4.2 ( $^{135}\text{Cs}$ ). Fig. 9.4.3 shows the geosphere releases of  $^{99}\text{Tc}$  and  $^{237}\text{Np}$  for all K-1 cases only as all J-2 cases were too small to calculate reliably and consequently are not shown graphically<sup>19</sup>.

<sup>19</sup> Note that this differs from the J-2 PA results (see JNC 2000) because a different geosphere model was used that considered a distribution of channel transmissivities, rather than the single, geometric mean value used here and this gives rise to higher calculated geosphere releases.

Tab. 9.3.1: Nuclide-independent geosphere parameters

Parameter	Cases based on K-1 <sup>1</sup>						Cases based on J-2 <sup>2</sup>					
	K-1-1	K-1-2	K-1-3	K-1-4	K-1-5	K-1-6	J-2-1	J-2-2	J-2-3	J-2-4	J-2-5	J-2-6
$\rho$ [kg m <sup>-3</sup> ]	2600						2700					
$b$ [m]	$5 \times 10^{-4}$						$10^{-5}$					
$i$	0.04						0.01					
$T$ [m <sup>2</sup> a <sup>-1</sup> ]	0.275						0.0065					
$L$ [m]	200						100					
$D_p^3$ [m <sup>2</sup> a <sup>-1</sup> ]	0.001					$10^{-4}$	0.0047					0.00047
$Pe$	10						10					
$\varepsilon$	0.05	0.01	0.20	0.05			0.02	0.005	0.1	0.02		
$y_p$ [m]	0.05			0.01	0.20	0.05	0.1			0.05	0.5	0.1

<sup>1</sup> Values based on Table 5.3.4 of NAGRA (1994).

<sup>2</sup> Values based on undisturbed host rock, Table 5.3.2-3 in JNC (2000). Channel transmissivity is taken to be the geometric mean transmissivity of a fracture ( $T_m = 10^{-9.99}$  m<sup>2</sup> s<sup>-1</sup>), multiplied by a factor of 2 to account for channelling within the fracture. In J-2,  $b = \sqrt{T_m}$ .

<sup>3</sup> See also footnote 16 on the treatment of tortuosity variations within  $D_p$ .

Tab. 9.3.2: Nuclide-dependent geosphere parameters

Nuclide	Half life [a]	$K_d$ for cases based on K-1 [m <sup>3</sup> kg <sup>-1</sup> ] <sup>2</sup>	$K_d$ for cases based on J-2 [m <sup>3</sup> kg <sup>-1</sup> ] <sup>3</sup>
<sup>79</sup> Se	$1.1 \times 10^6$ <sup>1</sup>	0.01	0.01
<sup>135</sup> Cs	$2.3 \times 10^6$	0.042 <sup>4</sup>	0.05
<sup>99</sup> Tc	$2.1 \times 10^5$	0.5	1
<sup>237</sup> Np	$2.1 \times 10^6$	1	1

<sup>1</sup> The value used in K-1 and J-2 was  $6.5 \times 10^4$ . This value has been revised since these assessments were carried out<sup>20</sup>.

<sup>2</sup> Values taken from Table 3.7.8 of Nagra (1994), "Realistic-conservative" values, Area West.

<sup>3</sup> Values taken from Table 5.3.2-2 of JNC (2000).

<sup>4</sup> Calculated from derived Freundlich isotherm (subsection 5.3.3.2 of NAGRA 1994).

<sup>20</sup> New value is based on the ENSDF data which can be viewed directly at the Brookhaven National Laboratory web site: <http://www.nndc.bnl.gov/nndc/ensdf/#001>.

## 9.5 Discussion

Fig. 9.4.1 to 9.4.3 show that, for all the radionuclides considered, varying the absolute value of the matrix porosity makes very little difference to calculated radionuclide retardation in the geosphere. Although in some cases (especially K-1-2 for  $^{99}\text{Tc}$ ) a low matrix porosity or a low pore diffusion coefficient give rise to earlier calculated geosphere releases, the peak release concentration is only slightly higher than for the Reference Case.

The figures show, however, that the depth of diffusion accessible matrix is a more sensitive parameter. Assuming a reduced matrix depth gives rise to both earlier and higher geosphere releases whereas an increased depth, while producing little temporal change in the release pattern, significantly decreases the peak release concentration (see Fig. 9.4.3, for example).

## 9.6 Conclusions

Over the ranges considered here, variations in the precise value of the matrix porosity and of matrix pore diffusion coefficient on calculated radionuclide retardation are small, rather it is the distance that this porosity extends into the rock that is the more important parameter.

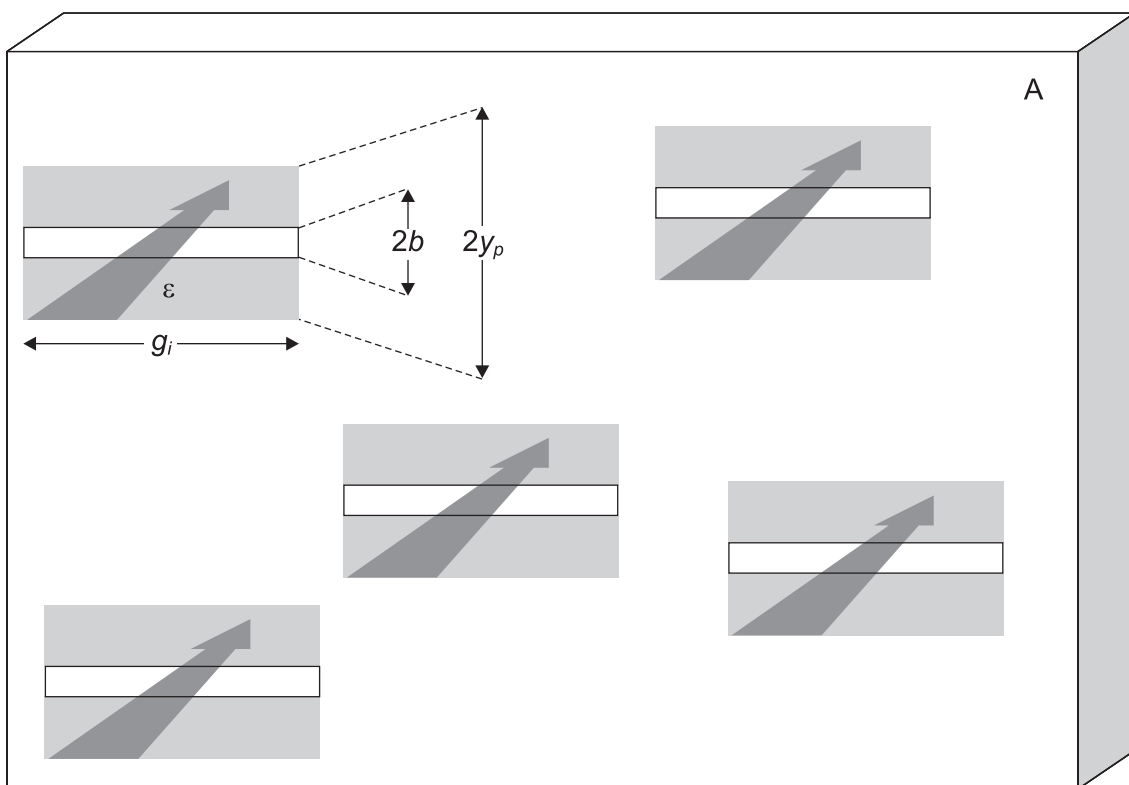


Fig. 9.2.1: Schematic illustration of the geosphere model, showing an area  $A$  in a planar section through the host rock normal to the direction of groundwater flow and channels passing through the plane that convey the groundwater (large arrows); matrix diffusion is assumed to occur within the shaded regions adjacent to the channels



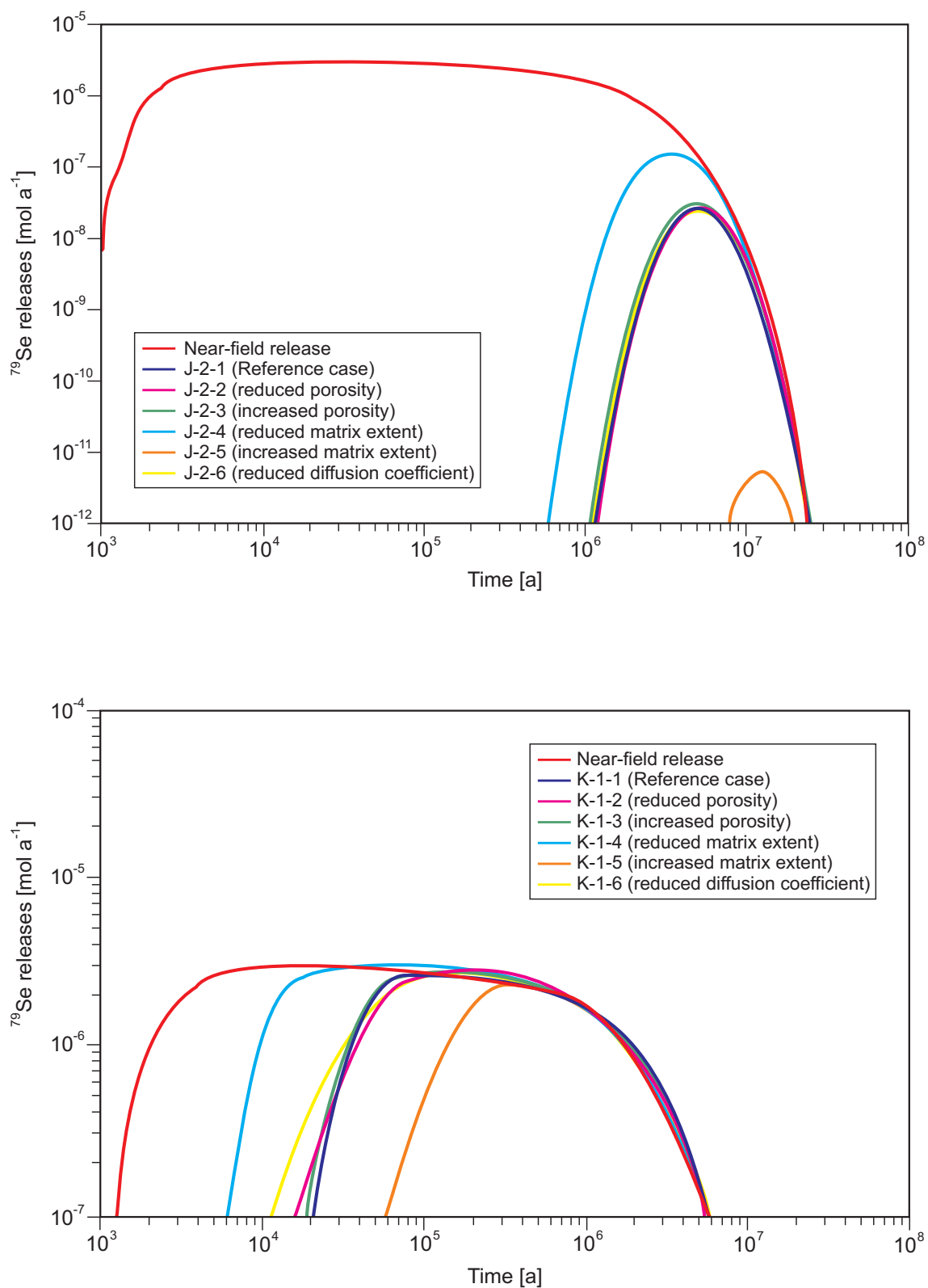


Fig. 9.4.1: The geosphere releases of  $^{79}\text{Se}$  for the cases J-2-1 to 6 (upper figure) and K-1-1 to 6 (lower figure), compared to the near-field release of this radionuclide

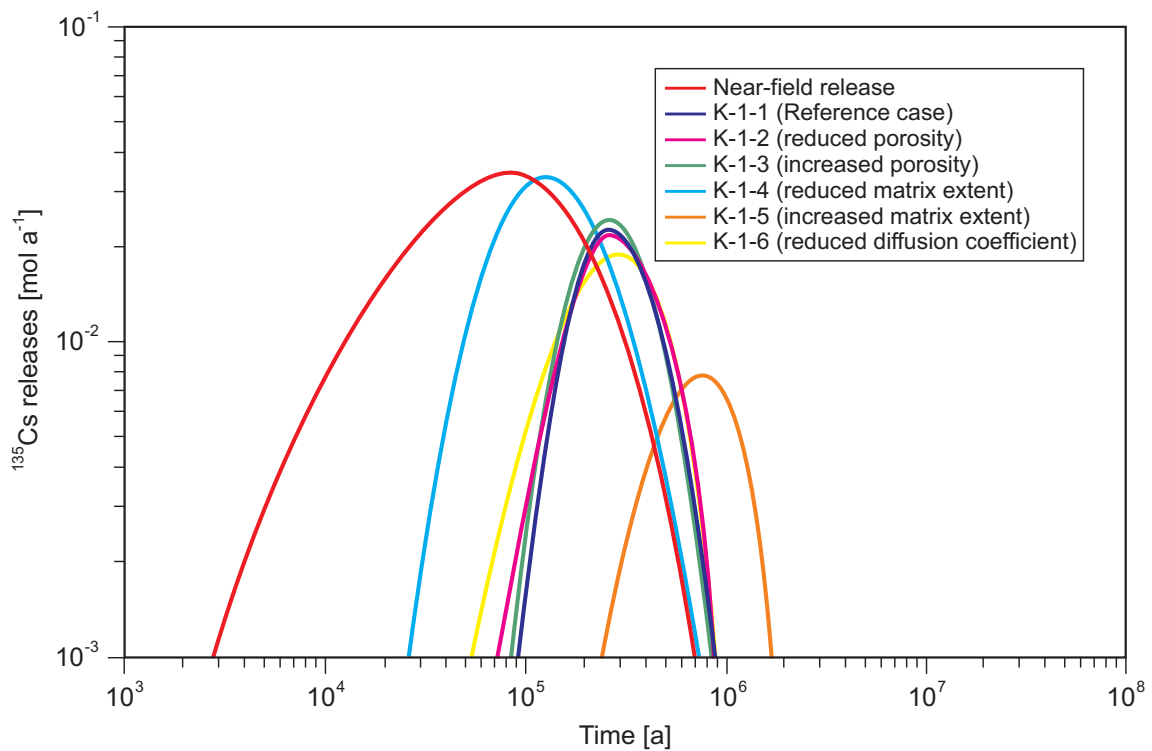
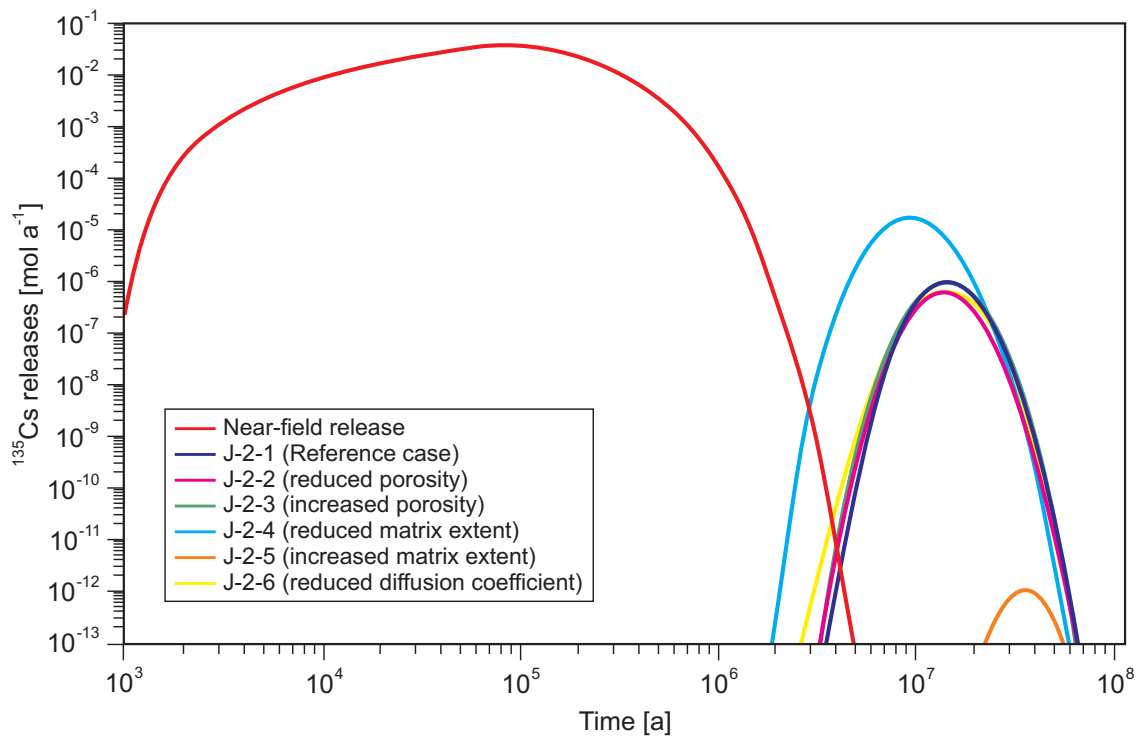


Fig. 9.4.2: The geosphere releases of  $^{135}\text{Cs}$  for the cases J-2-1 to 6 (upper figure) and K-1-1 to K-1-6 (lower figure), compared to the near-field release of this radionuclide

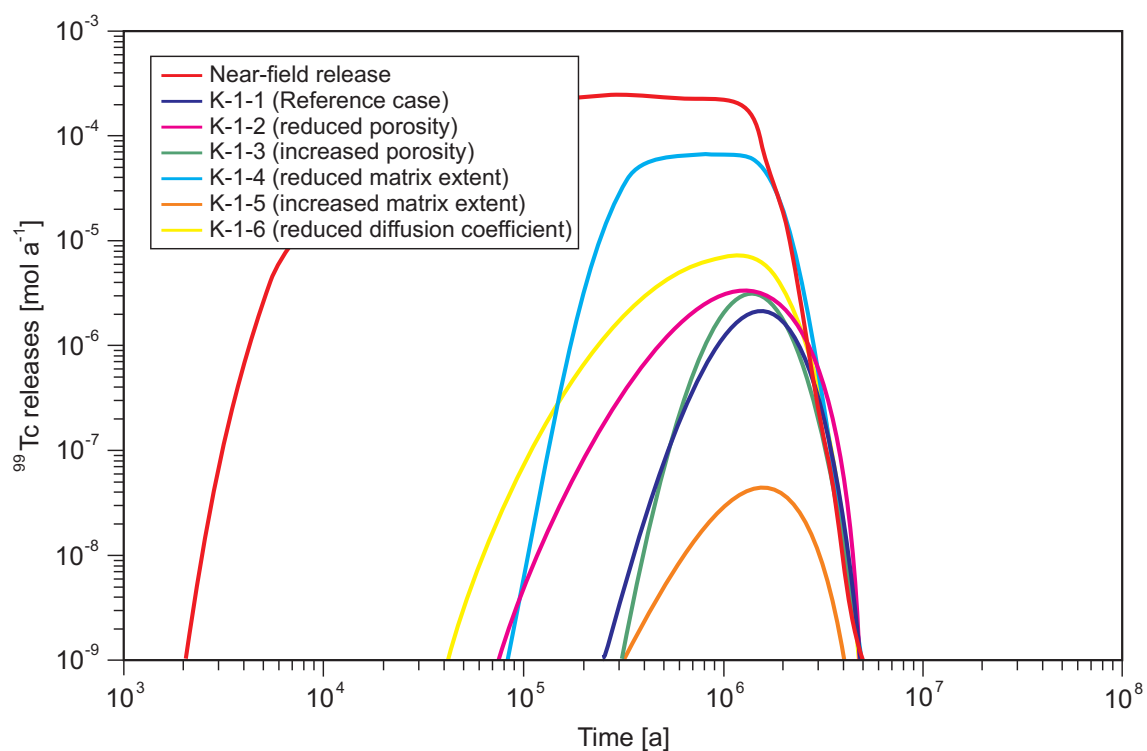
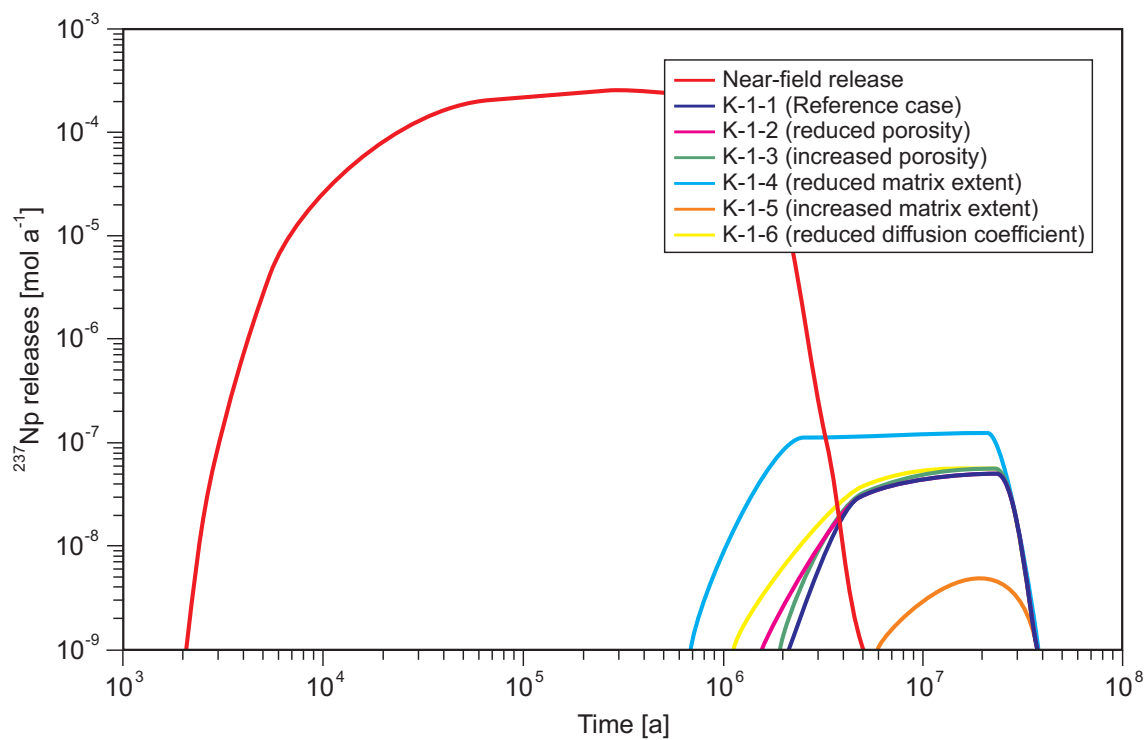


Fig. 9.4.3: The geosphere releases of  $^{237}\text{Np}$  (upper figure) and  $^{99}\text{Tc}$  (lower figure) for the cases K-1-1 to K-1-6, compared to the near-field releases of these radionuclides



## 10 CONCLUSIONS

*W.R. Alexander, A. Möri and K.Ota*

The present study has demonstrated that, by combining microfabric analyses, petrophysical investigations and *in situ* field observations, a quantitative evaluation of the matrix porosity can be obtained and this represents an important step towards the more realistic representation of *in situ* matrix properties in contaminant transport codes. In this project, a suitable resin formulation has been developed to impregnate undisturbed crystalline matrix rock *in situ*. The low viscosity acrylic resin that was developed provides adequate penetration at low pressures, which ensures minimal disruption of fine pore structures. Hardening is sufficient to allow overcoring and preparation of standard petrographic thin sections and other samples for subsequent analysis. Eosine as fluorescent agent in the resin was found to be appropriate for pore space impregnation.

The macroscopic distribution of pore space in the matrix was found to strongly depend on the mineralogical and structural composition. The shape of the impregnated area (observed on the surfaces of slabs cut from rock cores) indicated a mean resin impregnation depth of about 6 cm perpendicular to the injection borehole<sup>21</sup>, with a preferred matrix penetration direction parallel to the stretching lineation.

A borehole disturbed zone (BDZ) in the matrix around the injection boreholes was also identified. The BDZ is characterised by a relatively high density of pore space around boundaries of mineral grains and by open microfractures extending sub-parallel to the borehole axis. The extent of the BDZ into the rock matrix normal to the borehole axis is 3 to 4 cm.

Most intensive impregnation, indicating highest porosities, occurs in rock portions where initial ductile deformation subsequently underwent brittle reactivation, locally producing open fractures. Such structures are rare in the undisturbed matrix but become more abundant in the vicinity of shear zones. Several pore types have been distinguished microscopically:

- the majority are associated with mineralogical, structural or textural features of the rock such as grain boundary pores bordering mainly quartz and feldspar grains,
- sheet silicate pores, which are mainly bound to shear bands consisting of muscovite, biotite and chlorite and which are mainly orientated parallel to the (001)-cleavage planes
- microfractures which were observed as fine cracks within larger quartz and feldspar grains but also cross-cutting several mineral grains disregarding any textural or structural feature within the rock
- solution pores were defined as diffuse, cloudy impregnated sections of altered and exsolved feldspar, epidote and mica grains.

Since all of the different pore types distinguished in the matrix of both the Grimsel and Kurihashi granodiorites (see OTA et al. 2003) can be filled with acrylic resin, it can be assumed that they build an interconnected and permeable network and are, therefore, readily accessible to contaminants diffusing into the matrix from associated water-conducting features. The orientation and relative frequency of individual pore sets strongly depends on the fabric and texture of the related host minerals since microfractures and grain boundary pores predominate. The most significant fabric change from the wall rocks towards the centre of the shear zone is an increase of the intensity of the planar fabric which is best reflected by the orientation pattern of the

---

<sup>21</sup> *c.f.* penetration depth of 2 – 8 cm for the *in situ* diffusion of iodide from boreholes in VILKS et al. (2001).

(001)-cleavage planes. It can be assumed that the connectivity of the corresponding microfractures increases in the same direction. As a consequence, within the shear zone a channelled fluid flow through microfractures parallel to the foliation has to be expected.

A 3-D model of pore space distribution within the matrix revealed a constrictive and/or tortuous geometry of the matrix porosity caused by resin accessible pore spaces ("microchannels") and non-accessible spaces ("barriers") with pore dimensions of less than 1  $\mu\text{m}$ .

The diffusion accessible rock volume, described as connected/resin impregnated porosity, was determined by different techniques and the results were in good agreement: buoyancy weighting, water saturation gravimetry, mercury injection porosimetry and chemical analysis porosimetry. Buoyancy weighting on samples previously resin impregnated *in situ*, revealed porosities of about 0.6 vol%. Assuming that all accessible *in situ* porosity was already filled by resin, this additional (or residual) porosity can be assumed to be an indication of drilling / sub-sampling damage. The subtraction of this residual porosity from porosities derived from non-impregnated laboratory samples resulted in an *in situ* porosity of 0.4 to 0.5 vol%, or a third to a half of the porosity that is measured on conventionally sampled (i.e. non-impregnated) rock specimens in the laboratory. The results from water saturation gravimetry, mercury injection porosimetry and chemical analysis porosimetry on non-impregnated samples revealed porosity values of between 0.53 and 0.80 vol% (comparable to existing data for the Grimsel granodiorite). Mercury injection porosimetry and chemical analysis porosimetry on *in situ* impregnated samples revealed porosity values between 0.27 and 0.39 vol%, strongly suggesting that more than half of the connected porosity determined by standard laboratory measurements is an artefact of stress release and sample preparation.

However, the significance of this result should not be overstressed as the number of samples analysed to date using this methodology are not statistically significant. Nevertheless, the support of independent data can increase confidence in these new data and, here, this is provided by the results of the universal stage analyses.

Measurements of matrix permeability assuming a confining pressure of 20 MPa (which closely approximates the *in situ* conditions at both sites) revealed a hydraulic conductivity of between  $1.00 \times 10^{-12} \text{ m s}^{-1}$  and  $7.12 \times 10^{-13} \text{ m s}^{-1}$ . The anisotropy of the permeability/hydraulic conductivity was strongly related to the rock foliation, the smallest values were usually present normal to the foliation. From measured microfracture data, it was obvious that mainly the (001) cleavage microfractures in mica, plus microfractures in feldspars and quartz control the directional dependence of the hydraulic properties. This is also the case at higher confining pressures.

For both *in situ* impregnated and non-impregnated samples, a strong geometric relationship between the  $\Delta Vp$  stereograms and the pole figures under dry, water-saturated conditions and higher confining pressures indicated that the multi-directional  $Vp$  anisotropy was mainly caused by the observed and quantified pore fabrics. In fact, the  $\Delta Vp$  values between impregnated and non-impregnated samples reflect the bulk microfracture patterns which effectively influence the  $Vp$  anisotropy at lower confining pressure (below 20 MPa). An influence, especially on the microfractures in mica, connected microfractures in quartz and those in feldspar, could be recognised in the  $\Delta Vp$  stereogram, too. These pore sets which were mainly oriented parallel to the foliation produced a marked open connected porosity also under *in situ* conditions (*cf* the results of the 3-D pore space reconstruction discussed above). Moreover, the direct comparison of  $Vp$  between dry and saturated conditions allowed a quantitative comparison between open *in situ* pores and those effects produced by stress release after core extraction and sample treatment. This revealed an *in situ* porosity of about 0.5 %, in agreement with the upper limit of the different porosity measurements discussed above.

However, variations in the precise value of the matrix porosity and of the matrix pore diffusion coefficient (and, therefore on tortuosity and constrictivity<sup>22</sup>) on calculated radionuclide retardation in a repository host rock are small. Of much more significance is the distance that this porosity extends into the rock behind the water conducting features. Although the resin injected *in situ* penetrated only 6 – 8 cm away from the boreholes into the rock matrix, of much more importance is the simple fact that the matrix around the injection boreholes (and outwith the BDZ) could be successfully impregnated with resin at all. This clearly indicates the existence of an interconnected system of different pore types and it can be reasonably assumed that this pore space is accessible to contaminants migrating through a repository host rock. Furthermore, it should be remembered that the borehole layout was set-up such that there is a continuous profile through matrix rock on both sides of the shear zone for several metres. The clear implication, therefore, is that the pore connectivity spreads for at least this distance too. Indeed, once outwith the zone of influence of the shear zone (a few decimetres deep at most), there is little obvious difference in the pore space geometry (other than the constrictivity and tortuosity shown by the 'barrier' and 'channel' effect discussed above) and it is therefore tempting to suggest that the entire rock matrix is, in principle, open to diffusive transport of contaminants.

There is certainly evidence from the Scandinavian Shield that connected porosity can extend for 0.5 m behind fractures in some cases (see the discussions in SMELLIE & STUCKLESS 1985, and ALEXANDER et al. 1990a) and evidence from both granites and sediments for the presence of connected porosity in the rock matrix several metres away from fractures (see HOFMANN 1990 and MILLER et al. 2000, for discussion). These data are also consistent with recent observations (SMELLIE 2000) from the Aspö site in Sweden on matrix pore fluids, which imply a connected porosity over distances of several metres (although it is speculated here that the form of connectivity may include microfracturing, there is, as yet, no hard evidence).

This being the case, it seems likely that the usual PA assumption of limited matrix diffusion depth may well be over-conservative and that it is simply a case of looking systematically for more evidence of connected matrix porosity at depth in a repository host rock. Although it is accepted that most repository designs can be shown to be safe without requiring the presence of large volumes of accessible host rock, it would certainly greatly increase confidence in the potential retardation capacity of a host rock if unlimited matrix diffusion could be shown to occur. Such a long-term, large scale demonstration experiment is currently under consideration for the planned Grimsel Phase VI (more details on [www.grimsel.com](http://www.grimsel.com)).

---

<sup>22</sup> See also the comments in footnote 16 on the treatment of variations in tortuosity and constrictivity in transport codes.

## **11           ACKNOWLEDGEMENTS**

The authors would like to extend their thanks to the many colleagues who contributed to this work in some capacity or another, especially to H. Dollinger and P. Bossart of the Geotechnisches Institut, Switzerland. Thanks also to Nagra and JNC for funding this work as part of the joint GTS radionuclide migration programme RMP.



## 12 REFERENCES

- ALEXANDER, W.R., SCOTT, R.D., MACKENZIE, A.B. & McKINLEY, I.G. (1990a): Natural analogue studies in crystalline rock: the influence of water bearing fractures on radionuclide immobilisation in a crystalline rock repository. Nagra Technical Report NTB 87-08. Nagra, Wettingen, Switzerland.
- ALEXANDER, W.R., McKINLEY, I.G., MACKENZIE, A.B. & SCOTT, R.D. (1990b): Verification of matrix diffusion in granite by means of natural decay series disequilibria. *Sci. Basis Nucl. Waste Manag.* XIII, 567-576.
- ALEXANDER, W.R., BRADBURY, M.H., McKINLEY, I.G., HEER, W., EIKENBERG, J. & FRICK, U. (1992): The current status of the radionuclide migration experiment at the Grimsel underground rock laboratory. *Sci. Basis Nucl. Waste Manag.* XV, 721-728.
- ALEXANDER, W.R., OTA, K. & FRIEG, B. (eds.) (2001): The Nagra-JNC *in situ* study of safety relevant radionuclide retardation in fractured crystalline rock II: the RRP project methodology development, field and laboratory tests. Nagra Technical Report NTB 00-06. Nagra, Wettingen, Switzerland.
- ALEXANDER, W.R., OTA, K., MÖRI, R. & McKINLEY, I.G. (2002): Synthesis of the results of the 15 year Nagra-JNC Radionuclide Migration Programme. *Geochem. Trans. (in prep.)*.
- AUZERAIS, F.M., DUNSMUIR, J., FERREOL, B.B., MARTYS, N., OLSON, J., RAMAKRISHNAN, T.S., ROTHMAN, D.H. & SCHWARTZ, L.M. (1996): Transport in sandstone: a study based on three dimensional microtomography. *Geophys. Res. Lett.* 23, 705-708.
- BARENBLATT, G.I., ZHELTOV IV, P. & KOCHINA, I.N. (1960): Basic concepts in the theory of seepage of homogeneous liquids in fissured rock. *J. Appl. Math. Mech.* 24, 1286.
- BIRCH, F. (1960): The velocity of compressional waves in rocks to 10 kilobars – Part 1. *J. Geophys. Res.* 65, 1083-1102.
- BIRCH, F. (1960): The velocity of compressional waves in rocks to 10 kilobars – Part 2. *J. Geophys. Res.* 66, 2199-2224.
- BISCHOFF, K., WOLF, K. & HEIMGARTNER, B. (1987): Hydraulische Leitfähigkeit, Porosität und Uranrückhaltung von Kristallin und Mergel: Bohrkern-Infiltrationsversuche. Nagra Technical Report NTB 85-42. Nagra, Wettingen, Switzerland.
- BLÜMLING, P. (1997): Borehole sealing project at the Grimsel Test Site. 3<sup>rd</sup> European Engineering Geology Conference, 33<sup>rd</sup> Annual Conference of the Engineering Group of the Geological Society. *Geo-Engineering of Hazardous and Radioactive Waste Disposal*. 10 – 14 September 1997. Proc., edited by G.M. Reeves 19-36.
- BOSSART, P. & MAZUREK, M. (1991): Structural geology and water flow paths in the migration shear zone. Nagra Technical Report NTB 91-12. Nagra, Wettingen, Switzerland.

- BOSSART, P., MAZUREK, M. HELLMUTH, K.-H., SCHNEEBELI, M. & SIITARI-KAUPPI, M. (1991): Structural geology and water flow-paths in the Migration shear-zone. Nagra Technical Report NTB 91-12. Nagra, Wettingen, Switzerland.
- BRACE, W.F. (1965): Some new measurements of linear compressibility of rocks. *J. Geophys. Res.* 70/2, 391-398.
- BRACE, W.F., WALSH, J.B. & FRANGOS, W.T. (1968): Permeability of granite under high pressure. *J. Geophys. Res.* 2225-2236.
- BRADBURY, M.H. & STEPHEN, I.G. (1986): Diffusion and permeability based sorption measurements in intact rock samples. *Sci. Basis Nucl. Waste Manag.* IX, 81-90.
- BRADBURY, M.H., GREEN, A., LEVER, D. & STEPHEN, I.G. (1986): Diffusion and permeability based sorption measurements in sandstone, anhydrite and Upper Magnesian Limestone samples. UKAEA Report AERE R 11995. AEA Technology, Harwell, UK.
- BROWN, G.O., STONE, M.L. & GAZIN, J.E. (1993): Accuracy of gamma ray computerized topography in porous media. *Water Resour. Res.* 29, 479-486.
- BYEGÅRD, J., WIDERSTRAND, H., SKALBERG, M., TULLBORG, E.-L. & SIITARI-KAUPPI, M. (2001): Complementary investigation of diffusivity, porosity and sorptivity of Feature A-site specific geologic material. Äspö International Co-operation Report ICR-01-04. SKB, Stockholm, Sweden.
- CHERNIS, P.J. (1981): Scanning electron microscope study of the microcrack structure of a granite sample from Pinawa, Manitoba. AECL report TR-173. AECL, Whiteshell, Canada.
- CHERNIS, P.J. (1983): Notes on the pore-microfracture structure of some granitic samples from the Whiteshell Nuclear Research Establishment. AECL Report TR-226. AECL, Whiteshell, Canada.
- CHERNIS, P.J. (1984): Comparison of the pore microcrack structure of shallow and deep samples of the Lac Du Bonnet granite. AECL Report TR-223. AECL, Whiteshell, Canada.
- CHOUKROUNE, P. & GAPAIS, D. (1983): Strain pattern in the Aar granite (Central Alps): orthogneis developed by bulk inhomogeneous flattening. *J. Struct. Geol.* 5, 411-418.
- DREW, D.J. & VANDERGRAAF, T.T. (1989): Construction and operation of a high pressure radionuclide migration apparatus. AECL Report TR-476. AECL, Whiteshell, Canada.
- FRANKLIN, J.A.M., VOGLER, U.W., SZLAVIN, J., EDMOND, J.M., BIENIAWSKI, Z.T. (1979): Suggested methods for determining water content, porosity, density, adsorption and related properties and swelling and slake durability index properties. *In*: BROWN, E.T. (ed.): Rock characterization testing and monitoring, ISRM suggested methods, 81-94. Pergamon Press, Oxford.
- FREDRICH, J.T., MENÉNDEZ, B. & WONG, T.-F. (1995): Imaging the pore structure of geo-materials. *Science* 268, 276-279.

- FREDRICH, J.T. (1999): 3-D imaging of porous media using laser scanning confocal microscopy with application to microscale transport processes. *Phys. Chem. Earth A* 24, 551-561.
- FRICK, U., ALEXANDER, W.R., BAEYENS, B., BOSSART, P., BRADBURY, M.H., BÜHLER, CH., EIKENBERG, J., FIERZ, TH., HEER, W., HOEHN, E., McKINLEY, I.G. & SMITH, P.A. (1992): The radionuclide migration experiment – Overview of investigations 1985-1990. Nagra Technical Report NTB 91-04. Nagra, Wettingen, Switzerland.
- FRICK, U., SKAGIUS, K. & ALEXANDER, W.R. (1993): An evaluation of diffusion in the groundwater of crystalline rocks. Unpubl. Nagra Internal Report, translated January 1996. Nagra, Wettingen, Switzerland.
- GARRELS, R.M., DREYER, R.M. & HOWLAND, A.L. (1949): Diffusion of ions through intergranular spaces in water saturated rocks. *Bull. Geol. Soc. Amer.* 60, 1809-1924.
- GRISAK, G.E. & PICKENS, J.F. (1980): Solute transport through fractured media. Part I: The effect of matrix diffusion. *Water Resour. Res.* 16, 719-730.
- GRISAK, G.E., PICKENS, J.F., BELANGER, D.W. & AVIS, J.D. (1985): Hydrogeologic testing of crystalline rocks during the Nagra Deep Drilling Programme. Unpubl. Nagra Internal Report. Nagra, Wettingen, Switzerland.
- HADERMAN, J. & RÖSEL, F. (1985): Radionuclide chain transport in homogeneous crystalline rocks: limited matrix diffusion and effective surface sorption. Nagra Technical Report NTB 85-40. Nagra, Wettingen, Switzerland.
- HASTRUP, K (1976): Pore structure, mechanical properties and polymer characteristics of porous materials impregnated with methylmethacrylate. Library of Danish Atomic Energy Commission, Risø, Roskilde, Denmark.
- HEATH, M.J. & MONTOTO, M. (1996): Rock matrix diffusion as a mechanism for radionuclide retardation: natural radio-element migration in relation to the microfractography and petrophysics of fractured crystalline rock. CEC Report EUR 17121 EN, CEC Luxembourg.
- HEER, W. & SMITH, P.A. (1998): Modelling the radionuclide migration experiment at Grimsel – What have we learned? *Sci. Basis Nucl. Waste Manag.* XXI, 663-670.
- HELLMUTH, K.-H. & SIITARI-KAUPPI, M. (1998): Imprägnation von Tongesteinen mit C-14-Polymethylmethacrylat (PMMA). Unpubl. Nagra Internal Report. Nagra, Wettingen, Switzerland.
- HELLMUTH, K.-H., KLOBES, P., MEYER, K., RÖHL-KUHN, B., SIITARI-KAUPPI, M., HARTIKAINEN, J., HARTIKAINEN, K. & TIMONEN, J. (1995): Matrix retardation studies: size and structure of the accessible pore space in fresh and altered crystalline rock. *Z. geol. Wiss.* 23/(5/6), 691-706.
- HOFMANN, B.A. (1990): Reduction spheres in haematitic rocks from northern Switzerland: implications for the mobility of some rare elements. Nagra Technical Report NTB 89-17. Nagra, Wettingen, Switzerland.

- JNC (2000): H12: Project to Establish the Scientific and Technical Basis for HLW Disposal in Japan. Supporting Report 3, Safety Assessment of the Geological Disposal System. JNC Technical Report TN1410 2000-004. JNC, Tokai, Japan.
- KBS (1983): Final storage of spent nuclear fuel. SKB/KBS 3. Stockholm, Sweden.
- KEUSEN, H.R., GANGUIN, J., SCHULER, P. & BULETTI, M. (1989): Felslabor Grimsel – Geologie. Nagra Technical Report NTB 87-14. Nagra, Wettingen, Switzerland.
- KICKMAIER, W., VOMVORIS, S., ALEXANDER, W.R., MARSHALL, P., FRIEG, B., WANNER, W. & HUERTAS, F. (2001): GTS – Nagra's underground research laboratory in crystalline rock: status of the scientific programme 1997 – 2002. Hydrology (*in press*).
- KLINKENBERG, L.J. (1951): Analogy between diffusion and electrical conductivity in porous rocks. Bull. Geol. Soc. Amer. 62, 559-568.
- KOPLIK, J., LIN, C. & VERMETTE, M. (1984): Conductivity and permeability from micro-geometry. J. Appl. Phys. 56, 3127-3131.
- KULL, H., BREWITZ, W. & KLARR, K. (1993): Felslabor Grimsel – Ventilationstest: In-situ-Verfahren zur Permeabilitätsbestimmung im Kristallin. Nagra Technical Report NTB 91-02. Nagra, Wettingen, Switzerland.
- LIN, C., PIRIE, G. & TRIMMER, D.A. (1986): Low permeability rocks – Laboratory measurements and three-dimensional microstructural analysis. J. Geophys. Res. 91, 2173-2181.
- McKINLEY, I.G. (1989a): Applying natural analogues in predictive performance assessment: 1. Principles and requirements. *In*: SALTELLI, A., STANNERS, D.A. & D'ALLESSANDRO, M. (eds.): Risk analysis in nuclear waste management, 377-396 (1989).
- McKINLEY, I.G. (1989b): Applying natural analogues in predictive performance assessment: 2. Examples and discussions. *In*: SALTELLI, A., STANNERS, D.A. & D'ALLESSANDRO, M. (eds.): Risk analysis in nuclear waste management, 377-396 (1989).
- McKINLEY, I.G., ALEXANDER, W.R., BAJO, C., FRICK, U., HADERMANN J., HERZOG, F.A. & HOEHN, E. (1988): The radionuclide migration experiment at the Grimsel rock laboratory, Switzerland. Sci. Basis Nucl. Waste Manag. XI, 170-187.
- MARQUER, D. & GAPAIS, D. (1985): Les massifs cristallins externes sur une transversale Guttannen – Val Bedretto (Alpes Centrales): Structures et histoire cinématique. Comptes rendus de l'Académie des Sciences, Paris, tome 301(II)/8, 543-546.
- MARQUER, D., GAPAIS, D. & CAPDEVILA, R. (1985): Comportement chimique et orthogneissification d'une granodiorite en faciès schistes verts (Massif de l'Aar, Alpes Centrales). Bull. Mineral 108, 209-221.
- MAZUREK, M., ALEXANDER, W.R. & MACKENZIE, A.B. (1996): Contaminant retardation in fractured shales: matrix diffusion and redox front entrapment. J. Contam. Hydrol. 21, 71-84.
- MILLER, W.M., ALEXANDER, W.R., CHAPMAN, N.A., McKINLEY, I.G. & SMELLIE, J.A.T. (2000): Geological disposal of radioactive wastes and natural analogues. Pergamon, Amsterdam, The Netherlands.

- MÖRI, A., BÜHLER, C., HAAG, P. & OTA, K. (1996): Connected Porosity (CP) – visualising the pore space in crystalline rock matrix using fluorescent acrylic resin. Unpubl. Nagra Internal Report. Nagra, Wettingen, Switzerland.
- MÖRI, A., ALEXANDER, W.R., OTA, K. & FRIEG, B. (eds.) (2001): The Nagra-JNC *in situ* study of safety relevant radionuclide retardation in fractured crystalline rock III: the RRP project final report. Nagra Technical Report NTB 00-07 (*in prep.*). Nagra, Wettingen, Switzerland.
- MONTOTO, M., HEATH, M.J., RODRIGUEZ REY, A., RUIZ DE ARGANDONA, V.G., CALLEJA, L. & MENEDEZ, B. (1992): Natural analogue and microstructural studies in relation to radionuclide retardation by rock matrix diffusion in granite. CEC Report EUR 14352 EN, CEC Luxembourg.
- MONTOTO, M., MARTIEZNISTAL, A., RODRIGUEZ REY, A., FERNANDEZ MERAYO, N. & SORIANO, P. (1995): Microfractography of granitic-rocks under confocal scanning laser microscopy. *J. of Microscopy* 177, 138-149.
- NAGRA (1985): Nukleare Entsorgung Schweiz: Konzept und Übersicht über das Projekt Gewähr. Nagra Gewähr Reports NGB 85-01 to 85-08, NGB 85-09 (English Summary). Nagra, Wettingen, Switzerland.
- NAGRA (1994): Kristallin-1 Safety Assessment Report. Nagra Technical Report NTB 93-22. Nagra, Wettingen, Switzerland.
- NEALL, F.N. & SMITH, P.A. (2001): H12: a perspective on PA aims, procedures, data and results. Unpubl. Nagra Project Report. Nagra, Wettingen, Switzerland.
- NERETNIEKS, I. (1980): Diffusion in the rock matrix: an important factor in radionuclide retardation? *J. Geophys. Res.* 85, 4379-4397.
- NERETNIEKS, I. (1985): Some Aspects of the use of iron canisters in deep lying repositories for nuclear waste. Nagra Technical Report NTB 85-35. Nagra, Wettingen, Switzerland.
- NOVER, G., HEIKAMP, S., KOTNY, A. & DUBA, A. (1995): The effect of pressure on the electrical conductivity of KTB rocks. *Surveys in Geophysics* 16, 63-81.
- NUR, A. & SIMMONS, F. (1969): The effect of saturation on velocity in low porosity rocks. *Earth Planet Sci. Lett.* 7, 183-193.
- OTA, K., AMANO, K. & ANDO, T. (1999): Brief overview of *in situ* nuclide retardation in a fractured crystalline rock, Kamaishi *In Situ* Test Site. *In: Proceedings of an International Workshop for the Kamaishi Experiments, Kamaishi, Japan, August 1998.* JNC Technical Report, JNC TN7400 99-00. JNC Tono Geoscience Centre, Toki, Japan.
- OTA, K., MÖRI, A., ALEXANDER, W. R., FRIEG, B. & SCHILD, M. (2003): Influence of the mode of matrix porosity determination on matrix diffusion calculations. *J. Contam. Hydrol.* 61, 131-145.
- POPP, T. (1994): Der Einfluss von Gesteinsmatrix, Mikrorissgefügen und intergranularen Fluiden auf die elastischen Wellengeschwindigkeiten und die elektrische Leitfähigkeit krus-tenrelevanter Gesteine unter PT-Bedingungen – eine experimentelle Studie. PhD Thesis, Univ. Kiel, 167pp.

- RASILAINEN, K., HELLMUTH, K.H., KIVEKÄS, L., MELAMED, A., RUSKEENIEMI, T., SIITARI-KAUPPI, M., TIMONEN, J. & VALKIAINEN, M. (1996): An interlaboratory comparison of methods for measuring rock matrix porosity. VTT Research Notes 1776. Technical Research Center of Finland, Espoo, Finland.
- RASMUSON, A. & NERETNIEKS, I. (1981): Migration of radionuclides in fissured rock: the influence of micropore diffusion and longitudinal dispersion. *J. Geophys. Res.* 86, 3749-3578.
- SARDINI, P., SAMMARTINO, S., MEUNIER, A. & TEVISSSEN, E. (1999): Evolution of fluid pathways of Charroux-Civray tonalite (Part II): numerical study of microcrack networks. *Phys. Chem. Earth A* 24/7, 621-625.
- SCHILD, M. (1999): Verbundene Mikroporositäten in Kristallingesteinen. Fallstudie Felslabor Grimsel; PhD Thesis, Univ. Göttingen, 176pp.
- SIEGESMUND, S., VOLLBRECHT, A., CHLUPAC, T., NOVER, G., DÜRRAST, H., MÜLLER, J. & WEBER, K. (1993): Fabric-controlled anisotropy of orthophysical properties observed in KTB core samples. *Scientific Drilling* 4, 31-54.
- SKAGIUS, K. & NERETNIEKS, I. (1982): Diffusion in crystalline rocks of some sorbing and non-sorbing species. SKB Technical Report TR 82-12. SKB, Stockholm, Sweden.
- SKAGIUS, K. & NERETNIEKS, I. (1983): Diffusion measurements in crystalline rocks. SKB Technical Report TR 83-15. SKB, Stockholm, Sweden.
- SKAGIUS, K. & NERETNIEKS, I. (1985a): Diffusivities in crystalline rock materials. *Sci. Basis Nucl. Waste Mang.* IX, 73-80.
- SKAGIUS, K. & NERETNIEKS, I. (1985b): Porosities and diffusivities of some non-sorbing species in crystalline rock. SKB Technical Report TR 85-03. SKB, Stockholm, Sweden.
- SKAGIUS, K. & NERETNIEKS, I. (1986): Porosities and diffusivities of some non-sorbing species in crystalline rocks. *Water Resour. Res.* 22, 389-397.
- SMELLIE, J.A.T. (2000): Aspö Hard Rock Laboratory: status report of the Matrix Fluid Experiment, June 1998 – June 2000. Äspö Internal Progress Report IPR-00-35. SKB, Stockholm, Sweden.
- SMELLIE, J.A.T. & STUCKLESS, J.S. (1985): Element mobility studies of two drillcores from the Götemar granite (Krakemala test site), SE Sweden. *Chem. Geol.* 51, 55-78.
- SMITH, P.A., ALEXANDER, W.R., HEER, W., FIERZ, T., MEIER, P.M., BAEYENS, B., BRADBURY, M.H., MAZUREK, M. & McKINLEY, I.G. (2001a): The Nagra-JNC in situ study of safety relevant radionuclide retardation in fractured crystalline rock I: the radionuclide migration experiment – Overview of investigations 1990-1996. Nagra Technical Report NTB 00-09. Nagra, Wettingen, Switzerland.
- SMITH, P.A., ALEXANDER, W.R., KICKMAIER, W., OTA, K., FRIEG, B. & McKINLEY (2001b): Development and testing of radionuclide transport models for fractured rock: examples from the Nagra/JNC Radionuclide Migration Programme in the Grimsel Test Site, Switzerland. *J. Contam. Hydrol.* 47, 335-348.

- SPANNE, P., THOVERT, J.F., JACQUIN, C.J., LINDQUIST, W.B., JONES, K.W. & ADLER, P.M. (1994): Synchrotron computed microtomography of porous media: topology and transports. *Phys. Rev. Lett.* 73, 2001-2004.
- STECK, A. (1968): Die alpidischen Strukturen in den Zentralen Aaregraniten des westlichen Aarmassivs. *Eclogae geol. Helv.* 61, 19-48.
- TORSTENFELT, B., ITTNER, T., ALLARD, B., ANDERSSON, K. & OLOFSSON, U. (1982): Mobilities of radionuclides in fresh and fractured crystalline rock. SKB Technical Report TR 82-26. SKB, Stockholm, Sweden.
- VALKIANEN, M. (1992): Diffusion in the rock matrix – A review of laboratory tests and field studies. YJT (Nuclear Waste Commission of Finnish Power Companies) Report 92-04. YJT, Helsinki, Finland.
- VILKS, P., CRAMER, J.J., JENSEN, M., MILLER, N.H., MILLER, H.G. & STANCHELL, F.W. (2001): In-situ diffusion experiment in granite: Phase I. *J. Contam. Hydrol.* (*submitted*).
- VOLLBRECHT, A., RUST, S. & WEBER, K. (1991): Development of microcracks in granites during cooling and uplift: examples from the Variscan basement in NE Bavaria (FRG). *J. Struct. Geol.* 7, 787-799.
- VOMVORIS, S. & FRIEG, B. (eds.) (1992): Overview of Nagra field and modelling activities in the ventilation drift (1988-1990). Nagra Technical Report NTB 91-34. Nagra, Wettingen, Switzerland.
- WATANABE, K., TAKEDA, S., YAMABE, T., ISHIYAMA, K. & BOSSART, P. (1993): Displacements of fractures during an *in situ* freezing and thawing test. I: Proceedings of an International Symposium on the Assessment and Prevention of Failure Phenomena in Rock Engineering, 5-7 April 1993. Istanbul, Turkey.